

# Functional $^1\text{H}$ MR spectroscopic investigations of pain processing in the human brain

## Dissertation

zur Erlangung des Doktorgrades der Naturwissenschaften  
(*Dr. rer. nat.*)

der

Naturwissenschaftlichen Fakultät II  
Chemie, Physik und Mathematik

der Martin-Luther-Universität  
Halle-Wittenberg

vorgelegt von

Frau MARIANNE CLEVE

geboren am 16.12.1986 in Halle (Saale)

1. **Gutachter:** Prof. Dr. Jochen Balbach
2. **Gutachter:** Prof. Dr. Jürgen R. Reichenbach (Uni Jena)
3. **Gutachter:** Prof. Dr. Peter Bachert (Uni Heidelberg)

**Tag der öffentlichen Verteidigung:** 20.12.2017

# Abstract

The regulation of signal transduction in the human brain by the main inhibitory and excitatory neurotransmitters GABA and glutamate is subject of current research, as alterations in turnover of these neurotransmitters are being held responsible to cause disease, such as chronic pain. Proton magnetic resonance spectroscopy ( $^1\text{H}$  MRS) enables quantitation of brain metabolites *in vivo* and non-invasively. Due to its low concentration in the brain, the detection of GABA at a clinical magnetic field strength of 3 T is methodologically challenging but feasible by applying the spectroscopic editing sequence  $^1\text{H}$  MEGA-PRESS. Additionally to the GABA resonances, the corresponding MR spectrum also contains the mixed signal Glx, which is composed of glutamate and glutamine, and allows to extract information about the excitatory function. Apart from spectroscopy in the resting state, functional  $^1\text{H}$  MRS measurements are increasingly used to investigate changes in stimulation-induced metabolite concentrations with the aim to gain knowledge about the regulation of neurochemical processes in the brain. In this context, one major aim of the current thesis was to detect GABA and glutamate signals and to quantify their concentration level changes during functional stimulation in the healthy human brain by using the  $^1\text{H}$  MEGA-PRESS sequence. Functional stimulation was realized by applying acute heat pain stimuli. A second aim of the thesis was to combine measurements of fMRS and functional MR imaging (fMRI) to investigate whether activation-induced alterations of the glutamatergic and GABAergic neurotransmitter metabolism are directly coupled to changes of the blood oxygenation levels. The latter is associated with an elevated cellular energy demand and has been revealed by fMRI.

After a brief introduction of the fundamentals of MRS and fMRI, the first part of the thesis describes a fully automatic method to correct frequency and phase drifts, which might occur during the MRS measurements and complicate reliable metabolite signal quantitation based on MEGA-PRESS MR spectra. This developed correction method distinctly improves the elimination of so-called subtraction artifacts, which was demonstrated on both simulated and *in vivo* data. In the second part of the thesis the question about the relative composition of Glx by glutamate and glutamine is addressed by means of phantom measurements, which is particularly important for the interpretation of the quantified metabolite signal intensities. The MEGA-PRESS sequence was then applied to explore the limits in detecting concentration differences of GABA and Glx in aqueous solutions of brain metabolites. Simulation of under *in vivo* conditions acquired spectra revealed that GABA and Glx concentration differences of below 5% can be identified with a typical sample size of 20 subjects.

The third part of the thesis describes a functional MRS study in volunteers, which resulted in the observation of decreased GABA and increased Glx levels in the anterior cingulate and occipital cortex during acute heat pain stimulation. The fourth and last part of the presented work describes combined fMRS and fMRI measurements in a second group of volunteers. As a result, associations between the neurovascular responses (BOLD signals) during acute pain perception within the pain processing brain network and local resting state GABA levels in the insular cortex as well as with pain-induced relative Glx changes in the same cortex region were found. In summary, these findings shed light on the way how activity in brain networks is influenced by neurochemical level changes in and between certain cerebral brain areas. These results offer great potential for further functional MR spectroscopy studies to better understand the regulation of brain activity in healthy subjects but may also pave the way to increase knowledge about the development and manifestation of brain diseases in a rather unique way.

# Zusammenfassung

Die Regulation der Signalweiterleitung im menschlichen Gehirn durch die beiden wichtigsten inhibitorischen und exzitatorischen Neurotransmitter GABA und Glutamat ist Gegenstand aktueller Forschung, da Veränderungen im Neurotransmitterstoffwechsel als Ursache von Erkrankungen, wie beispielsweise der Manifestation von chronischem Schmerz, vermutet werden. Die Protonenmagnetresonanzspektroskopie ( $^1\text{H}$ -MRS) ermöglicht hierbei die Hirnmetaboliten *in vivo* und nicht-invasiv zu quantifizieren. Aufgrund seiner niedrigen Konzentration im Gehirn stellt die Detektion von GABA bei klinischen Magnetfeldstärken von 3T eine methodische Herausforderung dar, die jedoch durch Anwendung der speziellen Editierungssequenz  $^1\text{H}$ -MEGA-PRESS realisiert werden kann. Neben Signalen von GABA enthält das entsprechende MR-Spektrum zudem das Mischsignal Glx, bestehend aus Beiträgen von Glutamat und Glutamin, sodass zusätzlich Informationen über exzitatorische Vorgänge extrahiert werden können. Über die spektroskopische Untersuchung im Ruhezustand hinaus wird die funktionelle  $^1\text{H}$ -MRS zunehmend angewandt, um stimulusinduzierte Änderungen von Metabolitenkonzentrationen zu detektieren und damit Aufschluss über die Regulation von neurochemischen Hirnprozessen zu erhalten. Vor diesem Hintergrund war ein Ziel der vorliegenden Dissertation mögliche Konzentrationsänderungen von GABA und Glutamat während funktioneller Stimulation im gesunden menschlichen Gehirn mithilfe der  $^1\text{H}$ -MEGA-PRESS Spektroskopie zu quantifizieren. Dabei wurde die funktionelle Stimulation durch die Applikation von akuten Hitzeschmerzreizen realisiert. Ein zweites Ziel der Arbeit stellte die Durchführung kombinierter Messungen von fMRS und funktioneller MR-Tomographie (fMRT) dar, um zu untersuchen, ob aktivierungsbedingte Alterationen des glutamatergen und GABAergen Neurotransmitterstoffwechsels mit Änderungen der Blutoxygenierung direkt gekoppelt sind. Letztere sind mit einem erhöhten zellulären Energiebedarf assoziiert und können durch die fMRT abgebildet werden.

Nach einer kurzen Einführung der Grundlagen der MRS und fMRT wird vorab eine eigens implementierte vollautomatische Methode zur Korrektur von Frequenz- und Phasenverschiebungen beschrieben, die während MRS Messungen auftreten können und eine reliable Quantifizierung der Metabolitensignale basierend auf MEGA-PRESS MR-Spektren erschweren. Das in dieser Arbeit entwickelte Korrekturverfahren verbessert erheblich die Eliminierung von sogenannten Subtraktionsartefakten, was sowohl an simulierten als auch an *in vivo* Daten belegt wurde. Im zweiten Teil der Arbeit wird der Frage nach der relativen Zusammensetzung von Glx aus Glutamat und Glutamin anhand von Phantommessungen nachgegangen, was insbesondere für die Interpretation

der quantifizierten Metabolitenintensitäten von Bedeutung ist. Die MEGA-PRESS Sequenz wurde im Weiteren angewendet, um die Grenzen der Detektierbarkeit von GABA- und Glx-Konzentrationsunterschieden in wässrigen Hirnmetabolitenlösungen zu untersuchen. Die Simulation von unter *in vivo* Bedingungen gemessenen Spektren ergab, dass GABA- und Glx-Konzentrationsunterschiede von weniger als 5 % bei einer üblichen Fallzahl von 20 Probanden identifiziert werden können.

Der dritte Teil der Arbeit beschreibt eine funktionelle MRS Studie von Probanden, bei denen eine Abnahme der GABA-Konzentrationen bei gleichzeitiger Zunahme der Glx-Konzentrationen im anterioren cingulären und okzipitalen Kortex während der akuten Schmerzstimulation beobachtet werden konnte. Der vierte und letzte Abschnitt der vorliegenden Dissertation stellt dann die Ergebnisse kombinierter fMRS und fMRT Messungen von einer weiteren Probandengruppe vor. Dabei konnten Assoziationen zwischen neurovaskulären Reizantworten (BOLD-Signale) während der akuten Schmerzwahrnehmung innerhalb des Schmerzhirnnetzwerkes und den lokalen, insulären Ruhekonzentrationen von GABA sowie den schmerzinduzierten relativen Glx-Änderungen in derselben Kortexregion demonstriert werden. Zusammenfassend tragen diese Befunde zur Klärung bei, wie die Aktivität in Hirnnetzwerken durch neurochemische Konzentrationsalterationen in und zwischen bestimmten zerebralen Hirnarealen beeinflusst wird. Damit eröffnet sich ein großes Potential für weitere funktionelle MR-spektroskopische Untersuchungen, um die Regulation der Hirnaktivität nicht nur im gesunden Gehirn sondern auch bei der Entstehung und Manifestation von Hirnerkrankungen besser zu verstehen.

# Contents

<b>Abstract</b>	<b>i</b>
<b>Zusammenfassung</b>	<b>iii</b>
<b>Abbreviations and symbols</b>	<b>viii</b>
<b>1 Introduction</b>	<b>1</b>
<b>2 Fundamentals</b>	<b>6</b>
2.1 Nuclear magnetic resonance . . . . .	6
2.1.1 Background . . . . .	6
2.1.2 RF excitation and relaxation phenomena . . . . .	7
2.1.3 Signal detection and Fourier transform . . . . .	9
2.2 MR spectroscopy . . . . .	11
2.2.1 Chemical shift . . . . .	11
2.2.2 J-coupling . . . . .	13
2.2.3 J-coupling evolution . . . . .	15
2.2.4 J-difference editing . . . . .	16
2.2.5 <sup>1</sup> H MEGA-PRESS sequence . . . . .	17
2.2.6 Metabolite signal quantitation . . . . .	21
2.3 Glutamate, glutamine and GABA - Neurotransmitters and metabolites	24
2.3.1 Glutamate and glutamine . . . . .	24
2.3.2 GABA . . . . .	25
2.4 Functional MR imaging . . . . .	27
2.4.1 BOLD effect . . . . .	27
2.4.2 fMRI data acquisition . . . . .	28
2.4.3 From fMRI data to BOLD activation maps . . . . .	29
<b>3 Post-processing of MR spectra</b>	<b>33</b>
3.1 Post-processing pipeline . . . . .	33

3.1.1	Zero-filling . . . . .	34
3.1.2	Frequency correction . . . . .	36
3.1.3	Water peak extraction . . . . .	36
3.1.4	Phase correction . . . . .	37
3.1.5	Difference optimization . . . . .	38
3.2	Applications to $^1\text{H}$ MEGA-PRESS spectra . . . . .	42
3.2.1	Simulations . . . . .	42
3.2.2	<i>In vivo</i> application . . . . .	45
3.2.3	Discussion . . . . .	47
<b>4</b>	<b>Systematic phantom experiments</b>	<b>50</b>
4.1	About the composition of Glx in the $^1\text{H}$ MEGA-PRESS difference spectrum	50
4.1.1	Glutamate and glutamine phantom measurements . . . . .	51
4.1.2	Conclusions and alternative approaches . . . . .	53
4.2	Measurable concentration differences of GABA and Glx . . . . .	55
4.2.1	Experiment setup . . . . .	56
4.2.2	Detectable concentration changes <i>in vitro</i> . . . . .	56
4.2.3	Detectable concentration changes under simulated <i>in vivo</i> conditions	59
4.2.4	Conclusions and limitations . . . . .	61
<b>5</b>	<b>Functional MR spectroscopy during acute pain perception in the human brain</b>	<b>63</b>
5.1	Motivation . . . . .	63
5.2	Experiment setup . . . . .	64
5.2.1	Volunteers and thermal stimulation unit . . . . .	64
5.2.2	Measurement protocol . . . . .	65
5.2.3	Metabolite measures and statistical analysis . . . . .	66
5.3	Results . . . . .	67
5.4	Discussion . . . . .	72
<b>6</b>	<b>Combined <i>in vivo</i> functional MRS and functional MRI during painful stimulation</b>	<b>76</b>
6.1	Motivation . . . . .	76
6.2	Preliminary examinations . . . . .	78
6.2.1	Stimulation paradigm and experiment design . . . . .	78
6.2.2	Data analysis . . . . .	80
6.2.3	Results and conclusion . . . . .	81
6.3	Experiment setup . . . . .	82



6.3.1	Measurement protocol . . . . .	82
6.3.2	Volunteers . . . . .	83
6.3.3	Functional MRS data acquisition and analysis . . . . .	83
6.3.4	Functional MRI data acquisition and analysis . . . . .	84
6.3.5	Statistical analysis . . . . .	87
6.4	Results . . . . .	87
6.4.1	Pain stimulation and data exclusion . . . . .	87
6.4.2	Functional MRS data . . . . .	87
6.4.3	Functional MRI data . . . . .	89
6.4.4	Associations between BOLD signal changes and metabolite levels	90
6.5	Discussion . . . . .	92
<b>7</b>	<b>Conclusion and Outlook</b>	<b>98</b>
	<b>Bibliography</b>	<b>xii</b>
	<b>List of Figures</b>	<b>xxviii</b>
	<b>List of Tables</b>	<b>xxx</b>
	<b>Appendix</b>	<b>xxxix</b>
A.1	List of all measurement parameters . . . . .	xxxix
A.2	Lebenslauf . . . . .	xxxv
A.3	Auszeichnungen . . . . .	xxxvi
A.4	Veröffentlichungen . . . . .	xxxvii
A.5	Danksagung . . . . .	xl
A.6	Selbstständigkeitserklärung . . . . .	xli

# Abbreviations and symbols

$\alpha_{met}$	Metabolite editing efficiency
ACC	Anterior cingulate cortex
$B_0$	Magnetic field strength
BOLD	Blood oxygenation level dependent
BW	Bandwidth
c	Concentration
$^{\circ}\text{C}$	Degree Celsius (unit)
$^{13}\text{C}$	Carbon-13
$\text{CH}_2$	Methylene groups
CH	Methine group
Cho	Choline
Cr	Creatine
CSF	Cerebral spinal fluid
$\delta$	Chemical shift
DIFF	Difference spectrum
DMN	Default mode network
E	Energy
ED	Edited spectrum
$\text{Ed}_{ED}$	Position of the editing pulse during the ED scan (ppm)
$\text{Ed}_{NED}$	Position of the editing pulse during the NED scan (ppm)
EEG	Electroencephalography

<b>EPI</b>	Echo Planar Imaging
<b>f</b>	Frequency
<b>f<sub>CSF</sub></b>	Fraction of cerebral spinal fluid
<b>f<sub>GM</sub></b>	Fraction of gray matter
<b>f<sub>WM</sub></b>	Fraction of white matter
<b>FFT</b>	Fourier transformation
<b>FFT<sup>-1</sup></b>	Inverse Fourier transformation
<b>FID</b>	Free induction decay
<b>fMRI</b>	Functional magnetic resonance imaging
<b>fMRS</b>	Functional magnetic resonance spectroscopy
<b>FWHM</b>	Full width at half maximum
<b>FWE</b>	Family wise error
<b>γ</b>	Gyromagnetic ratio
<b>GABA</b>	γ-Aminobutyric acid
<b>GABA+</b>	γ-Aminobutyric acid including signals from macromolecules
<b>Glu</b>	Glutamate
<b>Gln</b>	Glutamine
<b>Glx</b>	Glutamate and glutamine
<b>GM</b>	Gray matter
<b>h</b>	Planck's constant
<b><sup>1</sup>H</b>	Proton
<b>Hz</b>	Hertz (unit)
<b>Im</b>	Imaginary part of complex signal
<b>Ins</b>	Insular cortex
<b>J</b>	Coupling constant
<b>k<sub>E</sub></b>	Expected number of voxels
<b>l</b>	Liter (unit)
<b>MEG</b>	Magnetoencephalography

<b>MEGA-PRESS</b>	MEscher-GARwood Point-RESolved Spectroscopy
<b>min</b>	Minute (unit)
<b>mI</b>	<i>Myo</i> -inositol
<b>MM</b>	Macromolecules
<b>mol</b>	Mole (unit)
<b>MR</b>	Magnetic resonance
<b>MRI</b>	Magnetic resonance imaging
<b>MRS</b>	Magnetic resonance spectroscopy
$N_{Samp}$	Number of sampled points
<b>NAA</b>	<i>N</i> -Acetylaspartate
<b>NAS</b>	Number of acquired scans
<b>NED</b>	Non-edited spectrum
<b>NMR</b>	Nuclear magnetic resonance
<b>OC</b>	Occipital cortex
$\phi$	Phase
<b>p</b>	<i>P</i> -value (statistical hypothesis testing)
<b>PC</b>	Posterior cortex
<b>PET</b>	Positron emission tomography
<b>ppm</b>	Parts per million (unit)
<b>PRESS</b>	Point-RESolved Spectroscopy
<b>R</b>	Correlation coefficient
$R_{met,x}$	Metabolite ( <i>met</i> ) and substance ( <i>x</i> ) specific relaxation related signal attenuation
<b>Re</b>	Real part of complex signal
<b>ROI</b>	Region of interest
<b>rf</b>	Radio-frequency
$\sigma$	Shielding constant
<b>s</b>	Second (unit)

$s$	FID signal
$S$	Frequency spectrum
$\bar{S}$	Mean frequency spectrum averaged over all scans
<b>SII</b>	Secondary somatosensory cortex
<b>SMA/MCC</b>	Supplementary motor area with overlap to the mid-cingulate cortex
<b>SNR</b>	Signal-to-noise ratio
<b>T</b>	Tesla (unit)
$T_1$	Longitudinal relaxation time constant
$T_2$	Transverse relaxation time constant
$T_2^*$	Effective transverse relaxation time constant
$T_{max}$	Maximum temperature
<b>TA</b>	Acquisition time
<b>TCA</b>	Tricarboxylic acid
<b>tCr</b>	Total creatine
<b>TE</b>	Echo time
<b>TR</b>	Repetition time
<b>V</b>	Volume
$\omega_0$	Larmor frequency
<b>WM</b>	White matter

# Chapter 1

## Introduction

The human brain is the key structure in the central nervous system (CNS) processing information, coordinating and influencing activation in all parts of our body. Roughly, the brain consists of two major tissue compartments, gray and white matter, where the latter mainly consists of myelinated axons, and gray matter contains numerous neuronal cell bodies, astroglia and other cells. Assuming a painful stimulus is processed, e.g. following touching a hot stove plate, signal transduction starts with activation of peripheral nociceptors in the tissue, which is converted into an action potential traveling electrically along axons to neurons of stimulus specific brain regions (Silbernagl and Despopoulos, 2012). The electrically excitable neurons transmit a signal either again electrically or chemically via synapses. In case of chemical information transmission the electric action potential has to be converted into a chemical signal that in turn may act excitatory or inhibitory on the postsynaptic neuron. This chemical signal is generated by the release of neurotransmitter molecules from the presynaptic neuron into the synaptic cleft. The neurotransmitters diffuse through the extracellular space to the postsynaptic neuron where they bind to dedicated chemical receptors located in the cell membrane. This, in turn, can lead to a depolarization of the membrane potential and thus a new action potential may evolve transmitting the signal further. Presynaptic neurons are differentiated into excitatory and inhibitory depending on the neurotransmitter that they release. The major inhibitory and excitatory neurotransmitters in the human brain are  $\gamma$ -aminobutyric acid (GABA) and glutamate (Glu). GABA has a hyperpolarizing effect on the postsynaptic neuron, whereas Glu lowers the threshold of excitation by depolarization. The interplay between excitation and inhibition essentially regulates signal transduction in the CNS, and the so-called excitation-inhibition balance of neuronal synaptic transmission has become a focus of recent and current research.

Knowledge about the organization of functional neuronal networks of the brain that process different internal or external stimuli has immensely expanded with the

availability of modern imaging and electrophysiological techniques, such as functional magnetic resonance imaging (fMRI), positron emission tomography (PET) and magneto- and electroencephalography (MEG, EEG). However, all these techniques do not provide direct insight into the neurochemical involvement of GABA and Glu, which has significant impact on controlling of the regulation of brain activity. In contrast, magnetic resonance spectroscopy (MRS) is a non-invasive tool to study these underlying neurochemical processes and enables the measurement and quantitation of the brain metabolites GABA and Glu *in vivo* (Mullins et al., 2014) by exploiting the magnetic properties of atomic nuclei. In 1946, Bloch and Purcell discovered independently the absorption and emission of electromagnetic radiation in the MHz frequency range by protons upon resonant excitation when exposed to a strong external magnetic field (Bloch et al., 1946; Purcell et al., 1946), a phenomenon that is known as nuclear magnetic resonance (NMR). In 1950, it was discovered that the absorbed and emitted energy, and its related frequency, depends not only on the external magnetic field strength but also on the local chemical environment of the nuclei (Dickinson, 1950; Proctor and Yu, 1950). This spectral fingerprint finally allowed the identification of different chemical compounds, including brain metabolites in brain tissue. The main nucleus used in MR is the proton ( $^1\text{H}$ ) due to its inherent magnetic moment required for NMR and its high natural abundance. Even though MRS did not reach the same popularity as MR imaging, that depicts the spatial distribution of protons rather than distinguishing between metabolite specific resonance frequencies (Lauterbur, 1973; Mansfield and Grannell, 1973), MR spectroscopy evolved into a powerful tool to identify biological biomarkers and to explore the physiochemical processes regulating brain activity.

In contrast to Glu (12 mmol/l), GABA is present in the brain with only low concentration ( $< 2$  mmol/l) (Govindaraju et al., 2000; Rae, 2014), and its spectral resonances show strong overlap with signals of other metabolites making quantitation challenging on clinical MR scanners with moderate magnetic field strengths ( $\leq 3$  T) when using standard MRS sequences. Therefore, GABA measurements *in vivo* are typically performed by applying modified MRS techniques, such as 2D spectroscopic approaches or the spectral editing method MEGA-PRESS (MEscher-GARwood Point RESolved Spectroscopy (Mescher et al., 1998)). The MEGA-PRESS technique alters selectively the spectral appearance of the metabolite of interest between two separate MR scans while leaving contributions to the spectrum from overlapping signals unaffected. Then, by subtracting one scan from the other the manipulated metabolite signal can be extracted as an isolated resonance from the corresponding difference spectrum. Besides the detection of GABA, the MEGA-PRESS spectrum contains a composite resonance of Glu and glutamine (Gln) that is frequently reported as Glx instead of Glu and is

assumed to reflect the excitatory measure in a comparable way. Consequently, the MEGA-PRESS difference spectrum contains information about both inhibitory and excitatory function. However, it should be noted that MRS inherently suffers from low spatial resolution, which typically is in the milliliter range. Hence, more than  $10^{13}$  synapses are contained in a 10 ml spectroscopic volume located in the human cortex (Huttenlocher, 1979). Consequently, MR spectroscopy is far from capturing physiological processes on a cellular level but rather reflects spatially averaged neuronal activity within a certain brain area.

The amount of research related to the exploration of the excitation-inhibition balance with  $^1\text{H}$  MRS increases continuously because alterations of the neurochemical signal transmission are assumed to be related to brain disorders (Duncan et al., 2014), such as in chronic pain state (Borsook et al., 2007; Gussew et al., 2011; Harris and Clauw, 2012; Zhuo, 2008) that was, so far, mainly investigated by applying invasive approaches in animal studies (Fields et al., 1991; Jasmin et al., 2003; LaGraize and Fuchs, 2007). The latter represents indeed a major healthcare problem in western populations with huge financial impact on the healthcare system (King et al., 2011). Thus, improved understanding of cerebral pain processing in both diseased and healthy states may ultimately help to define novel, model-driven approaches that explore the neurochemical mechanisms underlying the development of chronic pain. The network of brain regions being involved in pain processing is well known and includes the anterior cingulate cortex (ACC), the insular cortices (Ins), the primary and secondary somatosensory cortex, the thalamus and the prefrontal cortex (Apkarian et al., 2005). However, it is not fully understood yet how such neurochemical alterations are involved in the manifestation of diseased brain states. It is for this reason that the basic principles of signaling and the associated energy metabolism in the human brain are increasingly explored in the healthy state to potentially unravel neurochemical imbalances causing brain disorders. A growing number of MRS studies applied functional measurements to determine stimulus-induced metabolite changes in stimulus-specific brain areas (Duncan et al. (2014); Mangia et al. (2009) and references therein). Brain activity under different stimulation conditions have been explored, including visual stimulation (Apšvalka et al., 2015; Mangia et al., 2007), motor activation (Schaller et al., 2014) and also acute pain stimulation (Gussew et al., 2010; Gutzeit et al., 2011; Kupers et al., 2009; Mullins et al., 2005).

In most functional MRS studies concentration changes of Glu were investigated (Apšvalka et al., 2015; Gussew et al., 2010; Gutzeit et al., 2011; Mangia et al., 2007; Mullins et al., 2005; Schaller et al., 2014) since its detection is less complicated compared to GABA. Most studies reported elevated Glu levels during stimulation. The increased



Glu concentration were associated with processes of metabolism and also neurotransmission that cannot be distinguished with  $^1\text{H}$  MRS. Consequently, the Glu changes are thus caused by either increased excitation or metabolism or both. In contrast, the GABA signal detected with MRS is distinctly closer related to neurotransmitter turnover, as it is less involved in metabolism than Glu, and is assumed to give a deeper insight into the excitation-inhibition balance (Stagg et al., 2011b). Nevertheless, functional GABA measurements have been rarely performed due to the above mentioned difficulty to resolve its resonances from *in vivo* brain MR spectra at clinical field strengths.

Against this background, the main objective of this thesis was to perform functional  $^1\text{H}$  MEGA-PRESS measurements during acute pain perception to explore whether changes of GABA and Glu can be observed and quantified in the human brain. The successful detection of metabolite concentration changes during brain activation offers an additional channel to explore the healthy brain but also to improve knowledge about the manifestation of brain diseases. To this end, a functional MRS study was conceived and conducted in a group of healthy volunteers.

Beyond and above, current research tackles to combine different measurement capabilities to merge separate measures that are assumed to be related to the same origin: Neuronal activity. Hence, it is an open hypothesis that metabolite turnover measured with MRS is associated with the indirect measure of neuronal activity as it is detected by using fMRI (Mangia et al., 2009). Functional MRI allows the depiction of varying blood oxygenation levels that are related to increased energy demands in brain regions being activated, e.g. by external stimulation. Additionally and in contrast to MRS, fMRI measurements depicts brain activity of the whole brain. This, in turn, enables to progressively extend the focus to the exploration of interrelations across brain regions since long range inhibitory and excitatory neuronal projections of connected brain areas are assumed to potentially impact the regulation of neuronal activity within brain networks (Duncan et al., 2014). Moreover, besides gaining deeper insight into metabolic processes that occur together with brain activation, combined fMRS and fMRI may also help to identify biological markers that are indicative of disbalanced neuronal activity at early stages of diseases. Consequently, the second goal of the current work was to set up a combined fMRS and fMRI study to further investigate possible interrelations between metabolite and corresponding neuronal activity measures across the brain during pain perception.

The thesis is organized as follows: Chapter 2 summarizes the fundamentals of NMR and the basic principles of MR spectroscopy. Moreover, the physiology of GABA and Glu in the human brain and the functional MR imaging method are introduced. In Chapter 3, the post-processing steps of MR spectra are presented together with a

new developed approach to automatically correct MEGA-PRESS difference spectra. MRS requires the acquisition of multiple scans resulting in measurement times of several minutes to allow for the reliable quantitation of metabolite signals from the final averaged MR spectrum. During the acquisition, drift errors due to measurement instabilities can occur that have to be corrected by appropriate post-processing of the acquired data. In particular, when using  $^1\text{H}$  MEGA-PRESS, drifts between the two initial different MR scans have to be accounted for to enable sufficient GABA quantitation. Moreover, in Chapter 4, the MEGA-PRESS sequence was characterized in terms of the quantified Glu amount from the difference spectrum since the composite measure Glx is mostly reported instead. However, the contributing amounts of Glu and Gln to the Glx signal, respectively, were not fully clarified yet, which is of major importance to give best possible interpretation of the observed metabolite measures. Additionally, before performing the functional MRS measurements, it was determined which concentration differences of GABA and Glu can be reliably resolved by using  $^1\text{H}$  MEGA-PRESS. Both open questions were addressed in phantom studies. Finally, Chapters 5 and 6 present the exploration of pain-induced changes of GABA and Glu in a functional MRS study as well as combined fMRS and fMRI experiments. The last chapter (Chapter 7) briefly summarizes the major findings of the present thesis and draws some conclusions for future studies.

# Chapter 2

## Fundamentals

This chapter provides a brief overview on the basic principles of nuclear magnetic resonance and its application in MR spectroscopy. In particular, the spectral editing sequence  $^1\text{H}$  MEGA-PRESS and its underlying principles are introduced. Moreover, the physiology of GABA and glutamate is briefly described. Finally, the mechanics of functional MRI experiments are depicted.

### 2.1 Nuclear magnetic resonance

This section briefly introduces the fundamentals of nuclear magnetic resonance. More detailed explanations are extensively covered in the following works of (Brown et al., 2014; de Graaf, 2007; Levitt, 2008; Vlaardingerbroek and den Boer, 2003).

#### 2.1.1 Background

Nuclear magnetic resonance is based on the existence of the nuclear spin  $I$  and its associated angular momentum  $\vec{p}$ :

$$|\vec{p}| = \frac{h}{2\pi} \cdot \sqrt{I \cdot (I + 1)} \quad (2.1)$$

Only nuclei with a nonzero spin  $I$  are relevant for NMR, as it occurs in atomic nuclei except those with an even number of both protons and neutrons, since they reveal a magnetic moment  $\vec{\mu}$ :

$$\vec{\mu} = \gamma \cdot \vec{p} \quad (2.2)$$

$\gamma$  denotes the gyromagnetic ratio that is specific for each type of nuclei. If no external magnetic field is applied, the magnetic moments are randomly oriented in space and

energetically equivalent. Hence, no magnetization occurs. In contrast, when the nuclear spins are exposed to an external homogeneous magnetic field of the magnetic field strength  $\vec{B}_0$  the magnetic moments precess around the direction (z) of the magnetic field. Quantization of direction occurs regarding  $\vec{B}_0 \parallel z$ , resulting in  $(2I + 1)$  discrete energy levels  $E_m$ :

$$E_m = -\mu_z \cdot B_0 = -\gamma \cdot m \cdot \frac{h}{2\pi} \cdot B_0 \quad (2.3)$$

The magnetic quantum number is given by m ( $m = -I, -I+1, \dots, I-1, I$ ) and the Planck's constant is denoted by h ( $h = 6.620755 \cdot 10^{-34}$  Js). In thermal equilibrium, the energy levels  $E_m$  (see Eq. 2.3) are populated according to the Boltzmann statistics. Assuming protons (nuclear spin of  $I = 1/2$ ) the ratio between the two possible levels becomes:

$$\frac{N_{-1/2}}{N_{+1/2}} = \exp\left(-\frac{\Delta E}{k_B \cdot T}\right) = \exp\left(-\frac{h \cdot \gamma \cdot B_0}{2\pi \cdot k_B \cdot T}\right) \quad (2.4)$$

$N_{-1/2}$  and  $N_{+1/2}$  are the number of spins with  $m = -1/2$  and  $m = +1/2$ , respectively,  $k_B$  is the Boltzmann constant ( $k_B = 1.38065 \cdot 10^{-23}$  J/K) and T the temperature (in K). The sensitivity of nuclear magnetic resonance depends on the population difference between the energy levels, and can be increased by using nuclei of large  $\gamma$ , measurements at high magnetic field strengths  $B_0$  and reducing the temperature T. Obviously, the latter is not an option for in *in vivo* measurements. Thus, the population difference for hydrogen nuclei at a typical *in vivo* temperature of 37°C and a clinical field strength of 3 T results in 0.002%. Even if this population difference is very small, a measurable net magnetization  $\vec{M}_0$ , or macroscopic magnetisation, along the z axis is produced due to the large number of hydrogen nuclei usually encountered in the human body. Moreover, hydrogen reveals in fact the largest gyromagnetic ratio  $\gamma$  of  $2.675 \cdot 10^8$  rad/T/s compared to other isotopes used in *in vivo* NMR, e.g.  $^{31}\text{P}$  ( $\gamma = 1.084 \cdot 10^8$  rad/T/s) or  $^{13}\text{C}$  ( $\gamma = 0.673 \cdot 10^8$  rad/T/s) (de Graaf, 2007).

## 2.1.2 RF excitation and relaxation phenomena

By irradiating an oscillating magnetic field (rf-pulse) to the nuclear spins perpendicular to  $\vec{M}_0$ , transitions between the energy levels can be induced if the frequency of the rf-pulse matches  $\Delta E$  (see Eq. 2.3):

$$\Delta E = \frac{h}{2\pi} \cdot \omega_0 = E_{-\frac{1}{2}} - E_{+\frac{1}{2}} = \gamma \cdot \frac{h}{2\pi} \cdot B_0 \quad (2.5)$$

Following, the frequency  $\omega_0$  is given by:

$$\omega_0 = \gamma \cdot B_0 \quad (2.6)$$

and is called resonance or Larmor frequency, which is specific for each nuclear isotope. The macroscopic magnetisation is then deflected by a certain angle, e.g. by 90 deg., into to the x,y-plane while precessing around  $\vec{B}_0$ . Its precession produces an oscillating magnetic field that in turn induces an electric voltage in the receiver coils that corresponds to the finally detected NMR signal. After switching off the rf-pulse the net magnetisation continues to precess with the Larmor frequency around the z axis. Relaxation of the net magnetisation to its equilibrium position  $\vec{M}_0$  occurs due to interactions between the nuclei and their molecular surroundings and can be divided into two main mechanisms, the spin-lattice and the spin-spin relaxation. The spin-lattice relaxation describes the recovery of the longitudinal component  $M_z$  of the macroscopic magnetisation  $\vec{M}_0$  and is related to energy exchange between spins and their surrounding. It is characterized by the time constant  $T_1$ . The decay of the transverse component  $M_{x,y}$  is the spin-spin relaxation that occurs due to spin energy exchange between themselves, which in turn leads to irreversible dephasing among the precessing spins, and is described by the constant  $T_2$ . According to the Bloch's equations (Bloch et al., 1946) the relaxation processes after an on-resonant 90 deg. rf-pulse can be described by exponential functions:

$$\begin{aligned} M_z(t) &= M_0 \cdot \left( 1 - \exp\left(-\frac{t}{T_1}\right) \right) \\ M_{x,y}(t) &= M_0 \cdot \exp\left(-\frac{t}{T_2}\right) \end{aligned} \tag{2.7}$$

The spin-spin-relaxation is usually accelerated by magnetic field inhomogeneities of  $\vec{B}_0$  induced by the sample itself. This additional component is characterized by the time constant  $T'_2$  and usually dominates the  $M_{x,y}$  decay. The effective transverse relaxation time  $T_2^*$  then results to:

$$\frac{1}{T_2^*} = \frac{1}{T_2} + \frac{1}{T'_2} \tag{2.8}$$

Magnetic field inhomogeneities of  $\vec{B}_0$  can be reduced to some extent by appropriate shimming of the target volume by applying additional magnetic field gradients. However, since the remaining magnetic field inhomogeneities are assumed to be static, the  $T'_2$  related relaxation processes can be reversed by applying an additional 180 deg. pulse at  $t = TE/2$ , and thus being timely centered between excitation rf-pulse and the start of the acquisition. The rf-pulse refocuses phase shifts between the precessing spins in the x,y-plane and subsequently a spin echo is generated at  $t = TE$ . Thus, the echo time TE is an important parameter in NMR experiments. The so-called spin echo experiment was first described by Erwin Hahn in 1950 (Hahn, 1950).

### 2.1.3 Signal detection and Fourier transform

As introduced in the previous section, the induced electric voltage by the precessing magnetisation  $M_{x,y}$  and its decay over time is the actual measured signal in NMR and is referred to as the Free Induction Decay (FID). The FID encodes the information about the nuclear spins of a sample, such as their resonance frequencies, relaxation behavior, and their relative abundance. To disentangle the x and y components of  $M_{x,y}$ , the time domain FID signal  $s(t)$  is acquired as oscillating exponentially damped complex signal comprised of  $s_x(t)$  and  $s_y(t)$  using quadrature detection (de Graaf, 2007):

$$\begin{aligned} s(t) &= s_x(t) + i \cdot s_y(t) \\ &= s_0 \cdot \exp\left(-\frac{t}{T_2^*}\right) \cdot (\cos(\omega_0 \cdot t + \phi) + i \cdot \sin(\omega_0 \cdot t + \phi)) \\ &= s_0 \cdot \exp\left(-\frac{t}{T_2^*}\right) \cdot \exp(i \cdot (\omega_0 \cdot t + \phi)) \end{aligned} \quad (2.9)$$

The time signal is characterized by the following parameters:  $s_0$  denotes the signal amplitude at  $t = 0$ , signal decay occurs according to the time constant  $T_2^*$ ,  $\omega_0$  is the resonance frequency (see also Eq. 2.6) and  $\phi$  is the phase shift between  $\vec{M}_{x,y}$  and receiver coils at the beginning of the signal acquisition ( $t = 0$ ). The time signal is seldomly used for data analysis, and thus the FID is finally converted to a complex frequency spectrum  $S(\omega)$  by using Fourier transform (FT):

$$S(\omega) = \int_{-\infty}^{+\infty} s(t) \cdot \exp(-i \cdot \omega \cdot t) \cdot dt \quad (2.10)$$

Note that Equation 2.9 depicts the time signal of a single Lorentzian resonance in the MR frequency spectrum.

The principle of NMR signal detection by using two receiver coils placed in x and y direction, respectively, is shown in Figure 2.1 together with the corresponding time signal  $s(t)$  (B) and frequency spectrum  $S(\omega)$  (C). The parameters characterizing the FID are also represented in the frequency signal  $S(\omega)$ . The signal amplitude  $s_0$  is equal to the total integrated area of the absorption component of the frequency spectrum. Moreover, the signal appears at its resonance frequency  $\omega_0$ . Additionally, the linewidth (FWHM, Full Width at Half Maximum) of the absorption component of the Lorentzian frequency signal is inversely proportional to  $T_2^*$ :

$$FWHM = \frac{2}{T_2^*} \quad (2.11)$$

Finally, at the beginning of the acquisition ( $t = 0$ ) the detected FID can reveal a phase

offset  $\phi$  (zero-order phase error) between the orientation of the transverse magnetisation vector  $\vec{M}_{x,y}$  and the receiver coils. No phase offset results in an absorption line of the real part frequency spectrum  $\text{Re}\{S(\omega)\}$  and a dispersion line of the imaginary part  $\text{Im}\{S(\omega)\}$ . In contrast, a nonzero phase leads to a mixture of absorption and dispersion components of both  $\text{Re}\{S(\omega)\}$  and  $\text{Im}\{S(\omega)\}$  (see Fig. 2.1 bottom) and complicates the identification of the signal characterizing parameters. However, phase offsets can be corrected retrospectively by applying an appropriate phase correction.

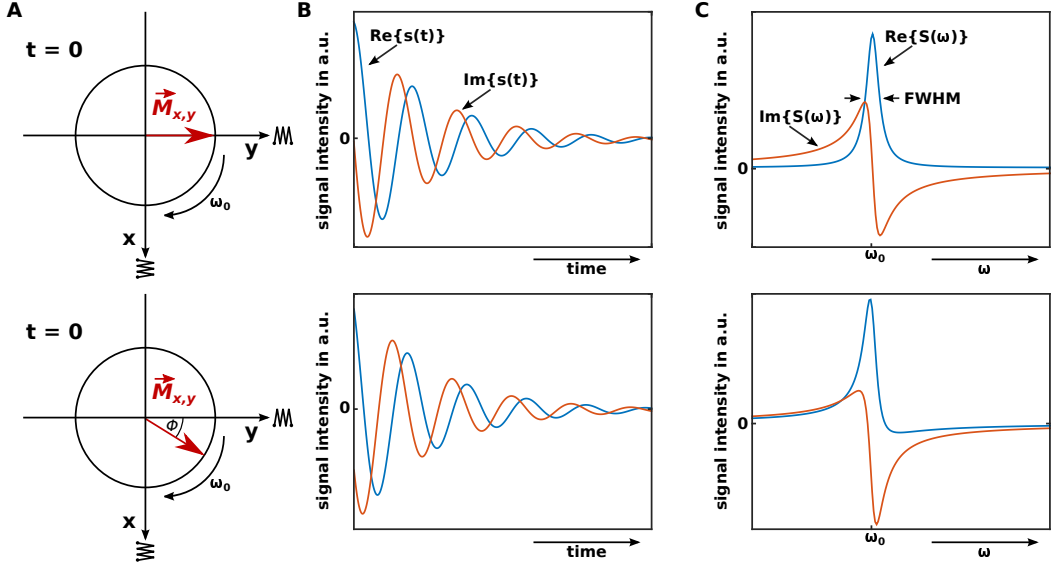


Figure 2.1: (A) Principle of NMR signal detection with two receiver coils placed in x and y direction with  $\vec{M}_{x,y}$  revealing no phase shift (*top*) and a nonzero phase shift  $\phi$  (*bottom*) relative to y at  $t = 0$ .  $\vec{M}_{x,y}$  rotates with  $\omega_0$  in the x,y-plane inducing a voltage in the receiver coils<sup>1</sup>. (B) Depiction of the real part (Re) and imaginary part (Im) components of an exemplary FID time signal  $s(t)$  decaying exponentially with  $T_2^*$ . (C) Corresponding real part and imaginary frequency spectrum  $S(\omega)$  showing a single Lorentzian peak at the resonance frequency  $\omega_0$ . The absorptive and dispersive components are separated in the real and imaginary part of the frequency spectrum for a phase offset  $\phi = 0$ , whereas a mixture of both are contained in  $\text{Re}\{S(\omega)\}$  and  $\text{Im}\{S(\omega)\}$  for a nonzero  $\phi$ . The subplots B and C were adapted from de Graaf (2007).

As a final remark, the above introduced linewidth FWHM of frequency signals represents an important spectral parameters describing spectrum quality. As introduced in section 2.1.2 long  $T_2^*$  time constants are preferred resulting in narrow linewidths. Additionally, it has to be noted, that MRS data acquisitions usually comprise multiple repetitions to improve the signal-to-noise ratio (SNR) by averaging due to typically low brain metabolite concentrations of only few millimolar and interfering noise originating from the receiver technology. Moreover, using multi-channel receiver coils and

<sup>1</sup>The vectorial notation of the Larmor frequency is given by  $\vec{\omega}_0 = -\gamma \cdot \vec{B}_0$ . Thus, for nuclei with positive  $\gamma$  and  $\vec{B}_0 \parallel z$  the z component of  $\vec{\omega}_0$  is negative, leading to a clockwise precession (Levitt, 2008).

appropriate weighted coil channel combination (Sandgren et al., 2005) can distinctly improve the SNR. Thus, the SNR represents an additional major spectral parameter in NMR characterizing data quality and is directly proportional to the square root of the number of acquired scans (NAS), to the investigated volume  $V$ , and to the signal amplitude  $s_0$ :

$$SNR \sim \sqrt{NAS} \cdot V \cdot s_0 \quad (2.12)$$

Note, that  $s_0$  equals to  $|\vec{M}_0|$  for a perfect 90 deg. pulse. However, the latter only holds for single-shot acquisitions or for experiments that allow for full recovery of the longitudinal magnetisation, thus measuring with long repetition times TR. Since the measurement time can dramatically be increased by the acquisition of multiple MRS scans to achieve sufficient SNR, time efficiency and available signal  $s_0$  are commonly compromised by shortening TR. Consequently, in such measurements the saturated reduced  $M_z$  component of  $|\vec{M}_0|$  is measured and replaces  $s_0$ .

## 2.2 MR spectroscopy

Proton MR spectroscopy of the human brain enables the observation of spectral information of a variety of brain metabolites from a specific volume. The underlying principles of chemical shift and J-coupling are briefly introduced in the following section. Next, the J-difference editing technique MEGA-PRESS will be presented that allows the detection of GABA. Finally, signal quantitation from the acquired MR spectra will be described. The content of the sections 2.2.1 to 2.2.4 is based on the book of de Graaf (2007).

### 2.2.1 Chemical shift

The so far introduced principles of nuclear magnetic resonance have been described considering only one type of nuclear spin of a certain resonance frequency  $\omega_0$ . Fortunately, the resonance frequency  $\omega_0$  does not only depend on the applied magnetic field strength  $B_0$  and the gyromagnetic ratio  $\gamma$ , but is also sensitive to the chemical environment of the nucleus. This is related to the surrounding electrons that induce, e.g., a magnetic field opposite to the applied static magnetic field  $\vec{B}_0$  according to Lenz's law (Lenz, 1834). Thus, the effective magnetic field strength experienced by the nucleus is effectively reduced, which is also termed shielding. Therefore, protons bound in different molecular structures reveal different resonance frequencies  $\omega'_0$  in the proton MR spectrum:

$$\omega'_0 = \gamma \cdot B_0 \cdot (1 - \sigma) \quad (2.13)$$



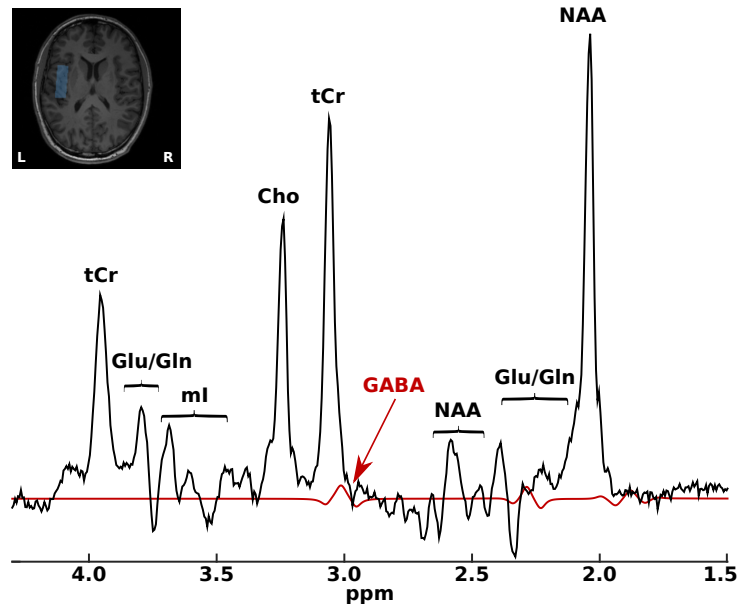


Figure 2.2: Exemplary *in vivo*  $^1\text{H}$  MR spectrum acquired from the insular cortex ( $V = 16$  ml) of a healthy volunteer (Non-edited MEGA-PRESS spectrum,  $\text{TE} = 68$  ms,  $B_0 = 3$  T). The detected brain metabolites are denoted as follows: Cho (choline), Glu (glutamate), Gln (glutamine), mI (*myo*-inositol), NAA (N-acetylaspartate), tCr (total creatine: PCr + Cr). The GABA resonances ( $\gamma$ -aminobutyric acid, red, simulated spectrum) cannot be separated from the spectrum due to its low concentration and strong overlapping by other brain metabolites.

where  $\sigma$  is the shielding constant. The chemical shift,  $\delta$ , is commonly expressed in parts per million (ppm) and referenced against a certain frequency  $\omega_{ref}$ . Thus, in contrast to the resonance frequency  $\omega_0$ ,  $\delta$  is independent of  $B_0$ :

$$\delta = \frac{\omega'_0 - \omega_{ref}}{\omega_{ref}} \quad (2.14)$$

A common substance used for referencing is tetramethylsilane (TMS, resonating by convention at 0 ppm) that reveals a higher  $\sigma$  than most other substances. Since TMS is not present in the human body, the ppm axis relative to TMS is commonly indirectly calculated by, first, selecting an alternative reference of known chemical shift, e.g. the water signal or the NAA resonance, for calculating  $\delta$  and, second, adding the known chemical shift value of this alternative reference with respect to TMS as offset to the calculated  $\delta$ , e.g. 4.7 ppm for water for *in vivo* or 2.01 ppm for NAA.

The effect of chemical shift ultimately allows for the observation of a variety of signals arising from different molecular structures. A typical *in vivo* proton MR spectrum acquired from the human brain at 3 T is shown in Figure 2.2. Isolated resonances from the brain metabolites NAA, creatine (tCr) and choline (Cho) can be easily identified.

Their signals can be used as biological markers in a diseased brain state as they are related to different cellular processes: NAA acts as neuronal density marker, tCr (composed of creatine (Cr) and phosphocreatine (PCr)) reflects the mitochondrial energy turnover, and Cho acts as cell membrane turnover marker (Govindaraju et al., 2000). In contrast, the resonances of GABA (red line in Fig. 2.2) are not only weak due to the comparably low GABA concentration in the human brain of ( $\sim 1\text{-}2\text{ mmol/l}$ ), but also overlapped by a variety of other metabolite signals. Consequently, the detection of GABA with MRS requires the so-called J-difference editing technique to disentangle its signals from other overlapping brain metabolite resonances at clinical field strength ( $B_0 \leq 3\text{ T}$ ) that will be introduced in the following sections.

## 2.2.2 J-coupling

To understand J-difference editing techniques the phenomenon of scalar coupling (J-coupling) of spins within a molecule has to be understood. J-coupling occurs because nuclei with magnetic moments can interact with each other through electrons in the intramolecular chemical bonds of molecules. Coupling can also occur directly through space (dipolar coupling), but can be neglected for *in vivo* MRS measurements since it averages to zero in isotropic liquids due to rapid molecular tumbling.

The coupling via chemical bonds is schematically depicted in Figure 2.3. An uncoupled and a weakly J-coupled proton *AX*-spin system with spin  $1/2$  each are shown. Four different combinations of spin orientations are possible and result in splitting to four different energy levels.  $E_1$  is the lowest energy level with both spins being parallel to the external magnetic field  $B_0$  ( $\alpha\alpha$  state), the high-energy level  $E_4$  corresponding to the antiparallel orientation ( $\beta\beta$  state), and  $E_2$  and  $E_3$  describing mixed orientations of both spins ( $\alpha\beta$  and  $\beta\alpha$  state). In case of an uncoupled spin system, the energy level difference between level  $E_1$  and  $E_3$  is equal to the energy level difference between  $E_2$  and  $E_4$ , thus revealing a single resonance at  $f_A$  (with  $f = \frac{1}{2\pi} \cdot \omega$ ) for nucleus *A*. Similarly, the single peak at  $f_X$  arises from the energy transitions between  $E_1$  and  $E_2$  as well as between  $E_3$  and  $E_4$  for nucleus *X*. In contrast, for a J-coupled *AX* spin system both single resonances at  $f_A$  and  $f_X$  show an additional split. This splitting is due to two physical laws. First, according to the Fermi contact interaction (Fermi, 1930) the antiparallel alignment between the spins of the bound electron and the nucleus is energetically preferred in contrast to a parallel alignment. Second, the Pauli exclusion principle demands that two interacting electrons cannot occupy the same quantum state and thus, in the described case of two binding electrons, they have to differ in their spin quantum numbers resulting again in an antiparallel orientation (Pauli, 1925). Due to the Pauli exclusion principle when the nuclear spins of *A* and

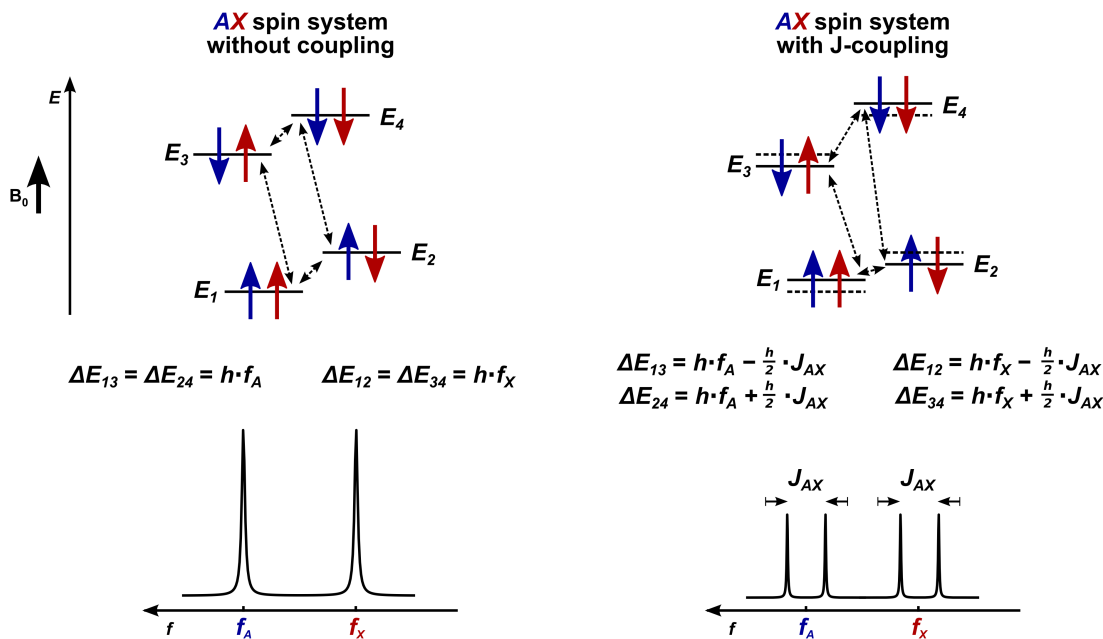


Figure 2.3: Energy level diagram demonstrating J-coupling of a proton  $AX$  spin system with spin  $1/2$ , each. *Left*: No coupling. The two energy transitions for nucleus  $A$  ( $\Delta E_{13}$  and  $\Delta E_{24}$ ) reveal the same frequency,  $f_A$ , and result in a single resonance in the MR spectrum. Analogously for nucleus  $X$ , showing the same frequency  $f_X$  for both transitions  $\Delta E_{12}$  and  $\Delta E_{34}$ . *Right*: Weakly J-coupled spin system. Energy transitions between  $\Delta E_{13}$  and  $\Delta E_{24}$  and between  $\Delta E_{12}$  and  $\Delta E_{34}$  decrease or increase due to the Fermi contact interaction and the Pauli exclusion principle (dashed lines: energy levels for the uncoupled state, see text for more details) and result in splitting of the resonances at  $f_A$  and  $f_X$  into two doublets in the MR spectrum. The frequency difference between the splitted resonances is preset by the scalar coupling constant  $J_{AX}$  that is specific for each molecule. The figure was adapted from de Graaf (2007).

$X$  are aligned parallel to each other, their corresponding bound electron spins cannot occupy the energetically preferred antiparallel state relative to both nuclei, respectively. This, in turn, leads to an increase of the nuclear energy levels  $E_1$  and  $E_4$  compared to the uncoupled state (dashed lines in Fig. 2.3), thus becoming energetically less favorable. Likewise, the energy levels  $E_2$  and  $E_3$  decrease since they become energetically more favorable allowing antiparallel nucleus-electron spin orientations for both  $A$  and  $X$ . The amount of energy level change is preset by the scalar coupling constant  $J$  that is specific for each molecule and results in  $\mp \frac{1}{4} h J_{AX}$ . Notably,  $J$  does not depend on the applied magnetic field strength  $B_0$  and is given in the unit Hz. Moreover, each additional coupling spin results in an additional split of the energy levels, and thus, the number of resonance splittings increases to  $N - 1$ , where  $N$  denotes the number of J-coupled spins.

### 2.2.3 J-coupling evolution

J-coupling between spins is accompanied by the effect of J-coupling evolution of the coupled spin system that occurs following excitation of the spin system. J-coupling evolution during a spin echo experiment is illustrated in Figure 2.4 using vector diagrams for a J-coupled  $AX$  spin system with resonance frequencies  $f_A - \frac{1}{2}J_{AX}$  and  $f_A + \frac{1}{2}J_{AX}$  of spin  $A$  (see Fig. 2.3). Following excitation ( $t = 0$ ), the  $A_X$  spins that are coupled to the  $X$  spin in the lower energy level ( $\alpha$  state) and the  $A$  spins that are coupled to the  $X$  spin in the higher energy level ( $\beta$  state) develop a phase shift  $\phi$  depending on the evolution time, and thus,  $TE/2$ . The non-selective 180 deg. refocusing pulse has two effects. First, the phase shift of  $A_{X=\alpha}$  and  $A_{X=\beta}$  is inverted, respectively, and second, the refocusing pulse inverts the  $X$  spin population, which means that the  $A$  spins that were attached to the  $X$  spins in the  $\alpha$  state are now attached to the  $\beta$  state spins revealing a change of resonance frequency of  $f_A + \frac{1}{2}J_{AX}$  to  $f_A - \frac{1}{2}J_{AX}$  and vice versa (see Fig. 2.4 B at  $t = TE/2$ ). Thus, at the end of the experiment ( $t = TE$ ) the  $A$  spins show a phase shift  $\phi$  depending on  $J_{AX}$  of:

$$\phi = \pi \cdot J_{AX} \cdot TE \quad (2.15)$$

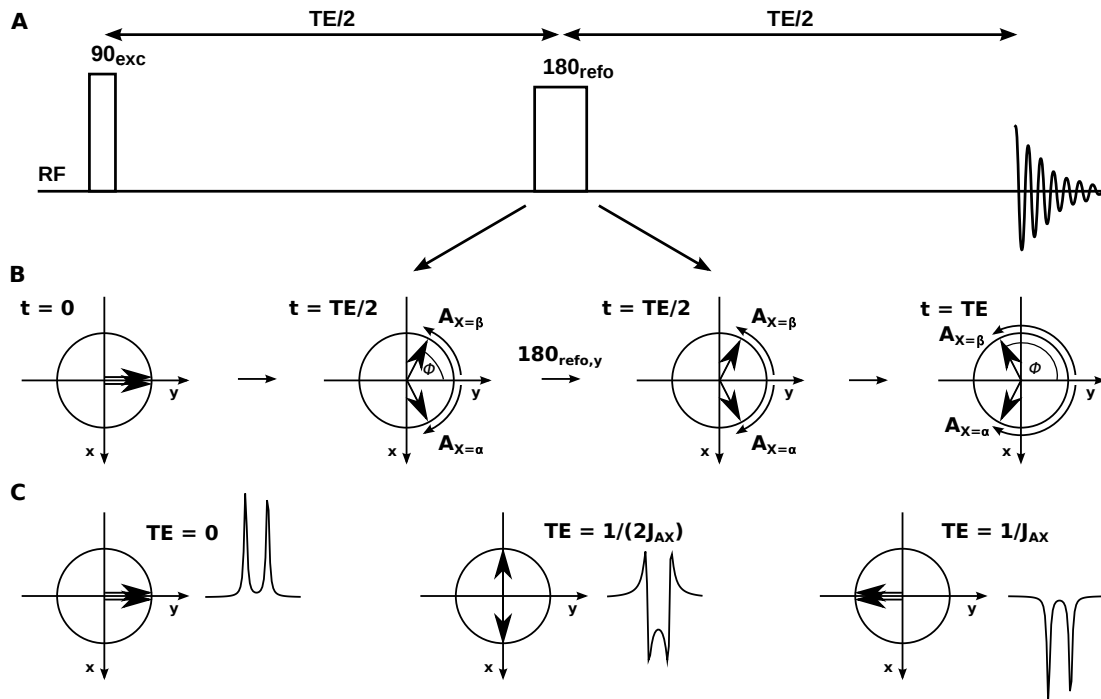


Figure 2.4: (A) Spin echo experiment. (B) J-coupling evolution of spin  $A$  during the experiment of a weakly J-coupled  $AX$  spin system illustrated as vector diagram. (C) Observed frequency spectrum for the  $A$  spin for different values of  $TE$ . See text for more details. The figure was adapted from de Graaf (2007).

Consequently, the spectral doublet pattern reveals an in-phase signal at  $TE = 0$ , an anti-phase doublet at  $TE = 1/(2J_{AX})$  and again an inverted in-phase signal at  $TE = 1/J_{AX}$  ( $\phi = 180$  deg.). Hence, the spectral appearance of a J-coupled spin system can be deliberately modulated by the applied echo time  $TE$ .

## 2.2.4 J-difference editing

Coming back to J-difference editing, this spectroscopic technique exploits the fact that the J-coupling evolution can be reversed when applying an additional frequency selective editing pulse ( $180_{edit}$  deg.) to one of the coupling partners, which shall briefly be demonstrated on the  $AX$  spin system (see Fig. 2.5). As described above, the  $A$  spins reveal a phase shift due to J-coupling evolution after excitation. Then, a frequency selective editing pulse is applied to the  $X$  spins ( $t = TE/4$ ) that inverts the  $X$  spin population. This means that the  $A$  spins that are coupled to the  $X$  spins in the  $\alpha$  state are now coupled to the spins in the  $\beta$  state, which leads to a reversal of the J-coupling evolution. Notably, in contrast to the non-selective  $180$  deg. refocusing pulse the phase shift of the  $A$  spins is not inverted. The following refocusing pulse simply refocuses  $T'_2$  related relaxation processes. J-coupling evolution following after the  $180_{refo}$  deg. pulse is reversed again by the second  $180_{edit}$  deg. pulse and results in in-phase signals at all  $TE$ s. Note, that two editing pulses are applied to eliminate rf-induced phase modulations (de Graaf, 2007).

During a J-difference editing experiment two MRS scans are acquired. The first

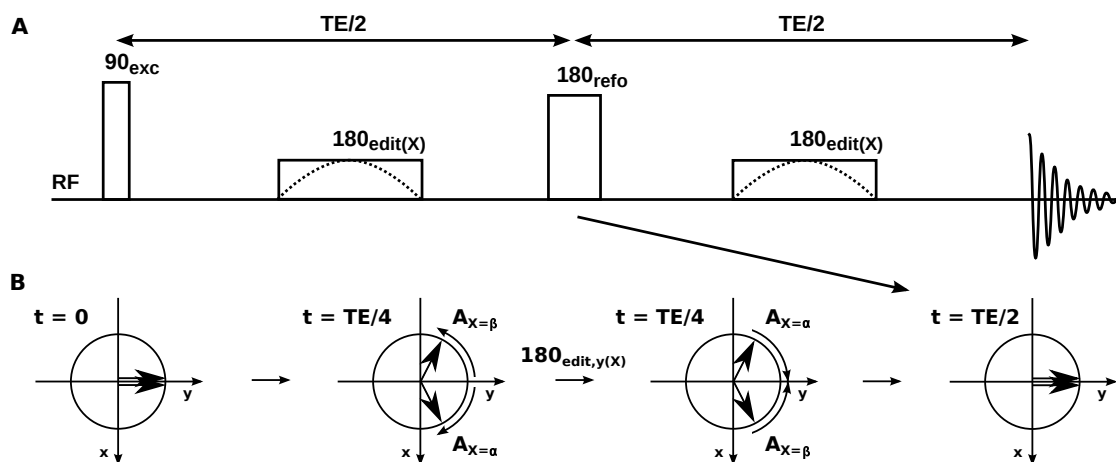


Figure 2.5: (A) Basic J-difference editing sequence containing two editing pulses being frequency selective for the  $X$  spin ( $180_{edit(X)}$ ). (B) Reversal of J-coupling evolution of a weakly J-coupled  $AX$  spin system for the  $A$  spin by frequency selective editing of  $X$  illustrated as vector diagram. See text for more details. The figure was adapted from de Graaf (2007).

experiment is conducted without frequency selective editing pulses (non-edited spectrum, NED), the second experiment with the editing pulses (edited spectrum, ED), which deliberately modulate the spectral appearance of the metabolite spin system of interest. All spins that are unaffected by the  $180_{edit}$  pulses will evolve as during the non-selective experiment (see Fig. 2.4) and are consequently removed by subtracting both MRS scans from each other (difference spectrum, DIFF). Since it is intended to obtain maximal signal of the metabolite of interest in the DIFF spectrum, the chosen echo time TE allows appropriate modulation of the signal structure in the NED experiment. For a weakly J-coupled  $AX$  spin system the optimal TE corresponds to  $1/J_{AX}$  leading to a inverted signal in the NED scan (Fig. 2.4 B), whereas in the ED scan a positive signal is observed (Fig. 2.5 B). Subtraction of both signals from each other ( $ED - NED = DIFF$ ) yields the resonance of interest.

### 2.2.5 $^1\text{H}$ MEGA-PRESS sequence

The  $^1\text{H}$  MEGA-PRESS sequence (Mescher et al., 1998; Mullins et al., 2014) is a common J-difference editing technique for the detection of GABA. GABA can be approximated as a weakly J-coupled  $A_2M_2X_2$  spin system comprising three multiplets that correspond to its methylene groups, resonating at 2.3 ppm (triplet of  $^2\text{CH}_2$ ,  $X$  spins), 1.9 ppm (quintet of  $^3\text{CH}_2$ ,  $M$  spins) and 3.0 ppm (triplet of  $^4\text{CH}_2$ ,  $A$  spins), respectively. The structural formula and the ball-and-stick model of GABA are given in Figure 2.6 C.

The NED scan corresponds to a conventional PRESS acquisition (Point RESolved Spectroscopy) and consists of a 90 deg. slice-selective excitation pulse ( $90_{exc}$ ) and two 180 deg. slice-selective refocusing pulses ( $180_{refo}$ , Fig. 2.7). Simultaneously with these rf-pulses, the magnetic gradient fields  $G_x$ ,  $G_y$  and  $G_z$  are applied presetting the local resonance frequencies, respectively. Thus, a 3D localization of the spectroscopic volume can be achieved and only spins from the intersection volume of all three slices will be detected during acquisition. In the NED scan, the GABA triplet at 3.0 ppm shows inverted outer lines (see Fig. 2.6 B) revealing a "W-shape" due to J-coupling evolution. During the ED scan, the two additional frequency selective  $180_{edit}$  pulses are applied at 1.9 ppm reversing the J-coupling evolution between the GABA protons resonating at 1.9 and 3.0 ppm. As a result, a "regular" pattern of the GABA triplet at 3.0 ppm, pointing upwards, is observed.

Upon subtraction, disturbing signals such as tCr and Cho are removed in the DIFF spectrum, while the outer lines of the GABA triplet at 3.0 ppm (pseudo doublet) remain in the spectrum and are commonly used for GABA quantitation (see Fig. 2.6 A). Besides GABA also the resonances of glutamate (Glu), glutamine (Gln), NAA and macromolecule signals (MM) are co-edited by the frequency selective  $180_{edit}$  pulses

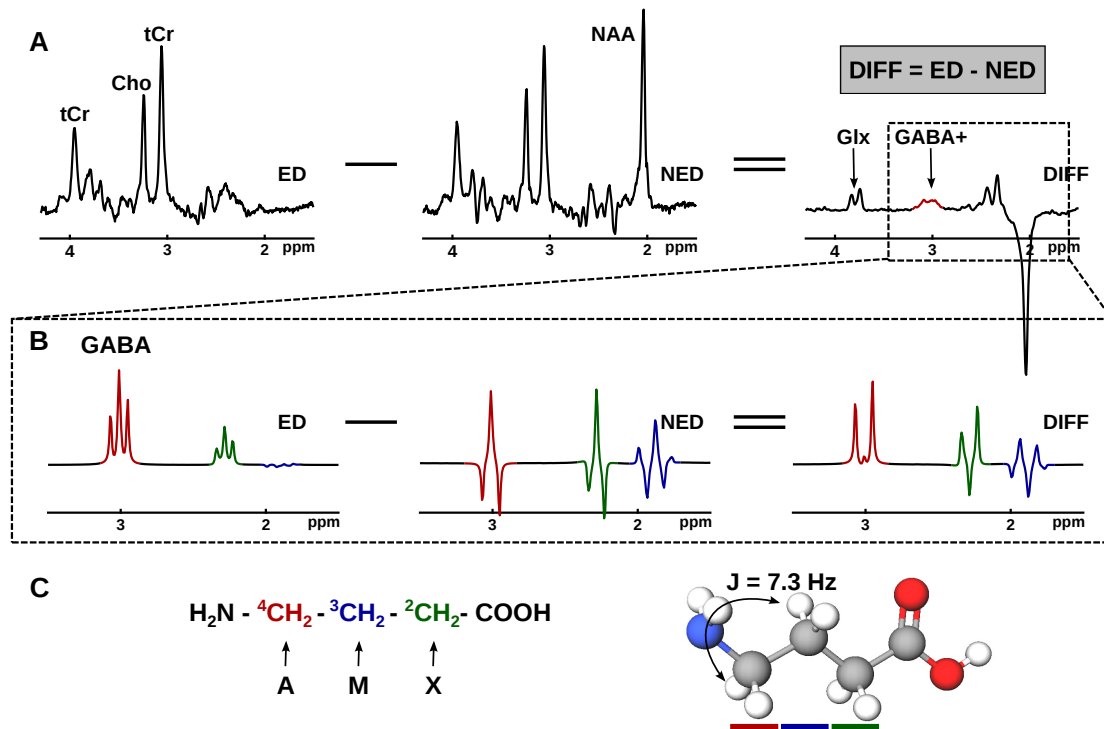


Figure 2.6: (A) *In vivo*  $^1\text{H}$  MEGA-PRESS brain spectra showing multiple resonances overlapping GABA. By applying a frequency selective editing pulse at 1.9 ppm (edited spectrum, ED), the evolution of J-coupling of the GABA spin system is reversed. By subtracting the non-edited scan (NED), the final difference spectrum (DIFF) reveals only the MR signals being affected by the frequency selective editing pulse during ED. (B) Simulated GABA resonances in the MR spectrum (red:  $^4\text{CH}_2$ -GABA triplet, green:  $^2\text{CH}_2$ -GABA triplet, blue:  $^3\text{CH}_2$ -GABA quintet). The J-coupling evolution of the GABA spin system at 3.0 ppm is refocused during the ED scan showing absorption peaks. During NED the outer lines of the GABA signal at 3.0 ppm are maximally inverted ("W-shape"), and subtraction of ED and NED scan reveals a pseudo-doublet of GABA at 3.0 ppm that is commonly used for quantitation. (C) Structural formula of GABA and corresponding ball-and-stick model (color of balls: blue - N, white - H, gray - C, red - O, created with the open-source software MolView<sup>2</sup>). The GABA  $\text{CH}_2$  groups of the  $A_2M_2X_2$  spins system are color-coded according to (B). The figure was adapted from Mullins et al. (2014).

and visible in the DIFF spectrum. Due to the chemical resemblance of Glu and Gln, the composite measure Glx is mostly reported (see also Chapter 4.1) when applying MEGA-PRESS, because the experiment parameters are optimized for the detection of GABA. Note that during NED the frequency selective editing pulses are also present but are applied off-resonant not affecting signals in the MR spectrum (commonly at 7.5 ppm, symmetrically around the water resonance at 4.7 ppm).

As described in section 2.2.3, the applied echo time TE presets the spectral ap-

<sup>2</sup><http://molview.org/>, Herman Bergwerf

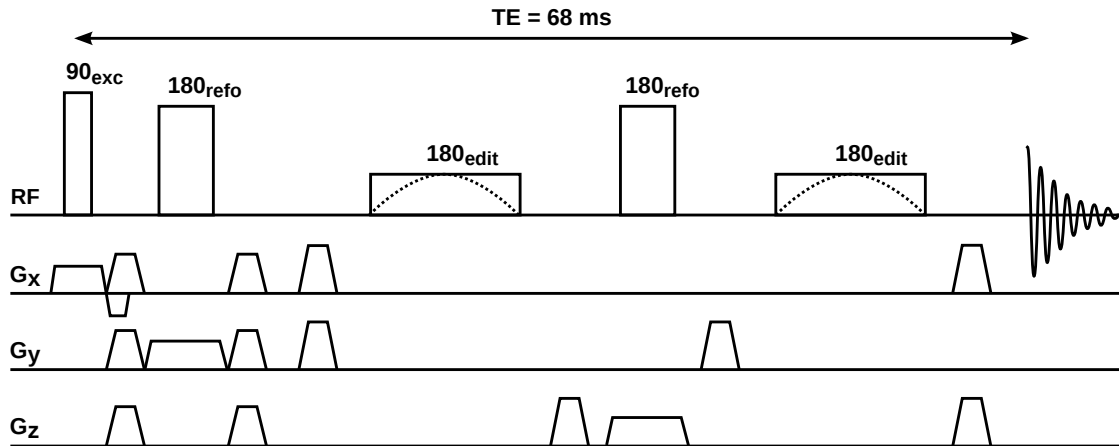


Figure 2.7: Schematic depiction of the  $^1\text{H}$  MEGA-PRESS sequence. The sequence comprises two separate scans. The first scan corresponds to the non-edited spectrum and a common spin echo experiment is performed applying the excitation ( $90_{exc}$ ) and two refocusing pulses ( $180_{refo}$ ). The gradients  $G_x$ ,  $G_y$  and  $G_z$ , which are simultaneously applied to the  $90_{exc}$  and  $180_{refo}$  rf-pulses, allow for localization of the spectroscopic volume. The additional crusher gradients dephase spins that are excited by non-ideal rf-pulses. During the second, edited scan two frequency selective frequency pulses  $180_{edit}$  refocusing the J-coupling evolution of the GABA spin system are additionally applied. Subtraction of the two scans from each other yields the difference spectrum. The echo time TE is optimized for GABA detection at 68 ms. The figure was adapted from Mullins et al. (2014).

pearance of signals of J-coupled spins. During J-coupling evolution of a triplet-like resonance, such as for GABA at 3.0 ppm, the center peak of the triplet reveals no phase shift, but only the outer lines evolve with TE (see Fig. 2.8). It is intended to reveal outer signals that are negative ("W-shape") in the NED spectrum to maximize the difference with the positive (J-coupling reversed) ED spectrum. In contrast to a doublet structure, maximum negative signals are observed at  $TE = 1/(2J)$  (Harris et al., 2017). The coupling constant for the  $^3\text{CH}_2$ -GABA and  $^4\text{CH}_2$ -GABA resonance is  $J = 7.3$  Hz (de Graaf, 2007) and thus results to a commonly used TE of 68 ms for GABA difference editing.

One limitation of the MEGA-PRESS technique is co-editing of a MM resonance at 1.7 ppm by the frequency selective editing pulse at 1.9 ppm. This is problematic, since MM spins at 1.7 ppm are coupled to a MM resonance at 3.0 ppm; thus, at the same frequency as the  $^4\text{CH}_2$ -GABA. Co-editing occurs because of the limited duration of the editing pulse that is restricted since during the TE interval two slice-selective refocusing pulses and the two editing pulses have to be applied. Consequently, the duration of each editing pulse is limited to a duration of  $\sim 14$  ms (Edden et al., 2012b). This corresponds to a frequency bandwidth of 88 Hz at half-width at 1% maximum of the



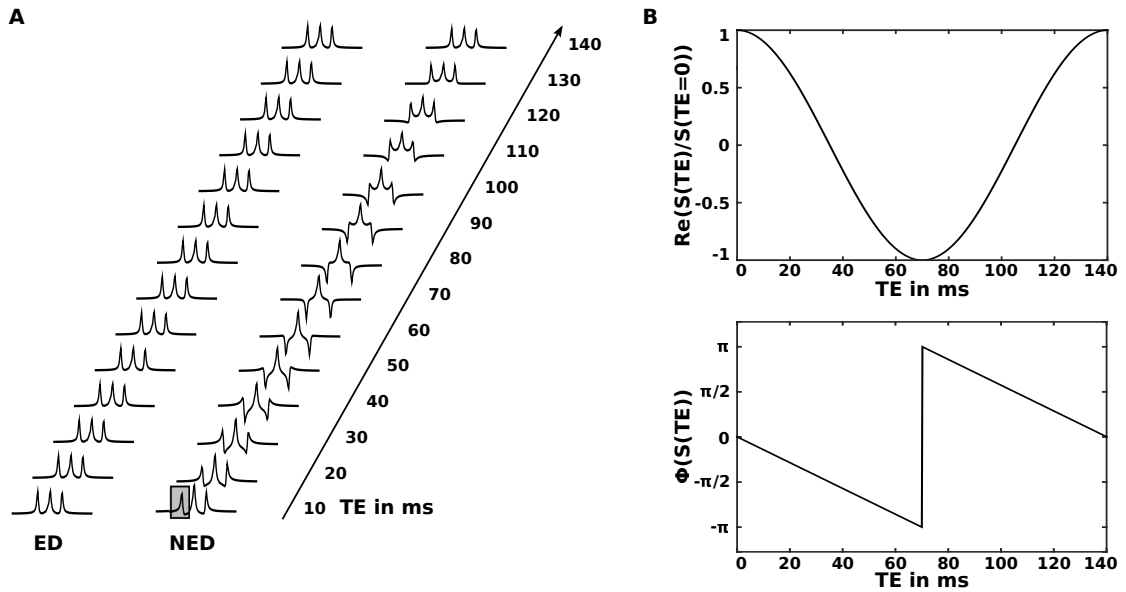


Figure 2.8: (A) J-coupling evolution with TE for a simulated GABA triplet resonating at 3.0 ppm during the ED and NED scan. In the ED scans no phase modulation occurs due to the reversion of the J-coupling evolution by the frequency selective editing pulse applied to the GABA multiplet at 1.9 ppm. For NED, J-coupling evolves with TE showing maximal negative outer wings of the GABA triplet at TE of 68 ms, which corresponds to  $1/(2J)$  with  $J = 7.3$  Hz. (B) Evolution of the normalized frequency signal intensity and signal phase  $\phi$  of the left outer GABA triplet resonance in NED scans (gray square in (A)). According to (A) a minimum of the signal intensity and a maximum negative phase is observed at TE of 68 ms. Relaxation effects were omitted for the sake of simplicity.

typically Gaussian editing pulse (Near et al., 2011) (0.7 ppm at 3 T). The MM signal is consequently partially co-edited due to the frequency distance of approximately 26 Hz at 3 T between the MM and GABA resonances at 1.7 and 1.9 ppm, respectively. The MM signal contributes about 50 % to the observed GABA resonance, which is usually referred to as GABA+. To solve this problem of MM signal contribution, a symmetric editing approach around the MM resonance at 1.7 ppm was proposed by Henry et al. (2001) placing the frequency selective editing pulse during the NED scan at 1.5 ppm (51 Hz frequency distance to 1.9 ppm at 3 T). This allows for an almost equivalent co-editing of the MM resonances during NED and ED, which are then cancelled out in the final DIFF spectrum. However, the symmetric editing approach requires a narrow bandwidth of the editing pulse, since otherwise the GABA intensity is reduced due to editing during both the NED and ED scans. For this purpose, a compromising value of TE of 80 ms was determined, enabling the detection of the GABA signal at 3.0 ppm with a "W-shape" during the NED scan and an editing pulse length of 20 ms (Edden et al., 2012b). The latter results in a half-width at 1 % maximum of 61 Hz (0.5 ppm at 3 T) instead of 88 Hz,

thus reducing GABA editing during the NED scan. However, the main disadvantage of this approach is that the increased frequency-selectivity of the editing pulses is prone to unwanted frequency drifts, which usually occur during MRS acquisitions (Edden et al., 2016; Harris et al., 2015b) (see also Chapter 3). Therefore, the symmetric editing approach was omitted in the studies presented in this thesis. However, this is not a drawback since a main focus of this work was to explore stimulus-induced changes of GABA (and Glx) and a change of MM signals during stimulation is not expected (Mullins et al., 2014).

## 2.2.6 Metabolite signal quantitation

A major signal processing step is the estimation of the metabolite brain levels from the acquired *in vivo* MR spectra since the amplitudes of the acquired signals are directly proportional to the number of spins contained in the spectroscopic volume and thus, to the metabolite and neurotransmitter concentrations. However, the MR signal intensities are given in arbitrary units and are variable between different MR measurements due to differences in e.g. excitation homogeneity or load of the receiver coils. Consequently, normalization with an appropriate reference is required to allow for comparisons between measurements or subjects.

### Quantitation software jMRUI

The simplest way to determine resonance intensities (or areas under the peaks) is numerical integration over the corresponding frequency range, which is only feasible for isolated resonances, and thus not applicable to *in vivo* MR brain spectra that comprise a variety of overlapping metabolite signals. A widely used quantitation software for *in vivo* MR spectra is the AMARES fitting routine (Vanhamme et al., 1997) included in the open source software package jMRUI (Stefan et al., 2009). AMARES performs fitting of the complex FID (see Eq. 2.9) and considers *a priori* knowledge constraints of the user. Model parameters for each fitted signal can be predefined including frequency, phase, linewidth and lineshape (Lorentzian or Gaussian), either fixed or using soft constraints to allow for estimation of the corresponding signal intensities.

Example fits of a NED and DIFF spectrum can be seen in Figure 2.9. Signal intensities of the isolated resonances (see also Fig. 2.2) of tCr, NAA and Cho were determined in the NED spectrum by fitting each metabolite to a single Lorentzian peak. In the mean DIFF spectrum GABA+ was fitted by a Lorentzian triplet at 3.0 ppm to consider contributions from the center peak (Mullins et al., 2014) while fixing the linewidths within the signal structure but keeping the amplitudes adjustable. The

relative frequency shifts of the signal triplet were fixed based on the coupling constant of  $J = 7.3$  Hz. The signal structure of Glx at 3.75 ppm was fitted by a Lorentzian doublet, using again fixed linewidths within the signal structure and adjustable amplitudes.

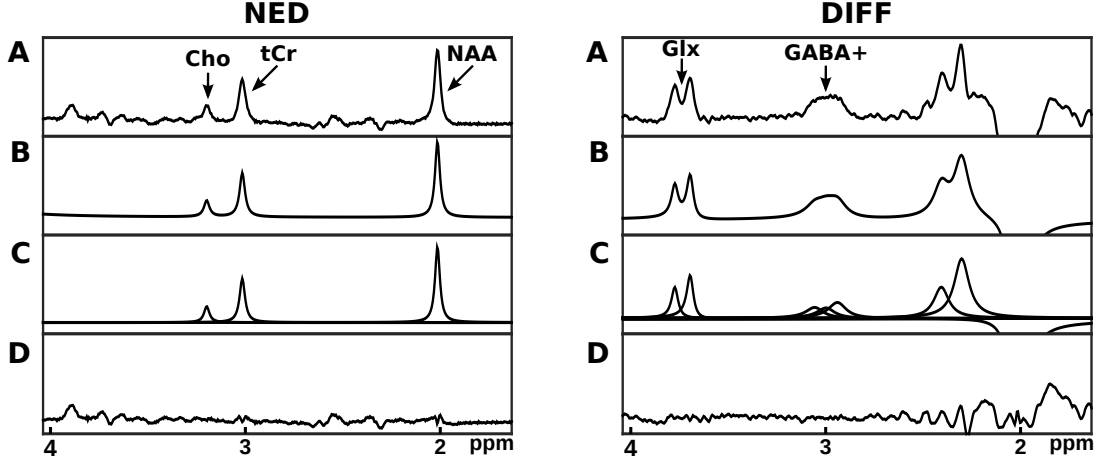


Figure 2.9: Example fits of AMARES for NED and DIFF spectra showing (A) the original spectrum, (B) the estimated fits, (C) the single components and (D) the fit residuals. For all fitted peaks Lorentzian shapes were used. Cho, tCr and NAA were determined as single peaks in the NED spectrum. GABA+ was fitted by a triplet and Glx by a doublet in the DIFF spectrum.

### Accounting for relaxation effects

The relaxation times constants  $T_1$  and  $T_2$  introduced in section 2.1.2 are specific for each metabolite, but also depend on brain tissue, such as gray (GM) or white matter (WM). Thus, by correcting the signal by transverse and longitudinal relaxation related signal attenuations for each metabolite allows an improved approximation of the non-relaxed signal that, in turn, is proportional to the true underlying metabolite concentration. Each single metabolite intensity  $I_{met}$  can be corrected by using the following expression (Gasparovic et al., 2006; Gussew et al., 2012):

$$I_{met} = \frac{I_{met,jMRUI}}{f_{WM} \cdot R_{met,WM} + f_{GM} \cdot R_{met,GM}} \quad (2.16)$$

with

$$R_{met,x} = \exp\left(-\frac{TE}{T_{2,met,x}}\right) \cdot \left(1 - \exp\left(-\frac{TR}{T_{1,met,x}}\right)\right) \quad (2.17)$$

where  $f_{WM}$  and  $f_{GM}$  are the WM and GM fractions in the MRS voxel, respectively, and  $R_{met,x}$  ( $x = GM, WM$ ) describes the  $T_1$ - and  $T_2$ -related attenuations (see also Eq. 2.7). Brain matter fractions of GM, WM and cerebral spinal fluid (CSF) can be determined from an anatomical MR imaging scan by using fully automated open source segmentation

toolboxes as implemented, e.g., in the image processing toolbox Freesurfer<sup>3</sup>. Since metabolite intensities only arise from WM and GM, the fraction of CSF can be neglected for relaxation correction of metabolite signal intensities.  $T_1$  and  $T_2$  values (see Tab. 2.1) for NAA, tCr, Cho and Glx have been reported by Mlynárik et al. (Mlynárik et al., 2001), Zaaraoui et al. (Zaaraoui et al., 2007) and Choi et al. (Choi et al., 2010). In case of GABA+, only the composite  $T_1$  and  $T_2$  time constants for GM and WM (Edden et al., 2012a; Puts et al., 2013) are known and were consequently used in the analysis.

Metabolite	$T_1$ in s		$T_2$ in s	
	GM	WM	GM	WM
NAA	1.470	1.350	0.226	0.264
tCr	1.460	1.240	0.137	0.155
Cho	1.300	1.080	0.207	0.202
Glx	1.200	0.960	0.161	0.169
GABA	1.310	1.310	0.088	0.088

Table 2.1: *In vivo* relaxation time constants  $T_1$  and  $T_2$  for selected metabolites in gray (GM) and white matter (WM) at  $B_0 = 3$  T.

### Internal referencing

Since the proportionality factor between quantified metabolite signal amplitude and absolute metabolite concentration is not known, the metabolite measures are generally reported relative to an internal reference. Metabolites with physiologically stable concentrations, such as creatine, or tissue water measured in the same spectroscopic volume can be used as concentration reference. The latter has the disadvantage to require a separate scan, which might be affected by subject motion (Jansen et al., 2006; Mullins et al., 2014). Additionally, referencing to the creatine signal, which can be quantified from the NED spectrum of the same MEGA-PRESS scan, proved to produce more reliable results (Bogner et al., 2010) and its concentration is not expected to change due to stimulation. Moreover, its main resonance at 3.0 ppm is within the metabolite signal range and chemical shift displacement issues are reduced compared to when referencing to water resonating at 4.7 ppm. Chemical shift displacement occurs due to the frequency-dependent slice-selection. Hence, the excited volumes depend on the chemical shifts of particular metabolites, leading to a mismatch of spatial origins of different signals in the spectrum. Nevertheless, referencing to water might be preferred in studies exploring diseased brain states because the Cr concentration may be affected.

<sup>3</sup>V 4.5.0, <http://surfer.nmr.mgh.harvard.edu/>



in turn, is then released to be taken up by neurons, forming again Glu (Rae, 2014). Since 60 – 70% of Glu is restored from Gln, this cycling between Glu and Gln is closely linked to neurotransmission (Mangia et al., 2012). However, the *de novo* synthesis of Glu requires intermediates from the TCA cycle (Rae, 2014) and, hence, is regulated to some degree by metabolism. Its relation to metabolism is even intensified since Glu cannot directly be restored by the presynaptic neuron. Therefore, Glu cannot be classified as either neurotransmitter or metabolite only.

As a final remark, even with Glu being present with relatively high concentrations in the human brain, it cannot be distinguished from glutamine by applying the MEGA-PRESS approach, which is optimized for GABA detection at clinical magnetic field strengths of  $B_0 \leq 3$  T. Therefore, the composite measure Glx is mostly reported. To which amount the Glx signal in MEGA-PRESS difference spectra is composed of Glu and Gln has not been fully resolved yet. In contrast to Glu, only little is known about the relation of Gln to brain function. It has been reported with a concentration of 4 – 6 mmol/l (Rae, 2014) and as described above, is synthesized from Glu, but is also an intermediate product from Glu released during neurotransmission.

### 2.3.2 GABA

GABA is involved in various processes in the human brain. However, its major function is the GABAergic inhibition acting in an antagonist manner to the excitatory neurotransmitter Glu (see Fig. 2.11). Being synthesized from Glu in the presynaptic GABAergic neuron (green), GABA is transported in vesicles and released into the synaptic cleft, similarly to Glu. Accordingly, GABA either binds to postsynaptic receptors or is restored by a high-affinity protein GABA transporter back to the presynaptic neuron where its main fraction re-enters the vesicular pool or, to a lesser extent, enters the TCA cycle. Binding of GABA to the postsynaptic membrane leads to a hyperpolarization of the membrane potential by allowing efflux of positive potassium ions as well as influx of negatively charged chloride ions. Moreover, a small fraction of the extracellular GABA also enters the adjacent astrocytes to generate Gln, either directly from a previous conversion of GABA to Glu or after entering the TCA cycle. Subsequently, Gln is released to be taken up again by the presynaptic neuron and converted to Glu to metabolize GABA either directly from Glu or via Glu leaving the TCA cycle, and being finally available for the vesicular pools or the TCA cycle. Thus, both Gln and Glu serve as precursors of GABA. However, in contrast to Glu, only a small GABA portion contributes to the metabolic pool (Patel et al., 2005; Stagg et al., 2011b; Walls et al., 2015) as its main fraction is directly restored by the postsynaptic neuron.

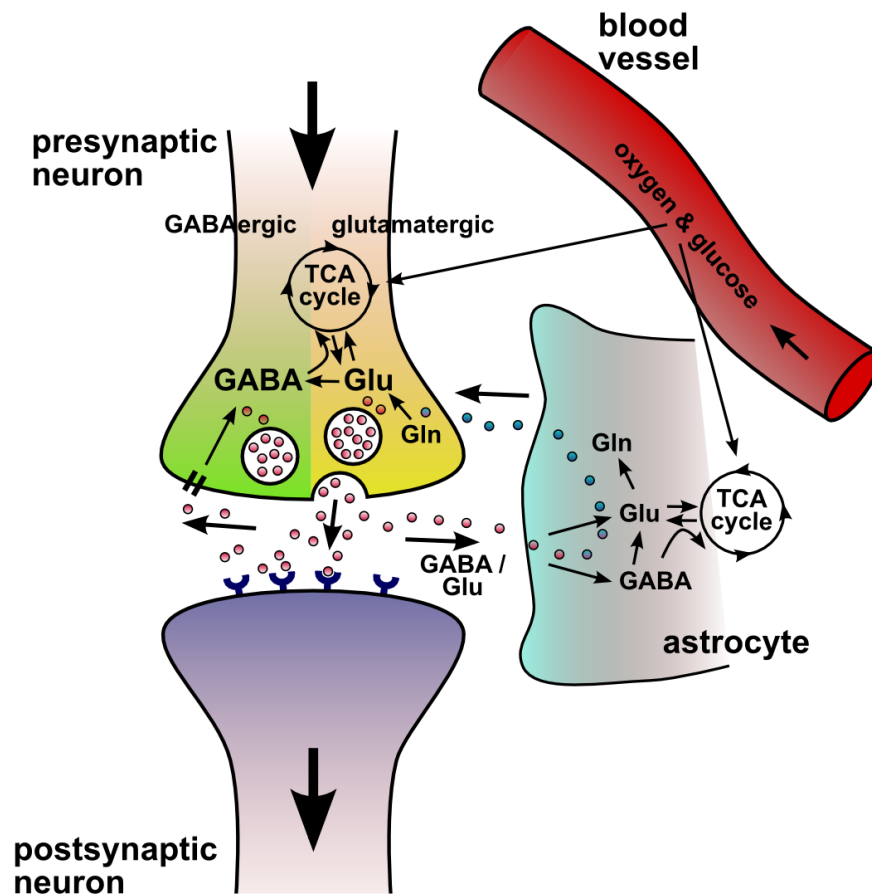


Figure 2.11: Chemical signal transduction between two neurons. Neurons can either be inhibitory (green, GABAergic) or excitatory (yellow, glutamatergic). The neurotransmitters GABA and Glu (red) are stored in vesicles in the presynaptic boutons and are released into the presynaptic cleft when an electric action potential has to be transduced (bold black arrow). The neurotransmitters then bind to specific receptors located in the cell membrane of the postsynaptic neuron affecting the membrane potential. In case of depolarization a new action potential is generated and is further transported to the next cell. Remaining neurotransmitters are consecutively removed from the synaptic cleft. GABA can be restored directly by the presynaptic neuron or is, similar to Glu but to a minor fraction, taken up by astrocytes (cyan). In the astrocytes both metabolites are converted to Gln (blue) directly or after entering the TCA cycle. Gln is then released to be restored by the presynaptic neuron to form Glu and GABA, either directly or, again, after entering the TCA cycle. Glu and GABA are then available for neurotransmission while being stored in vesicles or can re-enter the TCA cycle. Moreover, cerebral blood flow in adjacent blood vessels provides glucose and oxygen required for the TCA cycle and is closely linked to neurotransmitter cycling to compensate required energy demands. This interrelation is known as neurovascular coupling. The figure has been adapted from Mangia et al. (2009) and Patel et al. (2005).

In conclusion, it has to be noted, that when applying MR spectroscopy only total concentrations of GABA and Glu are detected in a certain volume and that MRS cannot

distinguish between neurotransmitter or metabolic pools. Moreover, the metabolites are differently bound in those pools and less "visible" to MRS when stored in vesicles. However, as discussed above and also indicated by recent findings, the GABA levels measured with MRS can predominantly be ascribed to the neurotransmitter GABA fraction (Stagg et al., 2011b), whereas the measured Glu concentration is more strongly related to metabolism.

## 2.4 Functional MR imaging

The following sections give a brief introduction to functional magnetic resonance imaging (fMRI). While MR spectroscopy focuses on the identification of a variety of chemical compounds by exploiting the chemical shift, magnetic resonance imaging (MRI) is based on the varying spatial density and relaxation properties of water protons between tissue compartments, such as GM, WM and CSF in the brain, and thus enables imaging of anatomy. Moreover, brain activity results in altered relaxation behavior, which is exploited in fMRI. The underlying physiological mechanisms are introduced, and the principle of fMRI data acquisition is described together with the required analysis steps.

### 2.4.1 BOLD effect

As described in section 2.3, signal transduction in the brain is directly related to neurotransmission of GABA and glutamate. Thus, when responding to an external stimulus the neuronal firing rates in corresponding task-specific brain regions increase and lead to elevated glucose and oxygen consumption rates to fulfill the raised energy demand (Shulman and Rothman, 1998). An accompanying effect of this altered energy demand due to neuronal activity changes is the hemodynamic response, which is mediated via the neurovascular coupling (see also Fig. 2.11, TCA cycle). In detail, fMRI exploits the change in  $T_2^*$  relaxation times due to the dynamic transient change in the oxygenation level of blood that is described as BOLD (Blood Oxygenation Level Dependent) effect (Ogawa et al., 1990a; Ogawa and Lee, 1990; Ogawa et al., 1990b). One would assume that during activation the amount of desoxygenated blood increases, but the increased energy demand is indeed overcompensated by fresh incoming oxygenated blood. The varying levels of blood oxygenation cause a change of magnetic susceptibility, and are thus related to changes of  $T_2^*$ . Desoxyhemoglobin is paramagnetic whereas oxyhemoglobin is diamagnetic, and consequently the latter has a longer  $T_2^*$  value, which is associated with an elevated MR signal magnitude compared to desoxygenated blood. This activation related modulation of  $T_2^*$  is exploited in fMRI experiments. An exemplary time course of the hemodynamic response function (HRF) to an external



stimulus is depicted in Fig 2.12 A. The observed BOLD signal change due to a stimulus is expected to be very small being in the range of only a few percent.

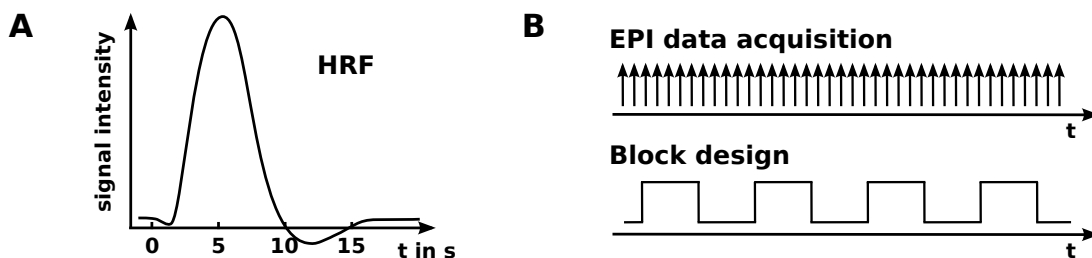


Figure 2.12: (A) Hemodynamic response function (HRF) describing the BOLD signal change due to a stimulus at the time point  $t = 0$ . The HRF shows, first, an initial dip after 1-2s that is related to the stimulus-induced blood deoxygenation. Second, the HRF reveals an overshoot due to incoming oxygenated blood ( $t = 5-6$  s) followed by a post-stimulus undershoot before returning to baseline. (B) Schematic fMRI data sampling over time using a block design stimulation with alternating baseline and stimulus conditions.

## 2.4.2 fMRI data acquisition

MR spectroscopy and MR imaging differ in terms of the preparation and detection of the FID. In MRS, the signal is typically acquired from a single voxel of a comparably large volume in the range of  $\text{cm}^3$ . In contrast, MRI allows spatial encoding of volumes comprised of multiple voxels with a spatial resolution in the millimeter range. Decoding of the spatial information is performed during reconstruction and is based on appropriate preparation of the acquired FIDs. The spatial information along  $x$ ,  $y$  and  $z$  is imprinted to the FID in three steps. First, slice-selection along  $z$  is performed similarly to MRS by superimposing the static magnetic field  $\vec{B}_0$  with a magnetic field gradient  $G_z$  during rf-excitation with a certain bandwidth. Second, the spatial encoding along  $y$  axis is achieved by superimposing the static magnetic field with an additional field gradient  $G_y$  prior to the signal acquisition. Thus, the protons are precessing with different frequencies depending on  $y$ . After switching off  $G_y$ , the spins continue to precess, again with same frequencies, but with a relative phase offsets depending on their position along the  $y$  axis, which is called phase encoding. To encode all spatial frequencies in  $y$  direction the integral of the phase encoding gradient  $G_y$  is varied with each acquired FID. Third, frequency encoding is conducted along the  $x$  direction by applying an additional field gradient  $G_x$  during the FID acquisition (readout gradient), which induces a variation of the Larmor frequency depending on the spins position along the  $x$  axis.

Functional MRI techniques commonly acquire rapid series of consecutive brain images at rest and during induced activation, either in block or event-related fashion

(Blamire et al., 1992; Dale and Buckner, 1997) by using  $T_2^*$ -weighted imaging sequences with echo planar readouts (EPI, (Mansfield, 1977)).  $T_2^*$ -weighting can be achieved by the usage of gradient echos instead of producing spin echos as described in section 2.1.2. Gradient echoes are produced by initially dephasing the  $M_{x,y}$  magnetisation with a magnetic field gradient. Following, the spins are refocused again by using a magnetic field gradient of inverted polarity that generates an echo. This approach does not refocus  $T_2'$  as in spin echo experiments, and thus, is sensitive to  $T_2^*$  variations. Additionally, EPI readout is used to realize fast, single-shot image encodings. In contrast to more conventional MRI acquisitions that require multiple phase-encoding steps to allow for the coverage of the spatial object information<sup>4</sup> commonly realized by conducting consecutive rf-excitations, EPI conducts all phase encoding steps after only one single rf-excitation pulse while successively generating multiple gradient echoes. As the available FID signal within an EPI echo train is limited by  $T_2^*$  relaxation, the resolution of the acquired image is limited to allow for the acquisition of all required object information within one rf-excitation. Additional acceleration, and thus, improved spatial resolution can be achieved by the application of parallel acquisition approaches, such as GRAPPA (Griswold et al., 2002), which utilizes the spatially heterogeneous sensitivity profiles of receiver coil elements. EPI images are typically obtained with a spatial resolution of 2 to 3 mm and can be acquired with a temporal resolution between 1 to 3 s while covering the whole brain.

### 2.4.3 From fMRI data to BOLD activation maps

In the following section, the analysis of EPI time series is described for images acquired during a block design stimulation (see Fig. 2.12 B). Several processing steps have to be carried out to obtain functional activation maps by using appropriate tools provided, for instance, with the widely used SPM (Statistical Parametric Mapping) software package<sup>5</sup> (Ashburner and Friston, 1997; Worsley and Friston, 1995). An overview over each step is depicted in Figure 2.13. First, object shifts that are related to motion of the subject's head during the measurement have to be corrected (Fig. 2.13 A). To this end, the EPI image time-series are spatially realigned with the time averaged EPI image using rigid-body transformation (translation and rotation for each direction in space x, y and z, respectively). Because EPI slice images are acquired consecutively, the hemodynamic response function (HRF) in each slice is timely shifted relative to an applied stimulus (Fig. 2.13 B). Slice time correction is achieved by shifting the EPI

<sup>4</sup>Referring to k-space. A detailed introduction is beyond the scope of this thesis and can be found in the works of Brown et al. (2014) and Vlaardingerbroek and den Boer (2003).

<sup>5</sup>Versions used: SPM8, SPM12; <http://www.fil.ion.ucl.ac.uk/spm/>

signal in time using the first acquired slice as reference. Moreover, the EPI time series are spatially smoothed by convolving the 3D EPI image volume with a 3D Gaussian kernel of defined FWHM (commonly 5-8 mm, see Fig. 2.13 C), which corresponds to a weighted spatial averaging of adjacent voxels. Smoothing results, first, in noise suppression, and second, in improvement of validity of the applied statistical tests (Friston et al., 1996; Worsley and Friston, 1995). Finally, the intensity fluctuations in the EPI time-series are statistically evaluated by applying a general linear model (GLM (Worsley and Friston, 1995)) that models the observed signal variation as a linear combination of different signal components (Fig. 2.13 D):

$$y = \beta_1 \cdot x_1 + \beta_2 \cdot x_2 + \epsilon \quad (2.18)$$

Thereby,  $y$  denotes the empirical observed BOLD signal time course in a single image voxel,  $x_1$  represents the predictor or regressor containing information about the applied paradigm (baseline (value 0) *vs.* stimulation (value 1) conditions) convolved with the hemodynamic response function and  $x_2$  is the constant term of the regression (value 1). The  $\beta_i$  values correspond to the parameter estimates obtained from the regression and  $\epsilon$  denotes the estimated error term. The defined regressors ( $x_i$ ) are pooled in the so-called design matrix (single columns) together with the number of sampled data points in the time dimension (rows). By applying appropriate statistical hypothesis testing (t-test) it is evaluated whether the observed signal fluctuation ( $y$ ) in each voxel is systematically related to the paradigm ( $x_1$ ). Thus, a statistical parametric map is obtained that, in turn, allows - by applying a defined significance threshold  $p$  - to determine if the observed activation in a particular voxel is significant.

Finally, a map of BOLD signal changes (BOLD in %) can be calculated by voxel-wise dividing the  $\beta_1$  by the  $\beta_2$  estimates (Bednařík et al., 2015):

$$\text{BOLD} = \left( \frac{\beta_1}{\beta_2} \right) \cdot 100 \quad (2.19)$$

The described data analysis has to be conducted separately for each single subject and is also known as first-level analysis. Moreover, comparisons across multiple subjects are typically performed to determine paradigm related effects in a group of subjects (group analysis or second-level analysis). However, to allow for comparisons across multiple subjects, the single subject data have to be transformed to a standard brain (MNI space<sup>6</sup> (Evans et al., 1993)) to account for anatomical differences between subjects. To this end, standardized SPM routines are used to perform a spatial nonlinear transformation

---

<sup>6</sup>Standard brain from the Montreal Neurological Institute of McGill University Health Care

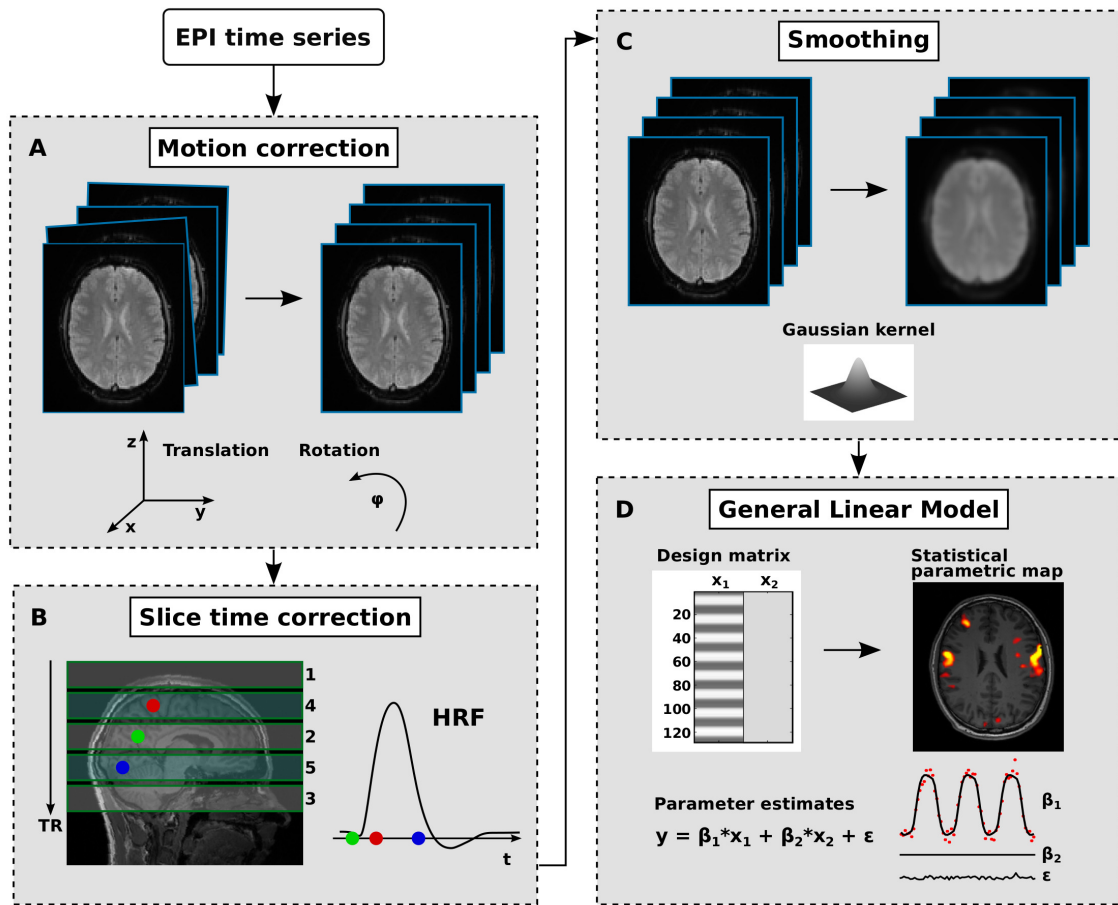


Figure 2.13: Processing pipeline of EPI series using SPM by applying (A) motion correction, (B) slice time correction of slices acquired in an interleaved fashion, (C) smoothing and (D) general linear model. Exemplary statistical parametric maps are mapped onto a transverse anatomical high resolution MP-RAGE scan. The color encodes the statistical power of the activation patterns. More details are given in the text.

of the EPI series into the MNI space.

Finally, some statistical aspects have to be considered. It has to be kept in mind that the statistical data evaluation applying the GLM is performed for each single voxel of the EPI brain images. EPI images often comprise more than 100 000 brain voxels that, in turn, corresponds to 100 000 performed GLM regressions. Selecting a typical significance threshold of  $\alpha = 0.05$  (or  $p < 0.05$ ) means to allow for 5% false positive results (type I errors). Applying the same significance threshold to all 100 000 performed tests results, on average, in 5 000 false positive results.

A common approach to reduce the number of type I errors for multiple comparisons is the Bonferroni correction that divides the selected significance threshold  $\alpha$  by the number of performed analyses that corresponds to the number of voxels. However, this method

is only applicable to independent comparisons, which is not the case for brain activation maps since neighboring voxels are expected to be physiologically related to each other, and the dependence between neighboring voxels is even increased by the applied data smoothing. Thus, the number of independent observations is much smaller than the number of voxels, making the Bonferroni correction excessively conservative. Therefore, an alternative approach is to consider a reduced number of independent observations in fMRI data to correct the significance threshold  $\alpha$  for multiple comparisons in an appropriate manner by using the so-called resolution elements (resels, (Schneider and Fink, 2007; Worsley et al., 1992)). The resolution elements can be calculated by dividing image volume by the smoothness of the data ( $V/(\text{FWHM}_x \cdot \text{FWHM}_y \cdot \text{FWHM}_z)$ ). Thus, assuming a smoothness of 5 voxels in each dimension for the example given above, the resolution elements result in 800 independent comparisons. This approach is also known as family wise error correction (FWE). Moreover, the FWE correction can be applied in two manners, differentiating between voxel- and cluster-level corrections. The voxel-level correction permits each voxel to be detected as significant whereas cluster-level corrections are based on the statistical inference between neighboring voxels, thus a minimum number of expected voxels  $k_E$  per cluster has to be taken into account (Friston et al., 1996). The type of correction applied to a dataset is variable depending on several aspects, as e.g. sensitivity of the experiment or the hypothesis that shall be tested. Proper usage, however, is currently still not clear-cut and controversially discussed (Bender and Lange, 2001; Eklund et al., 2016; Lieberman and Cunningham, 2009; Rothman, 1990). However, in cases of explorative analyses, the application of significance thresholds  $\alpha$  that are not corrected for multiple comparisons (uncorrected) at voxel-level in combination with cluster-level correction might be advantageous, since stringent corrections for multiple comparisons lack in the artificial increase of false negative results (type II errors). The application of an uncorrected significance threshold  $\alpha$  at voxel-level in combination with cluster-level correction is reasonable as false positive results will be randomly distributed throughout the brain, and thus, are much less likely to occur in voxel clusters (Lieberman and Cunningham, 2009).

# Chapter 3

## Post-processing of MR spectra

In the present chapter, an overview on the required post-processing steps for analyzing MRS data is given. First, common steps for processing MRS raw data will be described, including zero-filling, frequency and phase correction and water peak extraction, whose basic principles can be applied to a variety of MR spectra. In the case of MEGA-PRESS spectra, however, an additional processing step is required that comprises the alignment of mean NED and ED spectra. In the course of this work, a new automatic approach, difference optimization, was developed that minimizes subtraction artifacts in the final DIFF spectrum, which is presented in the second part of this chapter. This new approach was evaluated by applying it to simulated and *in vivo* data. The associated post-processing pipeline was implemented in MATLAB<sup>1</sup>. Parts of this chapter have been published previously as an article (Cleve et al., 2017d) and presented at national (Cleve et al., 2016b) and international conferences (Cleve et al., 2017c).

### 3.1 Post-processing pipeline

Since brain metabolites usually cannot be detected from single-shot spectra due to their low concentrations, averaging of repeated MRS measurements is required to improve SNR (see Eq. 2.12), which typically results in measurement times of several minutes. Hence, long measurement times lead to sensitivity against instabilities between single MRS scans, such as subject factors (e.g., movement, respiration, cardiac cycle) and hardware instabilities (e.g.,  $B_0$  drifts, scanner heating due to the application of magnetic field gradients, timing jitters) (Bogner et al., 2014; Evans et al., 2013; Harris et al., 2014). These measurement instabilities result in frequency and phase errors,  $\Delta f$  and  $\Delta\phi$ , jitters or drifts that have to be corrected for all scans to optimize the spectral resolution in the corresponding average spectrum (i.e. the separation of spectral

---

<sup>1</sup>2014b, The MathWorks, Natick, MA

peaks), and consequently to improve sensitivity, which is limited by the SNR and peak linewidths. In particular, when applying MEGA-PRESS spectroscopy, NED and ED spectra are measured separately. Thus, occurring errors lead to slight differences between NED and ED that, if not accounted for, result in subtraction artifacts arising from creatine or choline signals and, in turn, severely hamper GABA quantitation or make it even impossible (Bogner et al., 2014; Evans et al., 2013; Harris et al., 2014). Thus, before calculating the final DIFF spectrum, the mean NED and ED spectrum have to be matched with respect to their frequency and phase. However, as NED and ED spectra reveal a different spectral fingerprint, the identification of frequency and phase differences is complicated, because common correction methods exploit similarity of the acquired MR signals, e.g. by comparing the spectral appearance of isolated peaks.

### 3.1.1 Zero-filling

Zero-filling increases the digital resolution of the frequency spectrum, which corresponds to an increased number of spectral nodes within a given frequency range, and consequently improves the accuracy of parameter estimation. This can be achieved by simply adding zeros to the end of the FID before performing the discrete Fourier transform. The frequency sampling points are spaced at intervals defined by the inverse product of the number of acquired FID points ( $N_{Samp}$ ) and the selected sampling dwell time, which is the inverse of the sampling bandwidth. Thus, assuming an FID signal acquired with a common  $N_{Samp} = 2048$  and a sampling bandwidth of  $BW = 2000$  Hz results to frequency distance of  $BW/N_{Samp} = 0.98$  Hz between adjacent data points. Indeed, digital resolution could be improved by either decreasing  $BW$  or increasing  $N_{Samp}$ , but these procedures may induce aliasing effects ( $BW \downarrow$ ) or increase the relative noise in the spectrum ( $N_{Samp} \uparrow$ ) since the metabolite signal decreases with the time due to relaxation effects, and thus, the acquired signal will only contain noise at the end of the acquisition. Nevertheless, the latter can be exploited by artificially increasing the number of FID points by adding zeros to the time signal. Thus, by performing zero-filling,  $N_{Samp}$  is commonly doubled or at maximum increased fourfold without affecting the acquired signal since it does not add more information to the data. Thus, coming back to the given example, increasing  $N_{Samp}$  from 2048 to 8192 results in a reduced spacing between the frequency sampling points of 0.24 Hz, as depicted in Figure 3.1 A. However, when applying zero-filling it has to be considered that the acquired time signal has to contain the fully decayed FID.

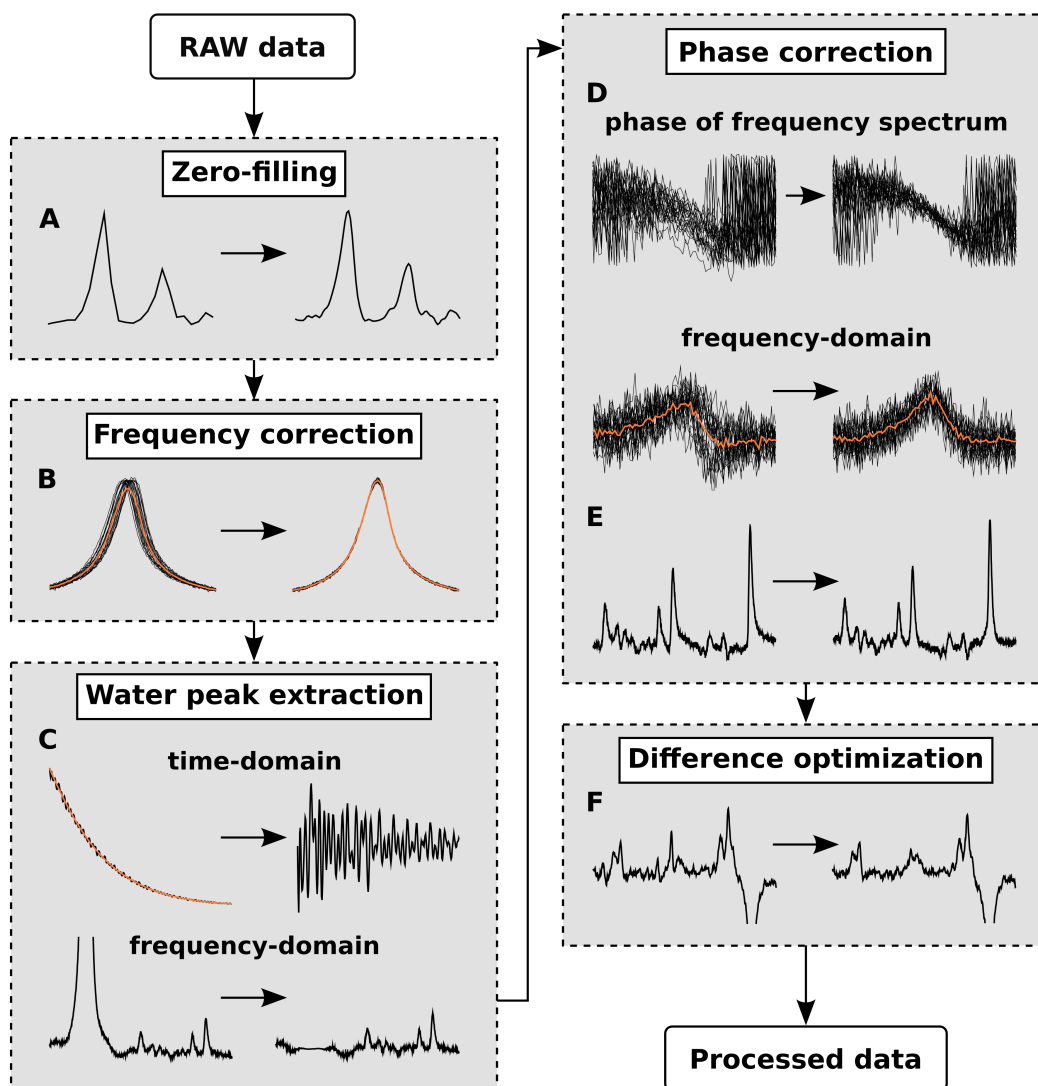


Figure 3.1: Post-processing pipeline for  $^1\text{H}$  MEGA-PRESS spectra. (A) Zero-filling: Improvement of digital resolution by adding zeros to the end of the FID signal. (B) Frequency correction: Correction of frequency drifts using the reduced suppressed water signal as reference signal. Mean curves (orange lines) demonstrate an increased signal intensity after correction. (C) Water peak extraction: Extracting the water resonance from each FID signal by applying a Savitzky-Golay smoothing filter (orange line) demonstrates reliable water signal removal in the frequency spectrum. (D) Phase correction between consecutive scans: Zero-order phase correction leads to increased signal intensity in the corrected mean spectrum (orange line) by minimizing the spectral phase dispersion around the creatine resonance. (E) Phase correction of mean NED spectrum: By comparing real part and magnitude NED spectrum any remaining zero-order offset can be eliminated leading to pure absorption lines. (F) Difference optimization: Automatic elimination of subtraction artifacts in the final DIFF spectrum by frequency and phase matching of mean NED and ED spectra.



### 3.1.2 Frequency correction

The correction of frequency drifts is important for MR spectra optimization because, as previously mentioned, measurement instabilities cannot be avoided in MR experiments. During MR spectrum acquisitions, the rf-transmitter frequency is centered on a predefined frequency, such as the water resonance at 4.7 ppm (*in vivo*), and drifts result in varying offsets between the constant rf-transmitter frequency and the drifting center frequency. Averaging multiple spectra each with slightly different position along the frequency axis leads to artifactual broadening of the observed peak and signal reduction and, thus, hampers the discrimination between separate resonances. Therefore, a dominant signal resonance, which is discriminable from noise in single spectra is commonly used to correct for those occurring offsets  $\Delta f$ . The developed MRS processing pipeline uses the weakly suppressed water signal in the MR spectra for correction of  $\Delta f$ . To this end, the windowed - limited to the range around the water resonance - magnitude water peak of each spectrum is shifted along the frequency axis until it matches the water signal in the first spectrum (reference) by multiplying the inversely Fourier transformed spectrum  $S(f)$  with different frequency offsets  $\Delta f$ :

$$S^*(f) = FFT \{ FFT^{-1} \{ S(f) \} \cdot exp(-i \cdot 2\pi \cdot \Delta f \cdot t) \} \quad (3.1)$$

$S^*(f)$  denotes the modulated frequency signal. Thereby, optimum frequency alignment ( $\Delta f_{opt}$ ) between the reference spectrum and each consecutive single MR spectrum was determined by applying an algorithm based on nonlinear regression implemented in the MATLAB toolbox. In case of MEGA-PRESS spectra, frequency correction of single NED and ED spectra was performed separately. The effect of frequency correction can be seen in Figure 3.1 B demonstrating an increased signal intensity in the mean spectrum of the corrected signal.

### 3.1.3 Water peak extraction

Even if the weakly suppressed water signal is useful for reliable frequency correction, the water peak still reveals high intensity compared to the metabolite peaks and can lead to baseline distortions, and thus, might affect metabolite quantitation. Therefore, removing the water resonance from each single MRS scan prior to averaging might be crucial to improve the quantitation accuracy.

In the current pipeline, a Savitzky-Golay smoothing filter (Savitzky and Golay, 1964) was used for water peak extraction that preserves the high metabolite frequencies. The filter performs a regression with a polynomial of order  $N$  of the complex FID  $s(t)$

with a window size  $n$  with the center at  $t_i$ :

$$p(t) = \sum_{k=0}^N a_k \cdot t^k \quad \text{with} \quad t = [t_{i-\frac{n-1}{2}}, \dots, t_i, \dots, t_{i+\frac{n-1}{2}}] \quad (3.2)$$

$p(t)$  is the polynomial determined from the fit,  $a_k$  are the coefficients of the polynomial and  $t$  represents the interval of the FID time points included in the fit. The polynomial value  $p(t_i)$  corresponds then to the smoothed data point at  $t_i$ . Consequently, the smoothing was performed for each single data point of the FID ( $N_{samp}$ ). For extraction of the water signal  $s_{wat}(t)$  from the FID,  $N$  was chosen to a value of 2 while using a window size of  $n = 103$ . The filtering process of the whole FID was repeated three times to minimize unintended metabolite signal removal. Finally, the extracted water signal was subsequently removed from each single NED and ED scan (Fig. 3.1 C):

$$s^*(t) = s(t) - s(t)_{wat} \quad (3.3)$$

$s^*(t)$  denotes the modulated FID signal.

### 3.1.4 Phase correction

As described in Chapter 2.1.3, the acquired complex FID signal might exhibit a nonzero phase shift  $\phi$ . These so-called zero-order phase errors are unwanted since they complicate the metabolite signal estimation from the frequency spectrum. Moreover, the phases  $\phi$  can differ between consecutive scans, e.g. due to subject movement. If not accounted for, these zero-order  $\phi$  errors result in partial signal cancellations and lead to reduced SNR in the averaged spectrum. Whereas the residual water peak is widely used to correct for frequency drifts, the phase of the water resonance can respond in an unpredictable manner to the applied water suppression technique and is, thus, not suitable to correct phase differences between single scans. Besides water, the Cr resonance at 3 ppm is also often used to correct MEGA-PRESS data because it is - in contrast to NAA - in both NED and ED spectra. However, Cr has low SNR compared to the water peak, which hampers the determination of the Cr phase in the frequency spectrum. Alternatively, besides investigating frequency or time domain signal patterns, the corresponding signal phases may be directly exploited to correct zero-order phase shifts. The phase of the frequency spectrum reveals a defined linear course around the resonance frequency of isolated peaks (see Fig. 3.1 D). In turn, multiple scans without any zero phase differences should show identical phase courses whereas phase errors lead to offsets along the vertical axis. Therefore,  $\phi$  alignment between single MR scans was performed in the phase spectrum ( $\angle$ ) of the complex-valued frequency spectrum. To this end,

phase modulation was applied to the complex frequency spectrum  $S(f)$  as follows:

$$S^*(f) = S(f) \cdot \exp(-i \cdot \Delta\phi) \quad (3.4)$$

The  $\Delta\phi_{opt}$  was obtained by minimizing the spectral phase dispersion individually for consecutive NED and ED spectra in a limited range around the creatine peak at 3 ppm ( $f_{Cr}$ ):

$$sum_{\angle}(\Delta\phi) = \sum_{f_{Cr}} |\angle(\overline{S}^*(f)) - \angle(S^*(f))| \quad (3.5)$$

$$sum_{\angle, opt} = \min(sum_{\angle}(\Delta\phi)) \quad (3.6)$$

The reference  $\overline{S}^*(f)$  used for the minimization problem is the corresponding mean spectrum and was recalculated for each iteration step while minimizing  $sum_{\angle}(\Delta\phi)$ .

However, this method does only allow for correction of phase differences between single scans, but does not eliminate a possibly remaining absolute zero-order phase offset. The best spectral resolution in MR spectra is achieved in an absorption mode spectrum with no zero-order  $\phi$  error in the averaged real part frequency spectrum (Fig. 3.1 E). Therefore, in a second phase correction step, remaining zero-order  $\phi$  errors of the mean NED spectrum following averaging were determined by performing  $\phi$  modulation (see Eq. 3.4) by maximizing the Pearson's correlation coefficient  $R$  calculated between the mean real part and mean magnitude frequency NED spectrum,  $\text{Re}(\overline{S}_{NED}^*(f))$  and  $|\overline{S}_{NED}(f)|$ , as the latter is independent of zero-order  $\phi$  errors. Optimal  $\Delta\phi$  was obtained for a maximal Pearson's correlation coefficient  $R(\Delta\phi)$ . The corresponding zero-order  $\Delta\phi_{opt}$  correction value was then applied to both mean NED and ED spectra. A separate zero-phase correction of ED is not advantageous since it lacks the prominent NAA peak.

A special case of phase errors is caused by so-called eddy currents. Eddy currents occur due to rapid gradient switching that induce time-varying magnetic fields superimposing  $\vec{B}_0$  and decay during the acquisition of the FID. This, in turn, causes a time varying phase  $\phi(t)$  of the metabolite spins that results in lineshape distortions of the detected peaks. However, by acquiring an additional non-suppressed water scan from the same volume using the same sequence parameters, this can be easily corrected since the measured resonances reveal the same  $\phi(t)$  errors. Thus, the metabolite FID can be corrected by modulating the signal with the opposite water signal phase  $-\phi_{wat}(t)$  (Klose, 1990) according to Eq. 3.4.

### 3.1.5 Difference optimization

The so far described post-processing pipeline can be applied with its basic principles to a variety of MR spectra that contain isolated prominent peaks. However, correction

of J-difference editing spectra requires a further processing step - the final frequency and phase alignment of mean NED and ED spectra, which is of major importance for sufficient suppression of subtraction artifacts (see Fig. 3.2) and reliable signal quantitation in the corresponding DIFF spectrum. The previous processing steps, in particular when limited to the creatine resonance at 3 ppm with the underlying GABA resonances, may work insufficiently due to the inequality between NED and ED due to the editing approach, and thus, cannot be directly applied to correct for frequency and phase differences between the two spectra.

The FID-A tool (Simpson et al., 2017) is an open source software package for fully automatic processing of MRS data, including  $^1\text{H}$  MEGA-PRESS spectra as well, that applies the spectral registration method (Near et al., 2015) for frequency and phase correction of consecutive single-shot MR scans as well as for alignment of the mean NED and ED spectra prior to calculating the final DIFF spectrum. The spectral registration method performs nonlinear least squares minimization to fit single scans to a reference scan by adjusting both frequency and phase prior to averaging and proved to perform excellent for single-shot corrections. For aligning the resulting mean NED and ED spectra it also minimizes their complex difference in a least squares sense ( $L^2$  norm based). When calculating the DIFF spectrum, minimization of small subtraction artifacts are of major importance. However, due to its quadratic dependence,

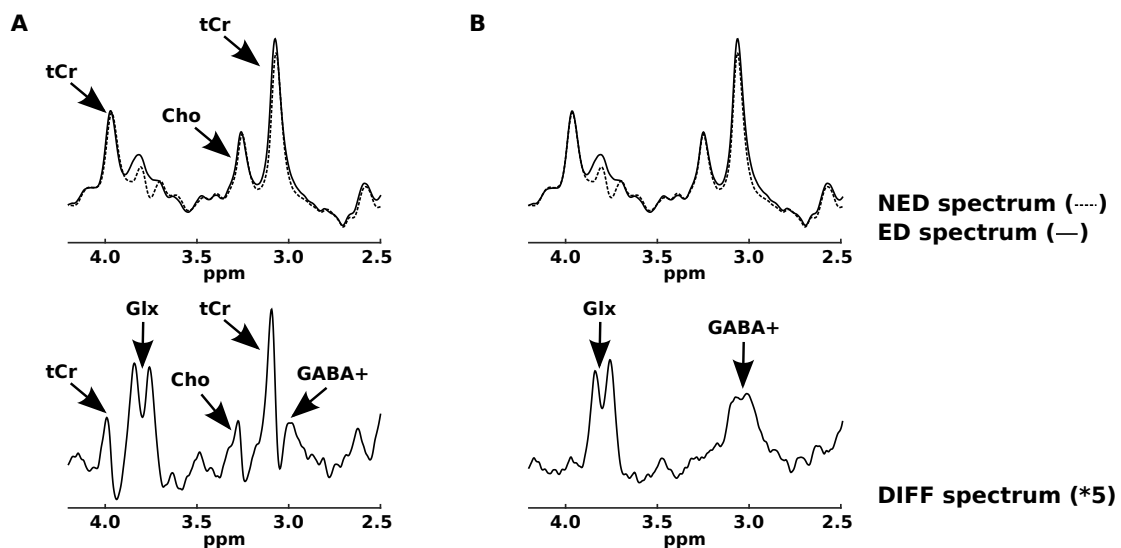


Figure 3.2: Exemplary depiction of subtraction artifacts occurring in the mean DIFF spectrum. (A) No phase and frequency alignment between *in vivo* mean NED (dashed line) and ED (solid line) (*top*) results in severe subtraction artifacts arising from Cho and tCr in the corresponding DIFF spectrum (*bottom*). (B) Correction of relative frequency and phase errors between mean NED and ED leads to elimination of such artifacts and enables reliable quantitation of GABA+ and Glx.

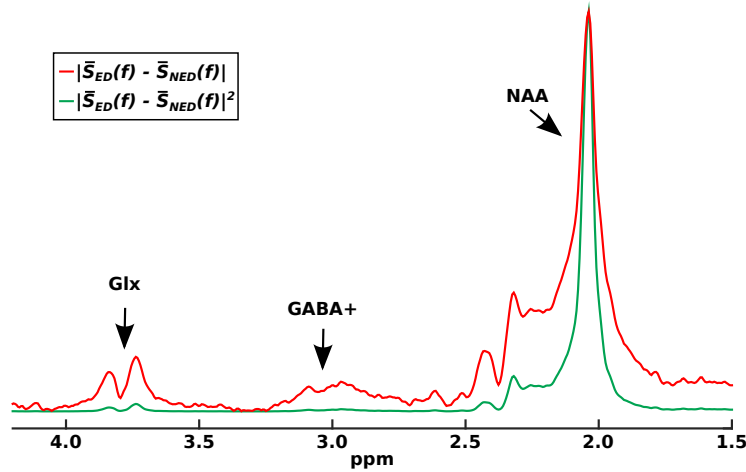


Figure 3.3: Visualization of the  $L^1$  norm (difference optimization, red line) and  $L^2$  norm (spectral registration, green line) based minimization criteria to automatically align mean NED and ED spectra. The red graph shows stronger weighting of small signal contributions, e.g. arising from subtraction artifacts, compared to the green graph. For improved visualization, the intensities of both lines were normalized to their absolute maxima, respectively.

nonlinear least squares minimization weights small signal differences related to those subtle subtraction artifacts less strongly compared to larger signal differences causing potentially inferior results concerning quantitation of metabolites such as GABA (see Fig. 3.3).

Therefore, an alternative method, difference optimization, was developed that applies a linear ( $L^1$  norm) instead of a quadratic ( $L^2$  norm) minimization criterion, which weighs more strongly small differences during the optimization as they are expected to arise from subtraction artifacts in the DIFF spectrum. The difference between the two minimization criteria ( $L^1$  vs.  $L^2$  norm) is visualized in Figure 3.3. Difference optimization aims to minimize the  $L^1$  norm over the complex frequency spectrum (red line), whereas spectral registration is based on the minimization of the  $L^2$  norm (green line). The green graph shows strong impact from the large NAA peak, whereas smaller resonances, such as arising from GABA and Glx, are hardly distinguishable from the baseline. In contrast, signal contributions of low amplitude are clearly visible in the red graph, thus being more weighted when calculating the sum over the  $L^1$  norm (difference optimization) of the complex frequency spectrum compared to when calculating the sum of the  $L^2$  norm (spectral registration).

To automatically align mean NED and ED spectra by using difference optimization, the averaged mean NED spectrum is modulated by multiplying the inversely Fourier transformed spectrum with different frequency offsets,  $\Delta f$  and  $\Delta\phi$ , in the time-domain

(see Eq. 3.1 and 3.4):

$$\bar{S}_{NED}^*(f) = FFT \{ FFT^{-1} \{ \bar{S}_{NED}(f) \} \cdot \exp(-i \cdot 2\pi \cdot \Delta f \cdot t) \cdot \exp(-i \cdot \Delta \phi) \} \quad (3.7)$$

The optimum relative phase and frequency correction between the NED and ED mean spectra is then determined by minimizing the sum of the absolute values of the differences between the complex mean spectra in the frequency domain over the whole frequency range, corresponding to minimizing the norm in the  $L^1$  sense (see Fig. 3.4):

$$sum_{DIFF}(\Delta f, \Delta \phi) = \sum_f |\bar{S}_{ED}(f) - \bar{S}_{NED}^*(f)| \quad (3.8)$$

$$sum_{DIFF,opt} = \min(sum_{DIFF}(\Delta f, \Delta \phi)) \quad (3.9)$$

To determine the optimum frequency  $\Delta f$  and phase  $\Delta \phi$  offsets, the iterative Nelder-Mead Simplex method (Lagarias et al., 1998) was used for minimization, which is an unconstrained nonlinear optimization. Starting values for  $\Delta f$  and  $\Delta \phi$  were both set to zero initially. Moreover, input spectra were apodized by using a 3 Hz exponential damping function to reduce the impact of noise.

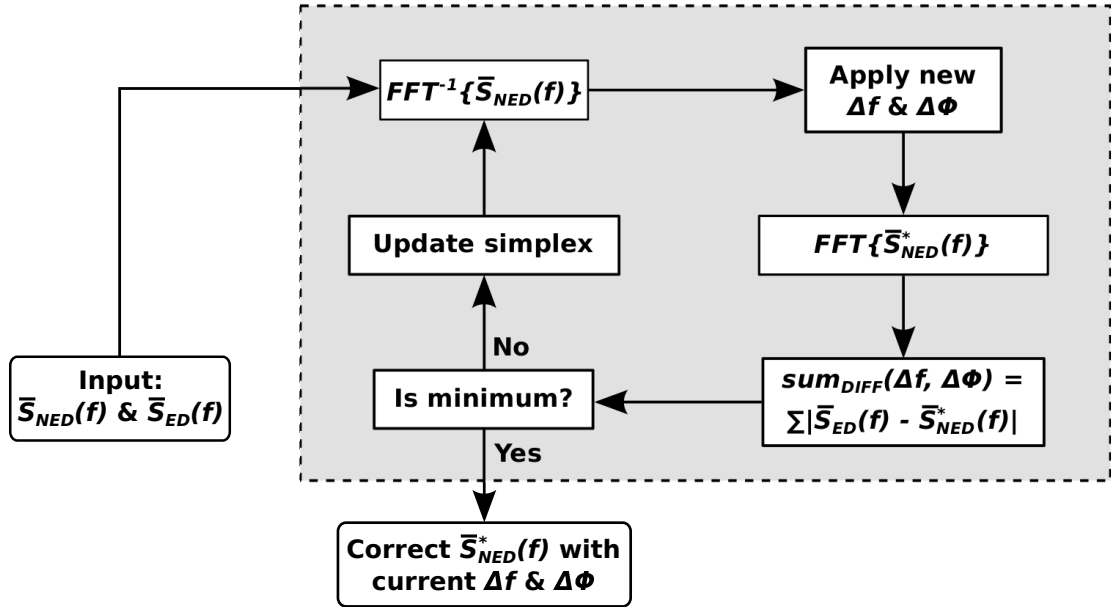


Figure 3.4: Flow chart of automatic alignment of mean NED and ED spectra based on difference optimization.

## 3.2 Applications to $^1\text{H}$ MEGA-PRESS spectra

The described processing pipeline comprises two main parts: First, frequency and phase corrections of single NED and ED scan series, respectively and, second, the final alignment between NED and ED mean spectra in case of J-difference editing. The performance of the new approach of difference optimization was compared with the spectral registration method as implemented in the FID-A toolbox by using simulated MRS data with known frequency and phase shifts between and mean NED and ED spectra as well as *in vivo* data sets. The obtained results are presented in the following sections.

### 3.2.1 Simulations

#### Generation of simulated erroneous brain spectra

In order to evaluate difference optimization, simulated  $^1\text{H}$  MEGA-PRESS data mimicking *in vivo* mean brain spectra were generated assuming perfect frequency and phase drift corrections of single-shot ED and NED scans, respectively. Different preset frequency and phase drift errors were applied between the mean NED and ED spectra. To this end,  $^1\text{H}$  MEGA-PRESS model spectra ( $\text{TE} = 68\text{ ms}$ ,  $2k$  points, spectral width =  $2\text{ kHz}$ ,  $B_0 = 3\text{ T}$ , linewidth =  $6\text{ Hz}$ ) were generated by using the simulation tool included in the FID-A toolbox with 12 metabolites (tCr, GABA, glutathione, Gln, Glu, mI, scyllo-inositol, N-acetyl aspartyl glutamate (NAAG), NAA, phosphocholine, glycerophosphorylcholine). The model spectra were combined to mimic approximately physiological *in vivo* brain concentrations. Different levels of normally distributed noise were then added to the spectra ( $\text{SNR} = [30, 50, 70, 110, 150, 350]$  with respect to the NAA peak). Next, error offsets for frequency ( $-6\text{ Hz}$  to  $+6\text{ Hz}$  in  $1\text{ Hz}$  steps) and phase ( $-6\text{ deg.}$  to  $+6\text{ deg.}$  in  $0.75\text{ deg.}$  steps) were applied to the mean NED spectrum only. Finally, the data were zero-filled to  $4k$ . For each SNR value, spectra generation was repeated 20 times as described above and frequency and phase drift correction was performed with each dataset using the proposed difference optimization algorithm. For comparison, the deliberate misalignment between mean NED and ED spectra was also corrected using the spectral registration method implemented in FID-A. With both correction methods phase and frequency adjustments were made by taking into account the full ranges of input data. To evaluate the performance of both correction methods for the different noise levels, the estimated frequency and phase errors were determined for each correction by calculating the absolute difference between the estimated and the initial preset errors.

## Results

An exemplary simulated DIFF spectrum with and without relative phase and frequency errors between NED and ED is shown in Figure 3.5 (with errors: black line, without errors: red line). Subtraction artifacts of tCr and Cho can be clearly seen in the uncorrected DIFF spectrum. Moreover, a color encoded matrix of the intentionally applied frequency  $\Delta f$  (blue) and phase  $\Delta\phi$  (green) errors is depicted (top left in Fig. 3.5) together with the correction values  $\Delta f$  and  $\Delta\phi$  obtained from the two correction routines for the different SNR levels (bottom in Fig. 3.5). The correction values obtained with difference optimization (A) were in good agreement with the originally applied  $\Delta f$  and  $\Delta\phi$  values at the highest SNR of 350 and revealed only slightly increasing deviations down to a SNR of 70. At the two lowest investigated SNR levels of 50 and 30, the correction values showed expectedly the highest aberrancy. With spectral registration, the correction factors demonstrated larger deviations from the original errors than the proposed difference optimization, which can be seen from the varying symmetry of the

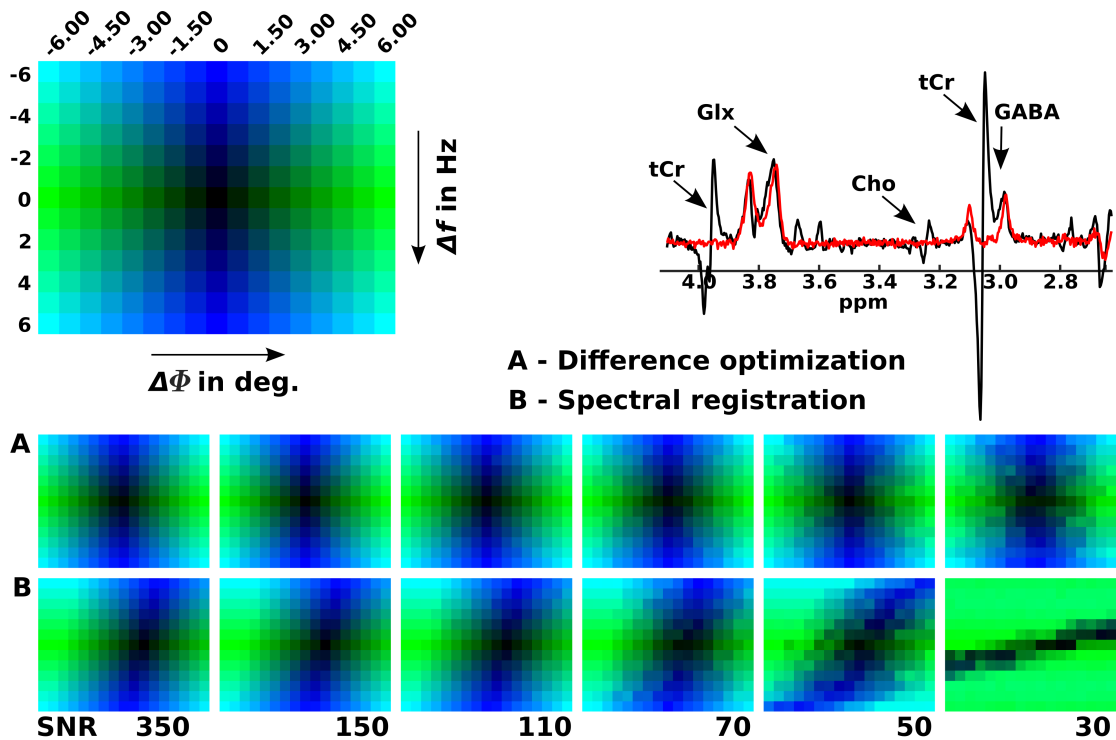


Figure 3.5: *Right top:* Exemplary DIFF spectrum for SNR = 350 without (red line) and with applied  $\Delta f$  (1 Hz) and  $\Delta\phi$  (0.75 deg.) errors between NED and ED (black line). *Left top:* Color encoded matrix of the intentionally applied  $\Delta f$  (blue) and  $\Delta\phi$  (green) error ranges to the simulated spectra at different levels of SNR. *Bottom:* Matrices of correction values  $\Delta f$  and  $\Delta\phi$  obtained by applying difference optimization (A) and spectral registration (B), averaged over all 20 repetitions.



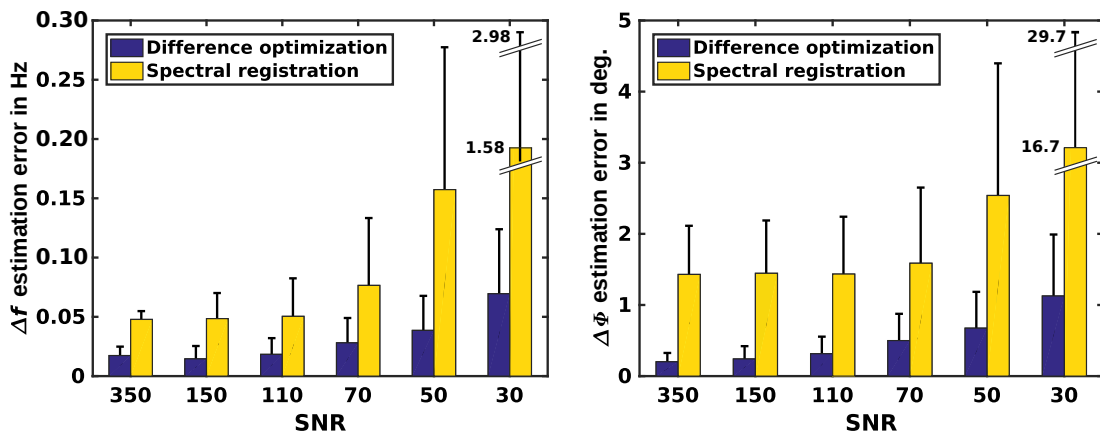


Figure 3.6: Mean frequency  $\Delta f$  and phase  $\Delta\phi$  estimation errors with corresponding standard deviations (bar whiskers) averaged over all repetitions and applied  $\Delta f$  and  $\Delta\phi$  offsets for the difference optimization routine and the spectral registration approach.

color encoded matrices. With decreasing SNR and similar to difference optimization, the discrepancy between the initial and calculated  $\Delta f$  and  $\Delta\phi$  values increased, but revealed larger and unsystematic deviations from the initial error values - as seen in the color gradient in Figure 3.5. Moreover, the increasing deviation of the correction values obtained with spectral registration can mainly be ascribed to inaccuracies in determining the correct  $\Delta\phi$  values as reflected in the growing green fraction in the color encoded matrices.

Figure 3.6 shows frequency and phase estimation errors averaged over all induced  $\Delta f$  and  $\Delta\phi$  errors and repetitions at different levels of SNR obtained for both correction methods. Difference optimization outperformed spectral registration at all SNR levels and showed, in particular, distinctly lower  $\Delta\phi$  errors than spectral registration. Moreover, it also showed a slight increase for both estimated  $\Delta f$  and  $\Delta\phi$  errors with decreasing SNR but demonstrated still good performance at the lowest investigated SNR level of 30. Spectral registration showed an increase of estimated  $\Delta f$  errors with decreasing SNR, whereas mean values of estimated  $\Delta\phi$  errors remained nearly unaffected by SNR levels down to 70. Both mean  $\Delta f$  and  $\Delta\phi$  estimation errors obtained with spectral registration showed a strong increase for SNR levels of 50 and 30.

### 3.2.2 *In vivo* application

#### Evaluating the performance of difference optimization *in vivo*

To apply difference optimization to *in vivo* data,  $^1\text{H}$  MEGA-PRESS spectra were acquired in the posterior cortex ( $V = 13.1$  ml, see Fig. 3.7, measurement parameters can be found in the appendix in Tab. A.1:1, A.1:2 and A.3:1) of 47 healthy volunteers ( $54.8 \pm 6.4$  years), who provided written informed consent with the approval of the local ethics committee.

Single-shot NED and ED spectra were processed separately as described in section 3.1 by applying zero-filling, frequency correction, water peak extraction and phase correction between single NED and ED scans. To demonstrate the necessity of phase and frequency alignment between mean NED and ED spectra prior to subtraction and to assess the performance of the developed difference optimization method, the following four strategies were investigated: (a) no correction, (b) difference optimization, (c) spectral registration, and (d) manual correction. For method (a) no further data processing was performed. Method (b) used the automatic relative phase and frequency correction of the mean NED and ED spectra as described before. For method (c) spectral registration was applied to align mean NED and ED spectra. Method (d) applied relative phase and frequency correction manually with visual assessment based

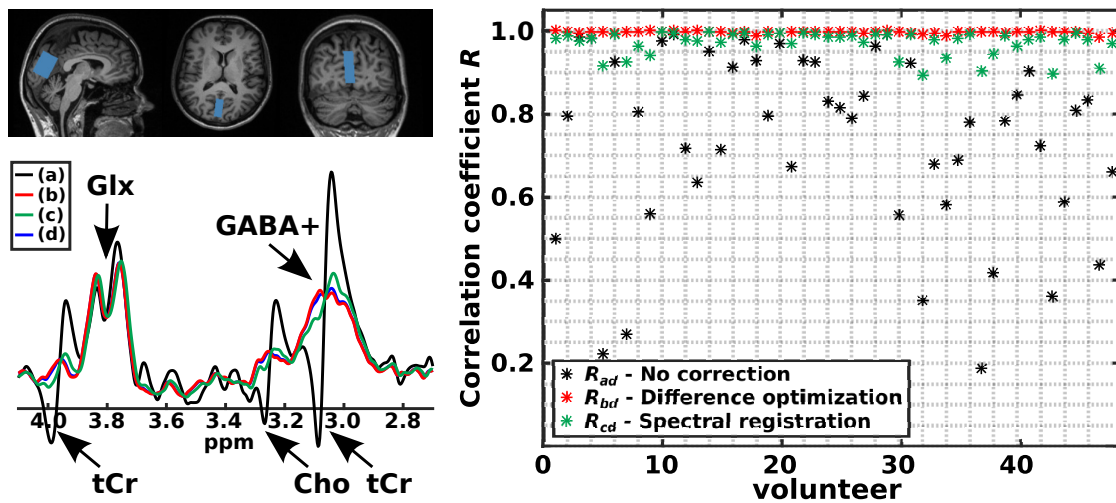


Figure 3.7: *Left top*: Voxel position in the posterior cortex ( $V = (25 \times 35 \times 12) \text{ mm}^3$ ). *Left bottom*: Example *in vivo* DIFF spectrum obtained by applying (a) no relative correction between NED and ED spectra (black), (b) difference optimization (red), (c) spectral registration (green) and (d) manual correction (blue). *Right*: Correlation coefficients  $R_{ad}$  (method (a) vs. (d)),  $R_{bd}$  (method (b) vs. (d)) and  $R_{cd}$  (method (c) vs. (d)) calculated between the real part frequency DIFF spectra in the range between 2.5 and 4.4 ppm for 47 subjects.

on criteria such as minimized subtraction artifacts in the real part of the frequency DIFF spectrum arising from Cho (at 3.2 ppm) and tCr (at 3.0 and 3.9 ppm) (see Fig. 3.7).

Since the true frequency and phase errors are unknown for *in vivo* data, method (d) was used as the gold standard reference spectrum. The gold standard DIFF spectrum of each dataset and the DIFF spectra obtained with method (a), method (b) or method (c) were compared in terms of Pearson correlation coefficients  $R_{ad}$ ,  $R_{bd}$  and  $R_{cd}$ , which were calculated between the corresponding real part mean DIFF spectra ( $R_{ad}$ : method (a) *vs.* method (d);  $R_{bd}$ : method (b) *vs.* method (d);  $R_{cd}$ : method (c) *vs.* method (d)) in the spectral range between 2.5 and 4.4 ppm. To reduce the impact of noise on the calculated correlation coefficients, the mean DIFF spectra were apodized by using a 10 Hz exponential damping function, respectively.

## Results

*In vivo* data measured in the posterior cortex revealed good spectra quality with an average SNR of  $87.9 \pm 13.6$  and FWHM of  $0.042 \pm 0.004$  ppm ( $5.2 \pm 0.5$  Hz) with respect to the NAA peak. To visualize the 2D minimization problem, Figure 3.8 illustrates the sum of the magnitude of an *in vivo* DIFF spectrum calculated for a range of discrete frequency and phase shifts,  $\Delta f$  and  $\Delta\phi$ . Real part DIFF spectra *in vivo* are displayed in Figure 3.7, which were obtained by processing the corresponding mean NED and ED spectra in the described four different ways: (a) no correction (black line), (b) difference optimization (red line), (c) spectral registration (green line) and (d) manual correction (blue line). Similar to the simulated dataset (see Fig. 3.5), the subtraction artifacts of tCr and Cho are clearly visible in the uncorrected DIFF spectrum (method (a)). Results after applying both automatic correction methods (b)

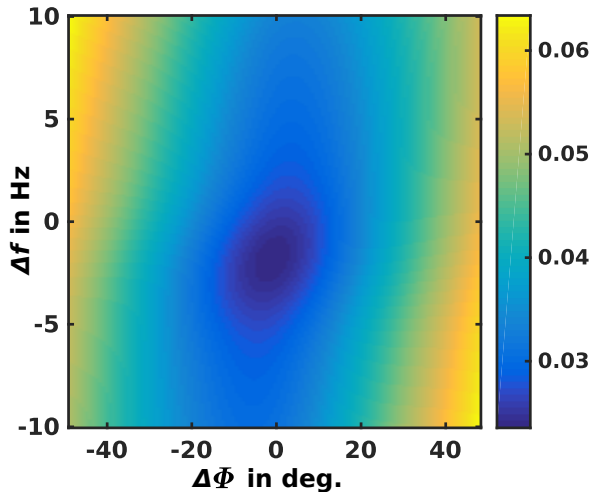


Figure 3.8: Exemplary depiction of the sum of the magnitude difference spectrum ( $sum_{DIFF}(\Delta f, \Delta\phi)$ , see Eq. 3.8) for a discrete range of frequency and phase shifts showing a minimum at  $\Delta f = -2.0$  Hz and  $\Delta\phi = -1.2$  deg.

and (c) showed distinct improvements, comparable with the manual correction (method (d)). Small subtraction artifacts from creatine and choline, however, remained in the DIFF spectrum processed with spectral registration (method (c)). The improved spectra quality is also reflected in the mean correlation coefficient of  $R_{bd} = 0.997 \pm 0.003$  compared to  $R_{ad} = 0.764 \pm 0.220$  (method (a), no corrections) calculated over all datasets (Fig. 3.7). Spectral registration revealed a slightly lower correlation coefficient of  $R_{cd} = 0.972 \pm 0.028$  compared to  $R_{bd}$ .

### 3.2.3 Discussion

The algorithm difference optimization was developed to align robustly mean NED and ED  $^1\text{H}$  MEGA-PRESS spectra. Comparing the difference optimization method with the common spectral registration approach included in the FID-A toolbox revealed superior performance of the former for all levels of SNR (see Fig. 3.6). Applying difference optimization to *in vivo* data resulted in nearly identical results regarding the final mean DIFF spectra when compared to manual correction as reflected in the high correlation coefficients. Spectral registration also improved spectra quality distinctly, but still showed small remaining residual subtraction artifacts in the final DIFF spectrum. In contrast and expectedly, not accounting for phase and frequency differences between NED and ED spectra at all resulted in large subtraction artifacts demonstrating the inevitable need of correction. However, it should be noted that taking the manually corrected spectra as gold-standard reference is somewhat limited because true phase and frequency differences between NED and ED spectra cannot be identified *in vivo*. Nevertheless, the findings observed *in vivo* confirm the main result obtained from the simulations of known true errors.

Performance of difference optimization and spectral registration dropped with decreasing SNR of the simulated spectra. However, spectral registration was inferior at low SNR levels as reflected in the more strongly increased means of the estimation errors for SNR lower than 50, compared to difference optimization that revealed only a comparably slight increase of the estimation errors,  $\Delta f$  and  $\Delta\phi$ , down to the lowest simulated SNR of 30. Moreover, difference optimization revealed distinctly lower mean estimation errors and standard deviations for  $\Delta\phi$  compared to spectral registration. The superior performance of difference optimization can be ascribed to the different minimization criteria used in the two compared routines. Spectral registration fits mean ED to mean NED spectra by using a nonlinear least squares regression algorithm while adjusting phase and frequency. In contrast, difference optimization minimizes the sum of the absolute differences ( $L^1$  norm) between ED and NED. The latter proved to be more sensitive to small differences (e.g. arising from subtraction artifacts), which are

less weighted in the least square regression analysis. This is underlined by the finding that the performance of the nonlinear least squares regression (spectral registration) was more affected by smaller SNR levels than difference optimization. Nevertheless, as demonstrated by Near et al., spectral registration performs excellent when applied to single-shot correction of consecutive scans with the same spectral fingerprint (Near et al., 2015).

Finally, some limitations have to be discussed. First, difference optimization requires fully water suppressed data or the subsequent removal of remaining water resonances in case of reduced water suppression. Since shape and amplitude of the residual water peak may vary as scanner drift causes frequency shifts of the water suppression pulse (Mullins et al., 2014; Near et al., 2015), subtraction of NED and ED spectra containing non-equivalent water resonances can lead to strong water subtraction artifacts that not necessarily vanish even with correct relative phase and frequency alignment of both spectra. Because difference optimization is based on minimizing subtraction artifacts, the routine will fail when aiming to minimize the dominating water subtraction artifact. However, the same issue holds for spectral registration (Near et al., 2015). Restriction of the analyzed input data range might be beneficial in cases, in which sufficient removal of unstable resonances cannot be achieved (Near et al., 2015). Nevertheless, the investigated spectral range should ideally cover frequencies of potentially arising subtraction artifacts in order to properly suppress their contributions by the algorithm. In addition, any signal contaminations from adjacent tissue (e.g. lipids), which may vary during the MRS acquisition due to measurement instabilities, should be avoided in advance, e.g. by applying localized outer volume suppression slabs.

Furthermore, like with all other MRS frequency and phase correction routines, the method requires sufficient SNR. For reliable correction of phase and frequency errors, the presented data suggest a minimum SNR level of around 70 for the mean NED and ED spectra, which is commonly achieved with J-edited GABA spectroscopy. Additionally, aiming to correct subtraction artifacts, the noise level should be sufficiently low to keep the amplitude of interfering unwanted signals distinguishable from noise. As a final remark, the proposed method does not substitute frequency and phase corrections of single consecutive NED and ED scans, which is mandatory before applying difference optimization to the corresponding mean spectra, but represents a tool to optimize mean DIFF spectra.

In summary, difference optimization is a robust and fast method for spectral alignment of NED and ED  $^1\text{H}$  MEGA-PRESS spectra, which is important for reliable GABA quantitation. One main advantage of the developed routine is that the correction can be performed by using the whole frequency spectrum without limiting the input data

range. Due to its simplicity and ease of implementation, difference optimization allows fast data processing without user-dependent intervention and a more accurate and consistent determination of the metabolite of interest. The presented routine might be also applicable for further editing approaches, such as for detecting e.g. lactate (Star-Lack et al., 1998), glutathione (Terpstra et al., 2005), 2-hydroxyglutarate (Choi et al., 2012) or NAAG (Edden et al., 2007).

# Chapter 4

## Systematic phantom experiments

This chapter describes the results of two preparatory phantom studies to characterize the metabolite signals measured with  $^1\text{H}$  MEGA-PRESS. In the first study, the Glx signal quantified from the DIFF spectrum was analyzed to explore the contributing amounts of Glu and Gln, respectively, which is of major importance regarding reliable interpretation of the observed metabolite measures. Additionally, it was investigated if signals of Glu and Gln can intendedly be separated by appropriate adjustment of the frequency selective editing pulse position when using MEGA-PRESS. In the second phantom study, the minimal detectable concentration differences of both metabolites were explored under *in vitro* and simulated *in vivo* conditions since the ultimate scope of this thesis was to investigate stimulus-induced changes of GABA and Glu in the human brain.

### 4.1 About the composition of Glx in the $^1\text{H}$ MEGA-PRESS difference spectrum

When applying  $^1\text{H}$  MEGA-PRESS to quantify GABA, also Glx, the composite measure of Glu and Gln, can be quantified at 3.75 ppm from the resulting DIFF spectrum due to co-editing during the ED scan. As already introduced in Chapter 2.3.1, Glu and Gln are differently involved in the physiological processes in the human brain. Glu is the main excitatory neurotransmitter but also participates in the metabolism (TCA cycle). In contrast, Gln is related to GABA synthesis but also represents an intermediate product from glutamatergic neurotransmission and is closely linked to the Glu-Gln cycling. Therefore, to interpret Glx signal levels correctly, it is important to know about the contributing amounts of Glu and Gln, respectively.

Recently, contradictory claims about the composition of the Glx signal in the MEGA-

PRESS DIFF spectrum were made. Shungu et al. (Shungu et al., 2013) stated that the Glx signal measured with MEGA-PRESS mainly consists of Glu. The authors justified their claim by first, determining Glx using MEGA-PRESS, and second, quantifying pure Glu and Glx by applying a constant time PRESS sequence (CT-PRESS) (Mayer and Spielman, 2005) that exploits effective homonuclear decoupling. CT-PRESS is very similar to 2D J-resolved spectroscopy and applies, besides the conventional PRESS sequence module for voxel localization, an additional refocusing pulse whose position is shifted with each encoding step while the time interval between excitation and begin of the data acquisition is held constant. Thus, the line splitting of the metabolite resonance of interest is suppressed in the corresponding 1D diagonal spectrum, and, in case of Glu, the isolated  $^4\text{CH}_2$ -resonance at 2.3 ppm can be quantified. Since the Glu and Glx measures obtained from applying both MRS approaches were correlated significantly, the authors concluded that the Glx signal quantified at 3.75 ppm from the MEGA-PRESS spectrum predominantly consists of Glu. In contrast, a recent MEGA-PRESS phantom study performed by Veenendaal et al. (Veenendaal et al., 2016) demonstrated that a substantial fraction of Gln is contained in the Glx signal quantified from the DIFF spectrum by measuring phantoms of different Glu and Gln concentrations. The Glx signal quantified at 3.75 ppm showed strong correlation with the nominal adjusted concentrations of Glu and Gln, respectively. Veenendaal et al. made a rough estimate of Gln contributing to one third to the *in vivo* Glx resonance measured with MEGA-PRESS, which was concluded from the comparable goodness of the correlations between nominal concentrations and quantified signals.

In the following section, the contradictory results about the composition of Glx when measured with MEGA-PRESS was investigated by performing a phantom study on Glu and Gln phantoms to explore whether frequency selective editing at 1.9 ppm results in signals contributions of Glu and Gln at 3.75 ppm in the MEGA-PRESS difference spectrum. Moreover, since the common  $^1\text{H}$  MEGA-PRESS sequence is optimized to detect GABA by applying the frequency selective pulse at 1.9 ppm, it was investigated whether the detection of both, either Glu or Gln, can be optimized by varying the frequency position of the editing pulse.

#### 4.1.1 Glutamate and glutamine phantom measurements

The Glx signal at 3.75 ppm was investigated by performing MEGA-PRESS measurements with separate Glu and Gln phantoms, respectively. Two phantoms of 250 ml each were prepared consisting of a commonly used stock solution containing 72 mmol/l  $\text{K}_2\text{HPO}_4$ , 28 mmol/l  $\text{KH}_2\text{PO}_4$  and 1 g/l  $\text{NaN}_3$ , and 40 mmol/l Glu or Gln. Moreover, 40 mmol/l GABA was added as frequency reference and a pH value of 7 was adjusted.



A PRESS spectrum was acquired first (see Tab. A.1:3) to determine the proper frequency positions of the frequency selective editing pulse to be applied during MEGA-PRESS for appropriate editing of the phantom compounds. The frequency selective editing pulse is applied by default relative to the water resonance position that depends on temperature due to alterations of electron shielding and hydrogen bonding equilibrium (Hindman, 1966). The water signal resonates at 4.7 ppm at 37°C *in vivo* but shows a shift of 0.01 ppm/1°C. Thus, the editing pulse position has to be shifted along the ppm axis for editing at the corresponding frequency at other temperatures. To determine the relative frequency shift, the center peak of the isolated GABA resonance at 3 ppm was used as reference. For both phantoms, measurement series (see Tab. A.1:4 and A.1:5) were acquired at room temperature while varying the editing pulse position between 1.7 and 2.5 ppm in steps of 0.05 ppm, resulting in 17 editing pulse positions. Each acquisition was repeated ten times.

To answer the question which amount of Glu and Gln is contained in the corresponding DIFF spectrum, the editing efficiency  $\alpha_{met}$  (with *met* given by Glu or Gln) was defined as the intensity of the metabolite signal at 3.75 ppm in the DIFF spectrum ( $I_{met}^{DIFF}$ ) normalized to the corresponding signal intensity in the NED spectrum ( $I_{met}^{NED}$ ), since the latter represents the nominal concentration and its signal intensity is not expected to change with the editing pulse position (Fig. 4.1 A):

$$\alpha_{met} = \frac{I_{met}^{DIFF}}{I_{met}^{NED}} \quad (4.1)$$

The dependence of mean  $\alpha_{met}$  on editing pulse frequency position is depicted in Figure 4.1 B. First of all, because  $\alpha_{Gln}$  was not zero or revealed only low values compared to  $\alpha_{Glu}$  it can be concluded that Gln indeed contributes to the Glx signal in a DIFF spectrum. For conventional GABA editing at 1.9 ppm, as applied in most *in vivo* studies, mean  $\alpha_{Glu}$  and mean  $\alpha_{Gln}$  resulted in comparable values of 0.51 and 0.55, respectively. Assuming a ratio of 2:1 between absolute concentrations of Glu and Gln (Govindaraju et al., 2000; Rae, 2014) (see also Chapter 2.3.1) in healthy brain state *in vivo* it follows that for conventional GABA <sup>1</sup>H MEGA-PRESS spectroscopy the Glx resonance at 3.75 ppm is composed to two thirds of Glu and to one third of Gln and mirrors the initial concentration ratio of both metabolites in the brain. This inference confirms the rough estimation by Veendendal et al. However, absolute values for the Glu and Gln fractions *in vivo* cannot be given based on single subject measurements, since the concentration ratio between both metabolites is only approximate. To this end, isolated measurements of Glu and Gln are required.

Separate measurements of Glu and Gln by using MEGA-PRESS can only be achieved

if the editing efficiencies of Glu and Gln are sufficiently different with respect to the editing pulse position. From Figure 4.1 B it can be seen that this is not the case, since the curve shapes of  $\alpha_{Glu}$  and  $\alpha_{Gln}$  are highly similar with maximum editing efficiency in the range between 2.2 ppm and 2.3 ppm. Thus, deliberately measuring Glu or Gln only or introducing different resulting Glu to Gln ratios by appropriate adjustment of the frequency selective editing pulse position is not possible. The inability to differentiate between Glu and Gln can be explained by their similar chemical structures (see Fig. 2.10). Since both metabolites contain two methylene groups ( $\text{CH}_2$ ) and a single methine group ( $\text{CH}$ ), the coupling constants and chemical shifts are therefore also similar. The methine groups resonate at 3.75 ppm for Glu and at 3.76 ppm for Gln and their coupled multiplet resonances of the  $^3\text{CH}_2$  group between 2.0 and 2.1 ppm (de Graaf, 2007), respectively, being similarly affected by the frequency selective editing pulse during the ED acquisition.

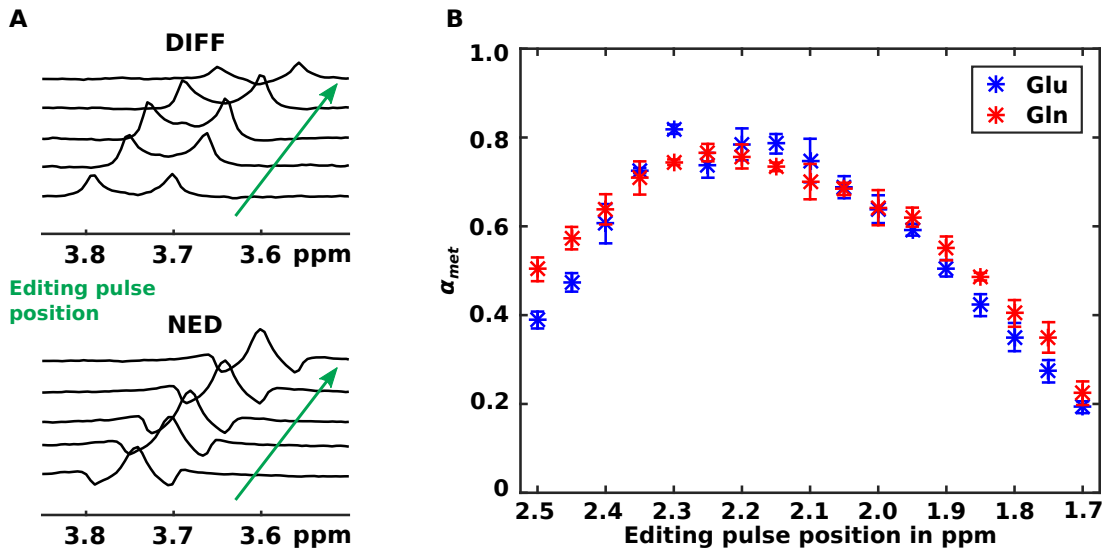


Figure 4.1: (A) Glutamate signal at 3.75 ppm in the DIFF and NED spectrum acquired with varying editing pulse position. The signal intensity in the DIFF spectrum reveals a maximum for resonant frequency selective editing, whereas the signal appearance in the NED spectrum remains unaffected. (B) Editing efficiency  $\alpha_{met}$  for Glu and Gln in dependence on the frequency selective editing pulse position. For both metabolites maximum editing efficiency is achieved for editing between 2.2 ppm and 2.3 ppm.

#### 4.1.2 Conclusions and alternative approaches

As explored in section 4.1.1, when applying the MEGA-PRESS spectroscopy, the Glx signal quantified at 3.75 ppm represents approximately the actual concentration ratio between Glu and Gln, which are edited in a similar way. This finding supports the

results of Veenendaal et al. (2016) and contrasts the previous assumption by Shungu et al. who stated that the Glx signal in the MEGA-PRESS difference spectrum constitutes mainly Glu. When quantifying pure Glu, the only allocation to neurotransmission seems arguable (Rae, 2014), because as previously described Glu is also involved in energy metabolism. Moreover, when measuring Glx the content-wise reasoning gets even more obscure since Gln is linked to both, neurotransmission and metabolism. Thus, to give a brief statement on what we are actually measuring when either quantifying Glu or Glx is not possible. Nevertheless, it can be hypothesized, that when measuring Glu separately it is more likely to mirror excitatory neurotransmission than when quantifying Glx. Quantifying Glx supposedly increases the amount of information about metabolism. Moreover, measuring Glx does not allow for the evaluation of conditions, where the concentrations of Gln and Glu are in opposing directions.

A widely used method to retrospectively disentangle overlapping signals is the usage of appropriate quantitation software. The quantitation toolbox LCModel (Provencher, 2001) proved to reliably estimate metabolite concentrations (O’Gorman et al., 2011) of *in vivo* MR spectra by fitting a linear combination of *in vitro* spectra from metabolite solutions in the frequency domain. To this end, LCModel requires sequence specific basis sets that either have to be precisely acquired for each metabolite under defined conditions or have to be simulated while using exact timing parameters of the applied MR sequence that are often not available. Although LCModel is widely accepted as a default toolbox to quantify MR signals, improper use has led to erroneous fitting in multiple literature examples (Mullins et al., 2014). In particular, over- or underestimation of single components of overlapping resonances, such as Gln and Glu, has been claimed (Shungu et al., 2013) and is usually depicted in higher estimation errors for Gln (Henry et al., 2011; O’Gorman et al., 2011). Moreover, user-intervention is limited that, on the one hand, is definitively advantageous to prevent errors caused by inexperienced users but, on the other hand, also has the disadvantage to limit the optimization of misfitted spectra. Thus, the usage of LCModel requires caution and fitting of isolated resonances should be preferred even if it results in reporting composite measures, such as Glx, in some cases.

Nevertheless, some alternative MRS approaches allowing the isolated detection of Glu at a clinical field strength of 3 T or lower shall be mentioned finally. At first, Glu quantitation can be distinctly improved by optimizing the echo time in a PRESS sequence and appropriate TE of 40 ms and 80 ms have been reported at 3 T (Mullins et al., 2008; Schubert et al., 2004). Moreover, TE-averaged PRESS proved to allow for reliable Glu quantitation by acquiring multiple 1D PRESS spectra at variable TE. This technique exploits the fact that the appearance coupled resonances depends on

TE, e.g. the outer peaks of triplets evolve with opposite phases during TE, whereas the center peak is not affected (see Chapter 2.2.3). Thus, by averaging scans acquired over multiple TE, the spectrum is substantially simplified (Harris et al., 2017) since the outer peaks are cancelled out and the center peak remains in the averaged spectrum. This allows the resolution of a single resonance of Glu at 2.35 ppm. Furthermore, J-coupling can also be disentangled by performing 2D measurements by adding a second spectral dimension containing the coupling information. However, this approach is seldomly used in *in vivo* studies due to the necessary long measurement times. Although the briefly presented selection of MRS methods allows to measure pure Glu, GABA cannot be resolved from the corresponding spectra or only with long measurement times (2D techniques), which is unsuitable for *in vivo* measurements at 3 T.

## 4.2 Measurable concentration differences of GABA and Glx

An increasing number of studies has focused on the investigation of changes of metabolite concentrations *in vivo* during the performance of an external task or while applying a stimulus to volunteers (Bednařík et al., 2015; Gussew et al., 2010; Kühn et al., 2016; Kupers et al., 2009; Mangia et al., 2007; Mullins et al., 2005). However, to successfully detect any concentration differences is primarily limited by the size of the effect itself, and in turn to the experiment conditions. The latter comprises of, first, the experiment conditions that can be influenced by the experimentalist to some extent, such as data quality and number of investigated subjects, and second, the experiment conditions that are of random nature and are related to instabilities or uncertainties of the measurement, such as performance of the applied method or impact of the used evaluation software of the acquired data. Since one main aim of this thesis was to investigate pain-induced concentration changes of GABA and Glu, their measurable concentration changes by using  $^1\text{H}$  MEGA-PRESS were investigated by acquiring a series of brain phantoms of varying GABA and Glu concentrations. Since instead of pure Glu the Glx signal is quantified from the MEGA-PRESS DIFF spectrum, as described in the previous chapter, the following phantom study consequently reports Glx changes. Moreover, the impact of the number of analyzed data samples and data quality, in terms of linewidth and SNR, under *in vitro* and under simulated *in vivo* conditions on the detectable concentration changes of GABA and Glx was explored.

## 4.2.1 Experiment setup

A brain phantom stock solution was prepared as described in section 4.1.1 and the following brain metabolites were added in concentrations mimicking approximately *in vivo* conditions: NAA (50 mmol/l), Cr (40 mmol/l), mI (30 mmol/l) and Gln (15 mmol/l). From this solution eleven phantoms of 250 ml each were made with increasing concentrations of GABA ranging from 10 mmol/l to 13 mmol/l and decreasing concentrations of Glu in the range between 45 mmol/l and 31.5 mmol/l in equidistant steps (Fig. 4.2), resulting in overall concentration changes of +30 % and -30 %, respectively. Each phantom was adjusted to a pH value of 7 and stored in the MR scanner room overnight to allow for temperature stabilization.

The measurements were conducted on the following day, and phantoms were measured consecutively but in randomized order independent of the adjusted GABA and Glu concentrations. First, a PRESS spectrum was acquired (see Tab. A.1:6) to determine the appropriate frequency position of the frequency selective editing pulse at room temperature (see section 4.1.1). Since the exact position of the edited GABA resonance relative to the water signal cannot be directly observed due to overlapping by other signals, the NAA resonance frequency extracted from the PRESS scan was used as reference (Corbett et al., 1995), which commonly resonates at 2.0 ppm with a relative chemical shift of 0.1 ppm to the GABA resonance (at 1.9 ppm). Subsequently, the prepared phantoms were measured with 20 repetitions each by using  $^1\text{H}$  MEGA-PRESS (see Tab. A.1:7 and A.1:8).

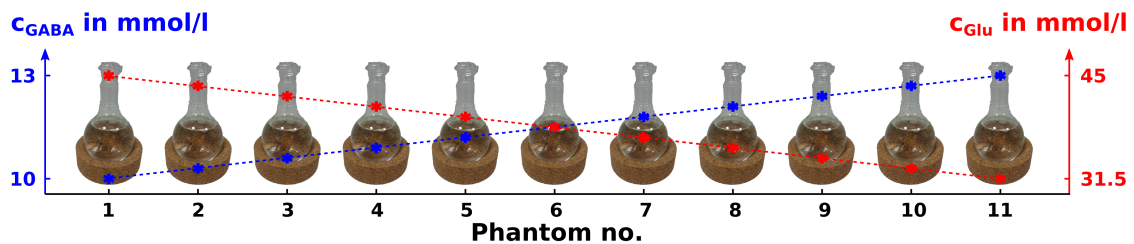


Figure 4.2: Experiment setup of eleven brain phantoms with increasing GABA concentrations in the range between 10 mmol/l to 13 mmol/l (blue) and decreasing Glu concentrations ranging from 45 mmol/l to 31.5 mmol/l (red).

## 4.2.2 Detectable concentration changes *in vitro*

The acquired data revealed good spectra quality with SNR of  $1192 \pm 67$  and FWHM =  $0.0133 \pm 0.0005$  ppm ( $1.6 \pm 0.1$  Hz) with respect to the NAA peak. From the calculated DIFF spectra GABA and Glx were quantified at 3.0 ppm and 3.75 ppm, respectively.

Creatine was used as internal reference to account for differences between single measurements since its adjusted concentration was constant for all phantoms. With tCr quantified at 3.0 ppm from the NED spectra, the corresponding concentration ratios GABA/tCr and Glx/tCr were calculated for each repeated measurement and phantom. The *in vitro* concentrations of GABA/tCr and Glx/tCr for the different phantoms are depicted in Figure 4.3 A. Low variation coefficients over the repeated measurements of  $1.5 \pm 0.4\%$  for GABA/tCr and  $0.9 \pm 0.2\%$  for Glx/tCr were obtained. Moreover, an increase of the GABA/tCr mean values and decreasing mean values for Glx/tCr in distinct steps was observed. The measured concentration change between phantom number one and eleven was  $+24.8\%$  for GABA and  $-23.4\%$  for Glx, which was lower than the nominally adjusted concentration difference of  $\pm 30\%$ . However, in case of Glx, this deviation is not surprising because the composite measure of Glu and Gln was quantified. Therefore, as described in section 4.1, the Glx signal reflects the concentration ratio between Glu and Gln, whereas only the concentration of Glu was varied. Thus, the expected percentage concentration change of Glx can be calculated from the known concentrations  $c_{Glu}$  of phantom #1 and phantom #11, and  $c_{Gln}$ , which was constant for all phantoms, as follows:

$$\Delta \text{Glx}_{1-11} = 100 \cdot \left( \frac{c_{Glu_{11}} - c_{Glu_1}}{c_{Gln} + c_{Glu_1}} \right) \quad (4.2)$$

Hence,  $\Delta \text{Glx}$  results to  $-22.5\%$  and is in good accordance with the observed value determined from the phantom measurements. The lower concentration difference for GABA of  $+24.8\%$  have presumably to be ascribed to aberrantly adjusted GABA concentrations for phantom #1 and phantom #11, whose solutions were used to generate the further nine phantoms of intermediate GABA and Glu concentrations.

Phantom #2 was an outlier for both GABA and Glx with an almost similar mean GABA/tCr ratio as phantom #1 and a distinctly lower mean Glx/tCr ratio compared to both neighboring phantoms #1 and #3. Phantom #6 and phantom #7 also showed deviations of the mean value from the equidistant concentration steps compared to the adjacent phantoms for GABA/tCr and Glx/tCr, respectively. Such variations of detected mean concentrations may be caused due to different factors. First, during the preparation process of the phantoms slight differences between the nominal and the truly obtained GABA and Glu concentrations might have occurred because adjustment of small concentration differences is particularly sensitive to errors. Second, the prepared solutions only have a limited durability. Third, as the chemical shift of metabolites is known to depend on temperature and pH value (Govindaraju et al., 2000), small differences of the pH values between the phantoms cannot be excluded since they were

adjusted individually. Thus, with the frequency selective editing pulse potentially not exactly applied at 1.9 ppm for all phantoms, differing editing efficiencies of GABA and Glx between the measurements may have resulted leading to aberrantly measured GABA/tCr and Glx/tCr concentration ratios.

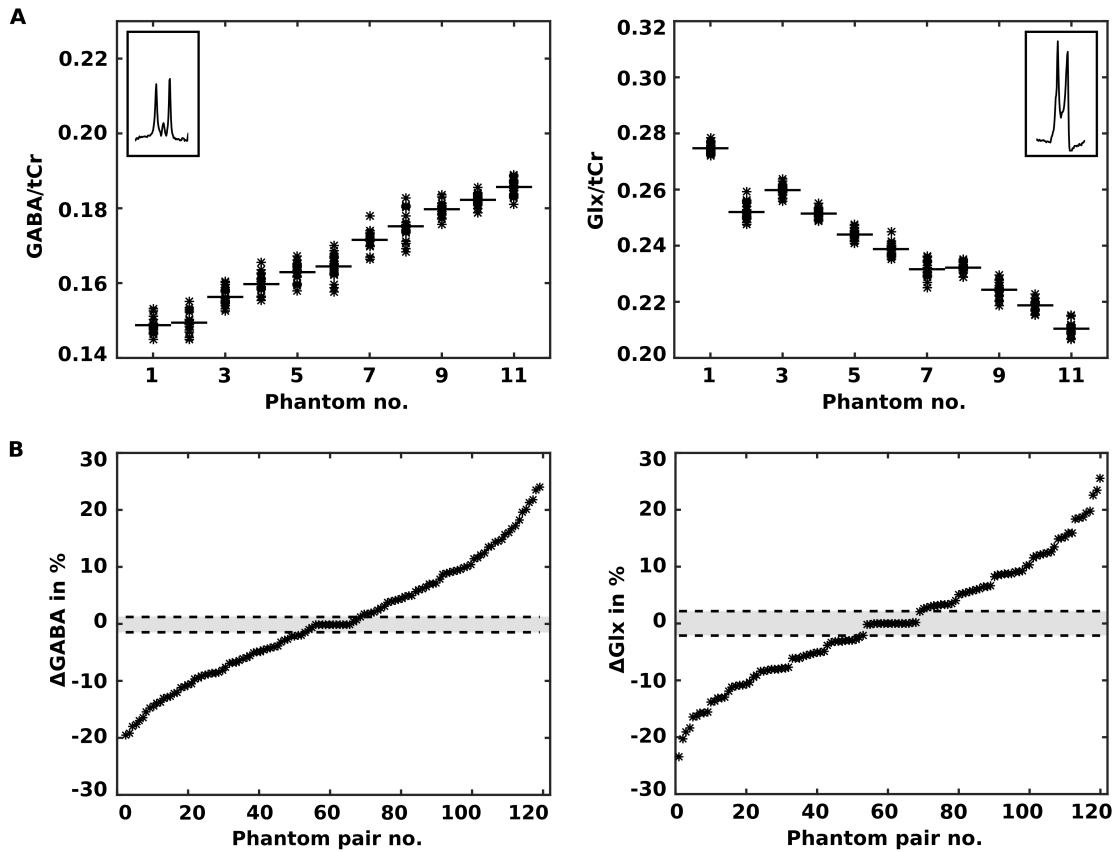


Figure 4.3: (A) Concentration courses for GABA/tCr and Glx/tCr obtained from phantom measurements of 20 repetitions (\*) with varying GABA and Glu concentrations. Mean values are represented by solid lines and exemplary GABA and Glx *in vitro* signals are depicted. (B) Relative percentage changes  $\Delta$ GABA and  $\Delta$ Glx calculated from the mean values of the compared distributions of each phantom pair considering all 20 repetitions. The gray shaded areas constitute the concentration differences that cannot be identified. The dashed lines (- -) correspond to the detection thresholds of metabolite concentration changes that were determined by applying a two-sided t-test with  $\alpha = 0.05$  to each phantom pair combination.

However, the observed deviations of the mean values of GABA/tCr and Glx/tCr from the nominal adjusted equidistant concentration steps do not restrict the further statistical analysis, because measurable concentration differences or changes are essentially limited by the distribution of the data around the mean value, which, in turn, is related to the experiment conditions as described at the beginning of this chapter. Moreover, the magnitude of the observed concentration ratio dispersion is independent from possible

erroneous initial metabolite concentrations or differing editing efficiencies since these parameters were stable over the repeated measurements in each phantom.

A range of possible concentration differences was created by comparing the distributions of each combination of possible phantom pairs (11 · 11 combinations). The statistical analysis was conducted by applying a two-sided t-test ( $\alpha = 0.05$ ) to each phantom pair combination and the corresponding distributions of GABA/tCr and Glx/tCr, respectively. It should be noted that no correction for multiple comparisons is required in this case since the determination of detectable concentration differences should be independent from the number of comparisons or phantoms. Finally, the relative percentage changes,  $\Delta$ GABA and  $\Delta$ Glx, were calculated from the mean values of the compared distributions of each phantom pair (see Fig. 4.3 B). The statistical analysis was repeated while reducing the number of considered data points to 15 and 10 to explore possible influences on the statistical outcome.

The obtained absolute detection thresholds for concentration changes of GABA and Glx are listed in Table 4.1. For both,  $\Delta$ GABA and  $\Delta$ Glx, even small absolute concentration differences of 1.4 % and 2.1 % were identified. The higher detection threshold for  $\Delta$ Glx is related to the compared available phantom pairs showing a gap below  $\Delta$ Glx of 2.1 % (see Fig. 4.3 B). The actual detection threshold for  $\Delta$ Glx is presumably lower than for  $\Delta$ GABA due to the lower variation coefficients for Glx/tCr of the repeated measurements. Moreover, the detection threshold of concentration differences was not affected by a reduction of included data points due to the narrow data distribution for each phantom.

### 4.2.3 Detectable concentration changes under simulated *in vivo* conditions

To simulate *in vivo* conditions the acquired *in vitro* data were line broadened to 0.05 ppm (6.2 Hz), and normally distributed noise was added to reduce the SNR to 90 with respect to the NAA resonance. GABA/tCr and Glx/tCr were determined analogously to the processing of the *in vitro* data and the statistical analysis was done in the same manner. The distributions of GABA/tCr and Glx/tCr are depicted in Figure 4.4 A. The dispersions of both metabolite ratios were distinctly increased compared to the *in vitro* results, which is also reflected in the increased variation coefficients of  $6.4 \pm 1.4$  % for GABA/tCr and  $3.7 \pm 0.7$  % for Glx/tCr. Notably, compared to the *in vitro* data, the quantified GABA and Glx values revealed a positive offset, thus being overestimated compared to the original (*in vitro*) data. Moreover, a concentration difference between phantoms #1 and #11 of +17.6 % for GABA and  $-23.9$  % for Glx was observed. The latter is in good accordance with the result obtained from the *in vitro* measurement,



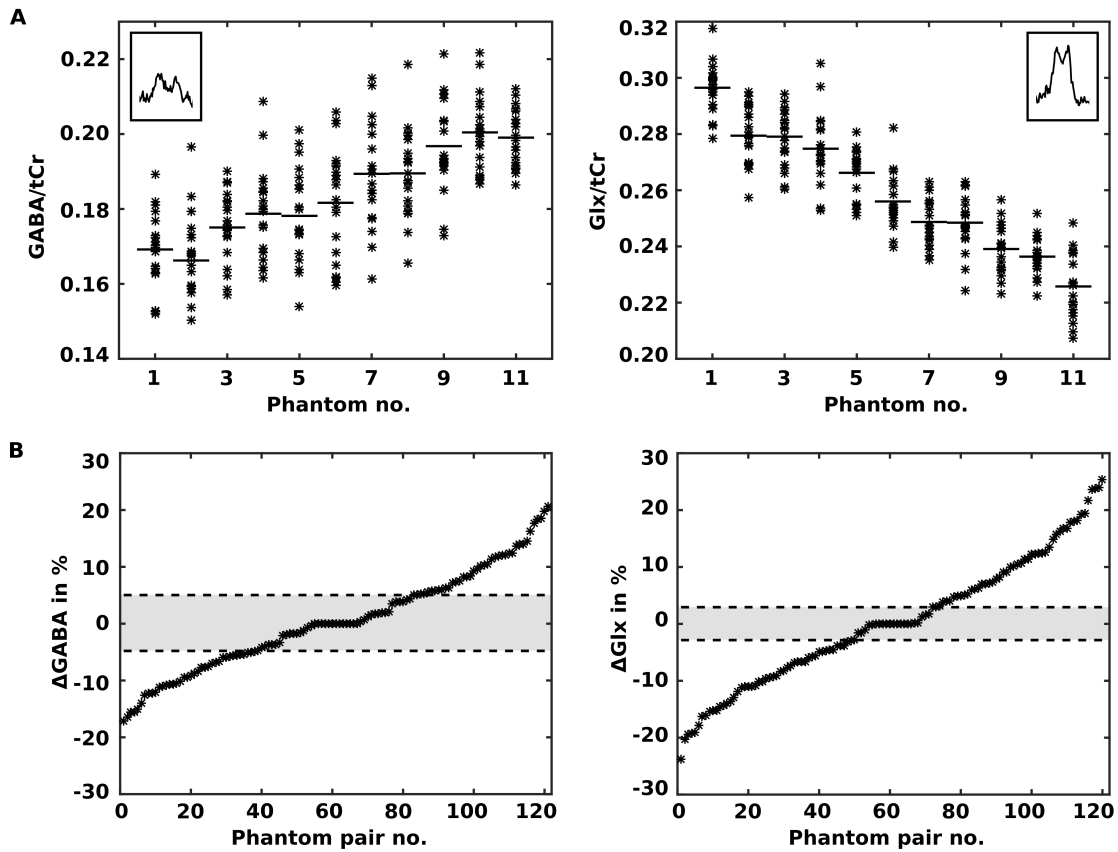


Figure 4.4: (A) Concentration courses for GABA/tCr and Glx/tCr under simulated *in vivo* conditions obtained from the measured phantom series (section 4.2.2). Mean values are represented by solid lines and exemplary simulated GABA and Glx *in vivo* signals are depicted, respectively. (B) Relative percentage changes  $\Delta$ GABA and  $\Delta$ Glx calculated from the mean values of the compared distributions of each phantom pair considering all 20 repetitions. The gray shaded areas constitute the concentration differences that cannot be identified comprising a broader range compared to the *in vitro* conditions. The dashed lines (- -) correspond to the detection threshold of metabolite concentration changes that were determined by applying a two-sided t-test with  $\alpha = 0.05$  to each phantom pair combination.

whereas the percentage change of GABA is smaller compared to the previous result. Both, the increased distributions and the concentration offsets can be ascribed to the poorer data quality under simulated *in vivo* conditions. In particular in case of the latter, low concentration metabolite resonances tend to be overestimated with decreasing SNR and increasing FWHM (Henry et al., 2011; Kreis, 2004). The inferior data quality also hampered the identification of concentration differences between the phantom measurements. The detection thresholds for  $\Delta$ GABA and  $\Delta$ Glx increased to 4.9% and 2.9%, respectively, when including all data points from the 20 repeated measurements. In contrast to the *in vitro* data, reduction of the number of included datasets to 15 and

10 resulted in increased minimally detectable differences (see Fig. 4.4 B and Tab. 4.1) with GABA being more affected than Glx, which is possibly related to the comparably low concentration and the smaller signal amplitude of GABA at 3.0 ppm in the DIFF spectrum.

Sample size	<i>In vitro</i>		<i>In vivo</i>	
	$\Delta$ GABA in %	$\Delta$ Glx in %	$\Delta$ GABA in %	$\Delta$ Glx in %
20	1.4	2.1	4.9	2.9
15	1.3	2.1	5.5	3.1
10	1.4	2.1	7.3	3.7

Table 4.1: Detection thresholds of GABA and Glx concentration differences under *in vitro* and under simulated *in vivo* conditions for varying numbers of included data points.

#### 4.2.4 Conclusions and limitations

The results from the phantom study indicate that  $^1\text{H}$  MEGA-PRESS works fairly reliable under ideal (*in vitro*) conditions and allows to resolve small concentration differences of 1.4% for GABA and 2.1% for Glx. It can be assumed that the observed variation coefficients for GABA and Glx mainly reflect the effect of the limited performance of the experiment setup. Evaluating the acquired phantom spectra under simulated *in vivo* conditions demonstrated inferior metabolite quantitation due to decreased spectra quality as indicated by the increased detection thresholds for  $\Delta$ GABA and  $\Delta$ Glx.

When performing *in vivo* MRS measurements data quality is affected by several experimental parameters. As introduced in Chapter 2.1.3, SNR is proportional to the measured voxel volume and increases with the square root of the number of acquired scans. Thus, SNR can be improved by, first, choosing large voxel volumes. However, this leads to reduced spatial specificity due to increased partial volume effects. Second, improving SNR by acquiring an increased number of MR scans may suffer from possible frequency drifts over long measurement times (see Chapter 3), because the editing efficiency of GABA will be affected by drifts of the frequency selective editing pulse position (Craven et al., 2014). Moreover, narrow linewidths are essential for reliable metabolite quantitation and can be realized by appropriate shimming to reduce magnetic field inhomogeneities. However, achievable linewidths are affected not only by the available hardware (shim system) but also by the location of the volume of interest in the brain. Thus, magnetic field inhomogeneities in brain areas containing or being surrounded by pulsating blood vessels, bones or air can only be removed to a limited extent due to unavoidable motion and different magnetic susceptibilities as, e.g.,

in the prefrontal cortex, thalamus or brainstem. Typically, a minimal number of 128 MEGA-PRESS scans, NED and ED each, are acquired with a maximum measurement time on the order of 13 min with voxel sizes ranging from 8 ml to 27 ml.

The presented results also demonstrate that the detection of small metabolite concentration differences is improved with an increased number of investigated data samples. Investigating multiple subjects in *in vivo* MRS studies reduces the probability of incidental findings and improves statistical validity. However, sample sizes are naturally restricted by the available study time, the number of participating volunteers or patients, and last but not least by money. Thus, reported sample sizes in MRS studies range typically from 10 up to 30 and more, depending on the complexity of the study design and possible co-variates.

Finally, some limitations have to be discussed. The performed phantom study reports on repeated measurements of the same phantoms of varying GABA and Glx concentrations. Transferring the findings to *in vivo* fMRS studies, the reported detection thresholds are only applicable for repeated measurements within the same subject revealing the same degree of stimulus-induced concentration changes over all measurements. Since the aim of most research studies is to give generally valid statements that can not be made based on repeated measurements of the same single subject, multiple subjects are commonly investigated. However, same degree of stimulus-induced metabolite concentration changes cannot be assumed for all subjects due to inter-individual differences. Moreover, slightly differing resting state metabolite concentrations between subjects lead to an additional impact on the data sample distributions. The influence of the latter can be excluded for functional measurements that focus on intra-individual changes by analyzing relative instead of absolute metabolite concentration changes. Unfortunately, this approach is not applicable to comparisons between two subject groups, since data normalization requires the measurement of data pairs, and thus, complicates the identification of small group differences due to additional ambiguities. Nonetheless, inter-individual variations can be reduced by investigating preferably homogeneous subject groups considering, e.g. gender, age and handedness.

The reported detection thresholds for  $\Delta$ GABA and  $\Delta$ Glx cannot be directly transferred to *in vivo* studies and represent only an estimate of the potential power of functional MRS MEGA-PRESS measurements. Nevertheless, the relatively low thresholds under simulated *in vivo* conditions are promising that stimulus-induced GABA and Glx changes can be observed in *in vivo* experiments when exceeding a crucial amplitude.

# Chapter 5

## Functional MR spectroscopy during acute pain perception in the human brain

After having explored the potential of the  $^1\text{H}$  MEGA-PRESS sequence to determine concentration differences between GABA and Glx containing solutions, the technique was applied in a functional MRS study. As described in the following, a stimulation protocol was developed for time-resolved  $^1\text{H}$  MEGA-PRESS measurements to explore both excitatory and inhibitory neurotransmitter changes during pain perception in volunteers. Parts of this chapter have previously been published as an article (Cleve et al., 2015) and were presented at national (Cleve et al., 2014b) and international conferences (Cleve et al., 2013, 2014a).

### 5.1 Motivation

Recent  $^1\text{H}$  MRS studies in healthy subjects revealed changes in Glu concentration evoked by acute pain stimulation in different brain regions known to be activated during pain perception, such as the insular and anterior cingulate cortex (Gussew et al., 2010; Mullins et al., 2005). The purpose of the current study was to address the question whether  $^1\text{H}$  MEGA-PRESS MR spectroscopy in combination with acute pain stimuli is able to quantify pain-induced neurotransmitter changes of Glx and GABA in the human brain. The experiments were based on a recent previous study of time-resolved measurements of Glu changes in the insular cortex (Gussew et al., 2010) performed in the Medical Physics Group Jena and were now extended to investigate also the potential changes of the inhibitory neurotransmitter GABA. To this end, pain evoked neurochemical changes in the anterior cingulate cortex (ACC), a region well known

to be activated during pain perception (Peyron et al., 2000), were investigated. In addition, the occipital cortex (OC) was selected as control region.

## 5.2 Experiment setup

### 5.2.1 Volunteers and thermal stimulation unit

Twenty right-handed healthy female volunteers ( $24.0 \pm 1.6$  years) were recruited without any known brain disorder or other chronic disease including chronic pain or diseases requiring medication. Women were investigated because they are more sensitive to pain than men (Bartley and Fillingim, 2013; Berkley, 1997). The experiments were not performed during menstruation or other indisposition to avoid interfering effects on pain perception. Prior to the measurements volunteers gave written consent following the guidelines of the local ethics committee after having been fully informed about the experiments including all possible risks.



Figure 5.1: MR compatible thermode placed on the left forearm and control unit.

Painful heat stimuli were applied to the inside of the left forearm by using a MR compatible thermode<sup>1</sup> placed one hand's breadth above the wrist. The thermode consists of a 27 mm diameter peltier element that offers fast heating rates of up to  $70^\circ\text{C}/\text{s}$  and cooling rates of up to  $40^\circ\text{C}/\text{s}$  within a temperature range of  $30^\circ\text{C}$  to  $55^\circ\text{C}$ . The control unit of the thermode was placed outside the scanner room while delivering the thermal stimuli inside the fMRI scanners via the thermode.

Two regions of interest were investigated in this study: the anterior cingulate cortex (ACC,  $V = (36 \times 20 \times 12) \text{ mm}^3$ ) and the occipital cortex (OC,  $V = (35 \times 20 \times 15) \text{ mm}^3$ ), see Fig. 5.2. The MR measurements (see Tab. A.1:9 - A.1:16 and Tab. A.3:2) in ACC and OC were performed on different days with a gap of up to 2 months. Prior to each MR session the intensity of the applied heat stimuli was individually adjusted (maximum stimulation temperature of  $47^\circ\text{C}$ ) to consider inter-individual variations in pain perception by using the method of limits (Defrin et al., 2006; Fruhstorfer et al., 1976): The volunteers received four successive ramps of increasing temperature starting at  $32^\circ\text{C}$  in two runs. During the first run the volunteers

<sup>1</sup>Medoc PATHWAY system with CHEPS thermode, Ramat Yishay, Israel, <http://medoc-web.com/products/pathway/>

were asked to abort the increasing temperature ramp by pressing a button when the perceived temperature started to be painful, and during the second run when the temperature was not bearable anymore to provide the individually tolerable lower ( $T_{min}$ ) and upper ( $T_{max}$ ) thermal pain threshold. The stimulation temperature was then defined by subtracting 30% of the tolerable painful heat interval of the upper pain threshold ( $T_{max} - 0.3 \cdot (T_{max} - T_{min})$ ). During the test the subjects were left unattended in an isolated room to reduce external distractions. To monitor habituation effects volunteers were asked to rate the stimuli intensity prior to (during the pre-test) and after the experiment using a visual analogue pain scale (VAS (Von Korff et al., 2000)).

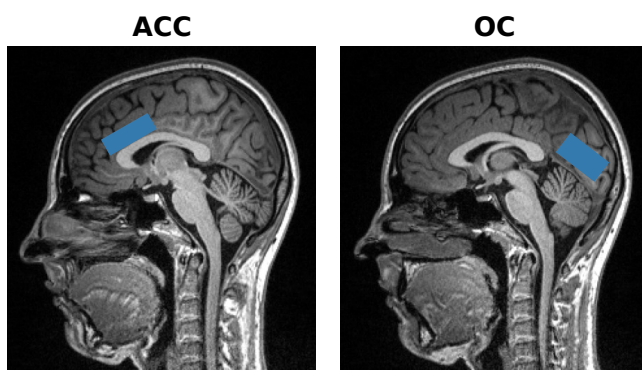


Figure 5.2: Sagittal  $T_1$ -weighted MP-RAGE slices showing the voxel position for the single voxel spectroscopy in the anterior cingulate cortex (ACC,  $V = (36 \times 20 \times 12) \text{ mm}^3$ ) and the occipital cortex (OC,  $V = (35 \times 20 \times 15) \text{ mm}^3$ ).

## 5.2.2 Measurement protocol

The measurement protocol to acquire  $^1\text{H}$  MEGA-PRESS spectra at defined time points is schematically shown in Figure 5.3. First, reference spectra (REF) with and without water suppression were collected prior to the functional stimulation block to quantify the metabolic levels in the resting state. Next, six dynamic runs were consecutively performed, each comprising a stimulation cycle and so-called DUMMY scans. The stimulation cycle in each dynamic run consisted of 56 scans with overall 44 heat stimuli (with duration of 1 s, respectively) where each stimulus was followed by a resting period at the baseline temperature of 31 °C. The duration of this resting period was alternated between 5 and 8 s to toggle between the acquisition of ED and NED spectra during pain stimulation and to avoid wind-up of pain perception (Price et al., 1977). By using a trigger signal of the thermal stimulation unit, single ED and NED spectra were acquired at defined time points: the PAIN state during each stimulus and the REST state 3 s after each stimulation. At the end of each stimulation cycle 24 DUMMY scans were collected without stimulation to allow for recovery and to reduce habituation to the stimuli. In total, the dynamic run was repeated six times to obtain a sufficiently large

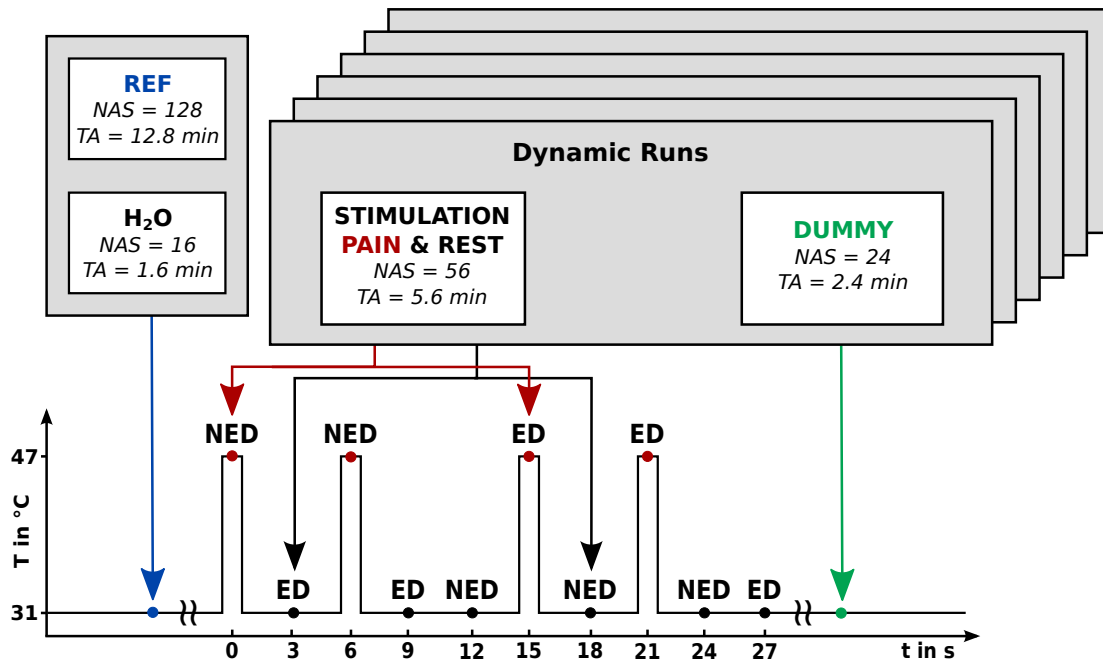


Figure 5.3: Time course of data acquisition of the MRS experiment. After acquiring reference spectra (REF) unsuppressed water data were measured. The following six dynamic runs each consisted of a stimulation cycle during which triggered heat stimuli (stimulus duration of 1 s with inter-stimulus intervals of 5 or 8 s) were applied to the left forearm of the volunteers and NED and ED were acquired at defined time points (PAIN, REST). For PAIN and REST states only a part of the complete stimulus time course is shown to illustrate the toggling between pain stimulation and rest condition during the continuous acquisition of NED and ED spectra (red and black arrows). DUMMY scans are performed without any stimulation to reduce habituation to applied stimuli.

number of scans, where 128 were assigned to ED and NED single acquisition data pairs in PAIN, REST and DUMMY state, respectively.

### 5.2.3 Metabolite measures and statistical analysis

GABA+ and Glx were quantified from the DIFF spectra, as described in Chapter 2.2.6. Moreover, the signal intensities of NAA, tCho and tCr were determined from the NED spectra and the metabolite ratios GABA+/tCr, Glx/tCr, NAA/tCr and tCho/tCr were calculated for REF, PAIN, DUMMY and REST state, respectively.

To test whether tCr remained constant throughout the experiment, tCr was normalized to the intensity of the unsuppressed water signal (tCr/H<sub>2</sub>O ratio). Since tCr signal arises only from WM and GM and water signal from GM, WM and CSF, the brain matter fractions used in Eq. (2.1) for relaxation correction were accordingly adjusted

by excluding CSF volume in case of tCr:

$$f'_{WM} = \frac{f_{WM}}{1 - f_{CSF}} \quad \text{and} \quad f'_{GM} = \frac{f_{GM}}{1 - f_{CSF}} \quad (5.1)$$

For the quantitative analyses of pain evoked metabolic changes only spectra were included that satisfied the pre-defined quality criteria including sufficiently narrow linewidth (FWHM < 0.06 ppm), adequate signal-to-noise ratio (SNR > 70) and sufficient fit quality, excluding spectra with large residuals. FWHM and SNR were determined from the NAA signal of the NED spectrum.

To test the significance of changes of metabolite concentrations during the extended experiments the intra-individual percentage concentration changes were statistically analyzed with respect to the REF state for Glx/tCr, GABA+/tCr, tCr/H<sub>2</sub>O, NAA/tCr and tCho/tCr by using the exact Wilcoxon rank sum test and a significance level of  $p = 0.05$ .

### 5.3 Results

The mean stimulation temperature was ( $46.0^{\circ}\text{C} \pm 1.0^{\circ}\text{C}$ ). Before starting the MR experiment and at the beginning of the last stimulation cycle volunteers were asked to evaluate the stimulation intensity on a VAS scale. The volunteers reported less, increased or no change in pain perception. The mean VAS values sampled at these two time points averaged across all participants resulted in  $5.1 \pm 1.2$  and  $5.0 \pm 1.6$ , respectively. All volunteers reported habituation to the heat stimuli during a single stimulation cycle.

Applying the quality criteria to the spectral data of sufficient GABA+ and Glx fits, narrow linewidths and sufficient SNR led to the inclusion of fifteen datasets for the REF state, ten datasets for the PAIN state, eight datasets for the REST and nine datasets for the DUMMY condition in case of the ACC voxel. For the OC voxel fourteen datasets satisfied the quality criteria for the REF, REST and DUMMY states whereas thirteen datasets were available for the PAIN state. Spectra had mainly to be excluded due to insufficient GABA+ and Glx fitting results. All included spectra revealed narrow linewidths (FWHM<sub>ACC</sub> =  $(0.034 \pm 0.004)$  ppm, FWHM<sub>OC</sub> =  $(0.042 \pm 0.005)$  ppm) and sufficient SNR with respect to the NAA peak. In the OC voxel SNR ( $118.3 \pm 20.1$ ) was higher than in ACC ( $82.6 \pm 10.3$ ) reflecting the slightly different voxel sizes.

Both MRS voxels revealed similar tissue composition with regard to the mean tissue fractions of GM (ACC:  $55.9\% \pm 3.1\%$ ; OC:  $54.5\% \pm 3.5\%$ ), WM (ACC:  $23.7\% \pm 3.2\%$ ; OC:  $31.0\% \pm 2.6\%$ ) and CSF (ACC:  $20.3\% \pm 3.7\%$ ; OC:  $14.5\% \pm 3.9\%$ ).



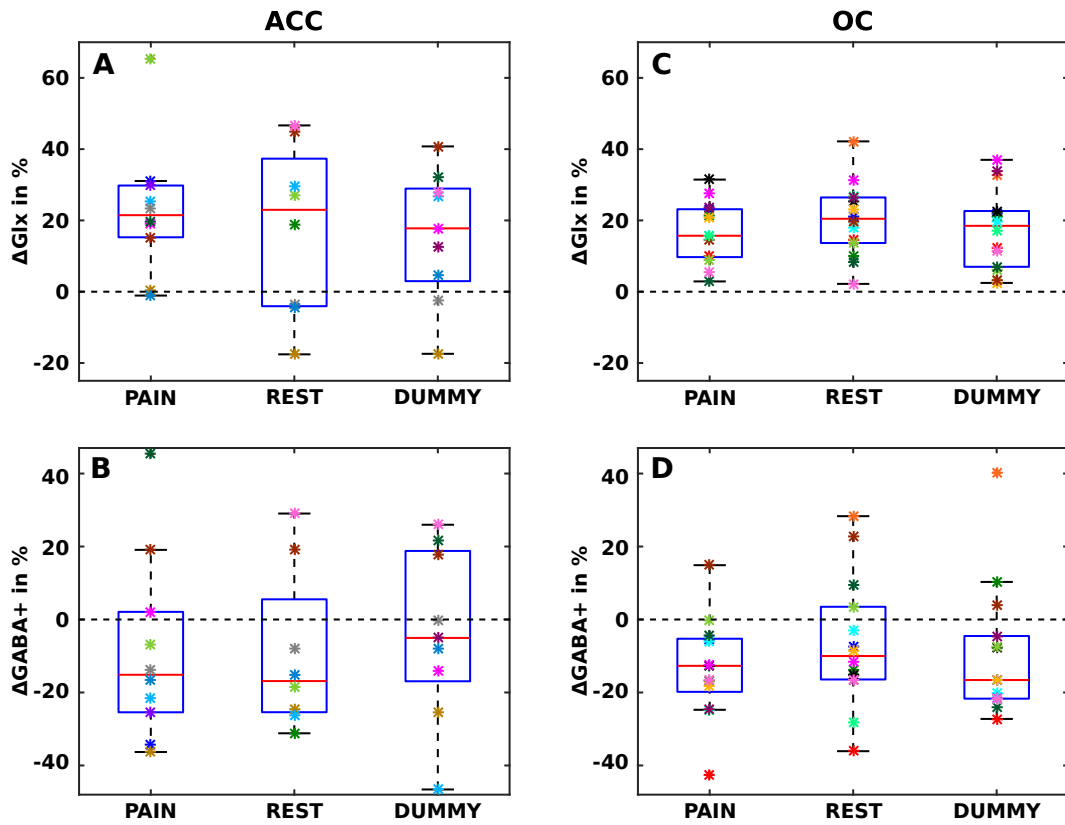


Figure 5.4: Relative concentration changes of Glx/tCr (A, C) and GABA+/tCr (B, D) in ACC (A, B) and OC (C, D), represented in boxplots normalized to the intra-individual REF state (- -) for each volunteer (marked with different colors of the diagram symbols). The solid red line indicates the median value of the distribution. The lower and upper blue lines of the boxes represent the 25<sup>th</sup> and 75<sup>th</sup> percentile, respectively.

Figure 5.4 shows the distribution of the percentage changes  $\Delta\text{Glx}$  and  $\Delta\text{GABA+}$  for the PAIN, REST and DUMMY states relative to the REF condition (zero line) in ACC (Fig. 5.4 A and B) and OC (Fig. 5.4 C and D). These changes were calculated for each subject by normalizing the concentration ratios Glx/tCr and GABA+/tCr in each state to the corresponding ratios in the REF state. Tables 5.1 and 5.2 summarize the median values of the Glx/tCr, GABA+/tCr, NAA/tCr, tCho/tCr and tCr/H<sub>2</sub>O ratios for the different stimulation states, the median values of the intra-individual percentage concentration changes relative to the REF state and the corresponding statistical results of the Wilcoxon rank sum test analysis ( $p$  values).

Unexpectedly, not only the ACC but also the control region OC revealed Glx/tCr and GABA+/tCr level changes during acute pain stimulation. In both brain regions, Glx/tCr was increased significantly in the PAIN state compared to the REF state (ACC: 21.5%,  $p < 0.001$ ; OC: 15.7%,  $p < 0.001$ ), whereas at the same time the GABA+/tCr ratios were both decreased (ACC: -15.1%,  $p = 0.114$ ; OC: -12.7%,

	REF	PAIN	REST	DUMMY
<b>Glx<sub>ACC</sub></b>				
Glx/tCr	0.22 (0.19, 0.23)	0.24 (0.23, 0.28)	0.25 (0.23, 0.27)	0.26 (0.22, 0.28)
$\Delta$ Glx [%]		21.5 (15.3, 29.8)	23.0 (-4.1, 37.3)	17.8 (3.0, 28.9)
$p_{Glx}$		< <b>0.001</b> (10)	0.404 (8)	<b>0.036</b> (9)
<b>Glx<sub>OC</sub></b>				
Glx/tCr	0.20 (0.12, 0.24)	0.21 (0.20, 0.29)	0.24 (0.20, 0.29)	0.24 (0.20, 0.29)
$\Delta$ Glx [%]		15.7 (9.7, 23.1)	20.5 (13.7, 26.4)	18.5 (7.0, 22.6)
$p_{Glx}$		< <b>0.001</b> (13)	< <b>0.001</b> (14)	< <b>0.001</b> (14)
<b>GABA+<sub>ACC</sub></b>				
GABA+/tCr	0.35 (0.28, 0.37)	0.31 (0.28, 0.32)	0.31 (0.26, 0.34)	0.31 (0.28, 0.33)
$\Delta$ GABA+ [%]		-15.1 (-25.4, 2.1)	-16.9 (-25.4, 5.5)	-5.1 (-16.9, 18.8)
$p_{GABA+}$		0.114 (10)	0.083 (8)	0.224 (9)
<b>GABA+<sub>OC</sub></b>				
GABA+/tCr	0.40 (0.35, 0.52)	0.37 (0.32, 0.43)	0.39 (0.33, 0.43)	0.37 (0.33, 0.41)
$\Delta$ GABA+ [%]		-12.7 (-19.8, -5.3)	-10.0 (-16.4, 3.5)	-16.6 (-21.7, -4.5)
$p_{GABA+}$		< <b>0.001</b> (13)	<b>0.041</b> (14)	<b>0.006</b> (14)

Table 5.1: Median values for the concentration ratios in the REF, PAIN, REST and DUMMY state and corresponding concentration changes in % (25<sup>th</sup> and 75<sup>th</sup> percentile in brackets) relative to the REF condition. The  $p$  values represent the results of the intra-individual Wilcoxon rank sum test applied to the intra-individual percentage concentration changes relative to the REF state in PAIN, REST and DUMMY (significant values in bold, number of evaluated datasets in brackets).

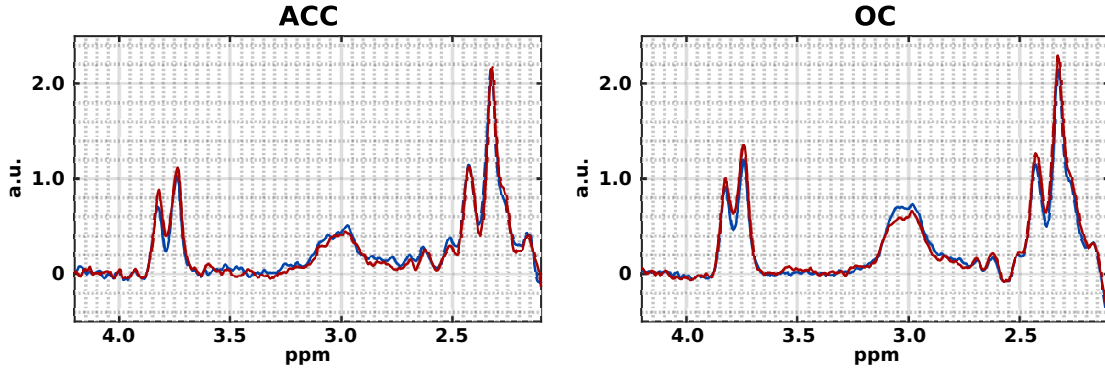


Figure 5.5: Mean <sup>1</sup>H MEGA-PRESS DIFF spectra for REF state (blue) and PAIN state (red) in ACC (*left*) and OC (*right*) averaged over all included datasets. An increase of Glx at 3.75 ppm and a decrease of GABA+ at 3.0 ppm in the PAIN state are clearly seen. Each individual spectrum was normalized to the tCr intensity determined from the AMARES fit of the NED spectra before averaging across individuals.

$p < 0.001$ ). Although the GABA+/tCr decrease in ACC was not significant, a strong decreasing trend can nevertheless be visually identified (Fig. 5.4 B). These changes were also apparent in the Glx and GABA+ signals in the mean <sup>1</sup>H MEGA-PRESS difference

spectra for the REF and PAIN state, which were calculated by averaging all included single acquisition data of the corresponding MRS voxel (Fig. 5.5). The magnitudes of calculated median percentage changes of Glx and GABA+ cannot be directly seen due to a strong influence of extreme values on the calculated mean spectrum, e.g. strong opposing observations of two  $\Delta$ GABA+ values in ACC in PAIN state (Fig. 5.4 B). We found no significant association between perceived pain intensity and metabolic changes.

In ACC and OC, the  $\Delta$ Glx values in the REST and DUMMY state had an opposing trend by slightly decreasing and increasing, respectively, but remaining elevated com-

	REF	PAIN	REST	DUMMY
<i>NAA<sub>ACC</sub></i>				
NAA/tCr	1.04 (1.01, 1.12)	1.05 (1.01, 1.09)	1.07 (1.03, 1.11)	1.06 (1.03, 1.11)
$\Delta$ NAA [%]		0.7 (-0.1, 1.9)	0.7 (-1.5, 1.7)	0.5 (-1.0, 3.0)
<i>p<sub>NAA</sub></i>		0.442 (10)	0.404 (8)	0.709 (9)
<i>NAA<sub>OC</sub></i>				
NAA/tCr	1.36 (1.23, 1.45)	1.39 (1.23, 1.47)	1.37 (1.25, 1.46)	1.38 (1.23, 1.44)
$\Delta$ NAA [%]		0.6 (-0.7, 1.5)	1.0 (-0.3, 1.6)	0.0 (-0.5, 2.2)
<i>p<sub>NAA</sub></i>		0.298 (13)	<b>0.006</b> (14)	1.000 (14)
<i>tCho<sub>ACC</sub></i>				
tCho/tCr	0.40 (0.39, 0.46)	0.43 (0.39, 0.47)	0.39 (0.38, 0.43)	0.39 (0.38, 0.42)
$\Delta$ tCho [%]		2.5 (0.7, 3.0)	-0.3 (-2.0, 1.4)	0.0 (-1.6, 1.8)
<i>p<sub>tCho</sub></i>		0.017 (10)	0.404 (8)	0.709 (9)
<i>tCho<sub>OC</sub></i>				
tCho/tCr	0.21 (0.20, 0.24)	0.21 (0.20, 0.24)	0.21 (0.20, 0.24)	0.21 (0.20, 0.24)
$\Delta$ tCho [%]		-1.0 (-3.5, 0.6)	-0.9 (-2.4, 0.6)	-1.2 (-2.4, -0.6)
<i>p<sub>tCho</sub></i>		0.298 (13)	0.177 (14)	< <b>0.001</b> (14)
<i>tCr<sub>ACC</sub></i>				
tCr/H <sub>2</sub> O * 10 <sup>3</sup>	0.43 (0.41, 0.46)	0.43 (0.41, 0.45)	0.43 (0.41, 0.45)	0.43 (0.42, 0.45)
$\Delta$ tCr [%]		-0.8 (-1.1, -0.2)	-0.2 (-2.0, 1.2)	-1.2 (-2.7, 0.2)
<i>p<sub>tCr</sub></i>		<b>0.001</b> (10)	1.000 (8)	0.709 (9)
<i>tCr<sub>OC</sub></i>				
tCr/H <sub>2</sub> O * 10 <sup>3</sup>	0.42 (0.40, 0.44)	0.42 (0.39, 0.45)	0.42 (0.39, 0.44)	0.42 (0.39, 0.44)
$\Delta$ tCr [%]		-0.2 (-1.6, 0.8)	-0.4 (-1.7, 0.6)	-0.4 (-1.7, 0.4)
<i>p<sub>tCr</sub></i>		0.742 (13)	0.507 (14)	0.177 (14)

Table 5.2: Median values for the concentration ratios in the REF, PAIN, REST and DUMMY state and corresponding concentration changes in % (25<sup>th</sup> and 75<sup>th</sup> percentile in brackets) relative to the REF condition. The *p* values represent the results of the intra-individual Wilcoxon rank sum test applied to the intra-individual percentage concentration changes relative to the REF state in PAIN, REST and DUMMY (significant values in bold, number of included datasets in brackets).

pared to the REF state (see Fig. 5.4). In OC, the median value of  $\Delta\text{GABA}+$  remained decreased in the REST and DUMMY state, whereas in the ACC the median value in the DUMMY state was closer to the baseline value.

Since the median  $\text{Glx}/\text{tCr}$  and  $\text{GABA}+/\text{tCr}$  values remained on a similar level during (PAIN) and after stimulation (REST and DUMMY), the corresponding metabolite ratios were pooled to an average stimulation state (STIM) for each subject individually. The individual stimulus evoked  $\text{Glx}/\text{tCr}$  increases and  $\text{GABA}+/\text{tCr}$  decreases are displayed in Figure 5.6, which visualizes the range of  $\text{Glx}/\text{tCr}$  and  $\text{GABA}+/\text{tCr}$  ratios in ACC (Fig. 5.6 A and B) and OC (Fig. 5.6 C and D) before (REF) and during and after the stimulation (STIM).

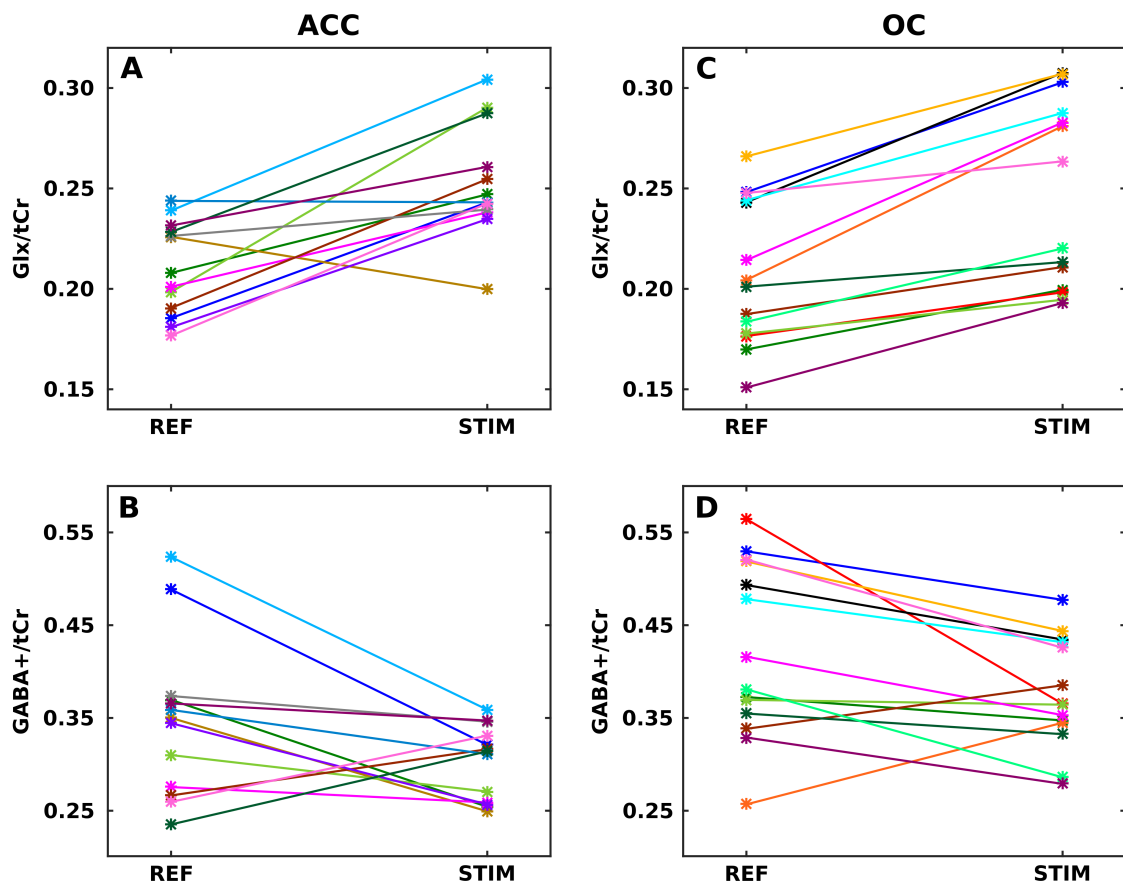


Figure 5.6: Changes of  $\text{Glx}/\text{tCr}$  (A, C) and  $\text{GABA}+/\text{tCr}$  (B, D) in ACC (A, B) and OC (C, D) for each volunteer (marked with different colors of the diagram symbols) for the REF and STIM states (stimulation state, averaged over all data of the PAIN, REST and DUMMY states).

The  $\text{NAA}/\text{tCr}$ ,  $\text{tCho}/\text{tCr}$  and  $\text{tCr}/\text{H}_2\text{O}$  ratios in ACC and OC remained relatively constant across the different stimulation states with percentage changes below 2.5% in the PAIN, REST and DUMMY states relative to the REF condition (see Tab. 5.2). Although some of these changes reached statistical significance, they were very small

compared to the changes of GABA+ and Glx. Thus, it can be assumed that these metabolites (NAA, tCho and tCr) were not or only minor affected by the pain stimuli. Moreover, to minimize motion the subjects' heads were carefully fixated by padding during the experiments. The very small changes observed for tCr, NAA and tCho suggest that subject motion during the experiments was not a major limitation.

## 5.4 Discussion

In the study presented in this chapter,  $^1\text{H}$  MEGA-PRESS spectroscopy was applied in a group of female volunteers to explore simultaneously pain-induced changes of GABA+ and Glx. Changes in metabolite concentrations ratios were identified in both investigated brain regions, in ACC as well as in OC.

The the ACC was selected since it is known to be activated during pain perception (Apkarian et al., 2005), pain related attention and emotional processing (Peyron et al., 2000). Thus, regarding the neurotransmitter mediated regulation of neuronal activity, changes in the neurotransmitter levels were expected upon stimulation with acute pain stimuli. In contrast, the observed metabolite concentration changes in the OC were surprising since the OC is not a primary part of the pain processing network. In order to discuss these observations, the OC voxel was further explored with regard to its functional and morphological characteristics. The subcortical segmentation results obtained by analyzing the  $T_1$ -weighted MRI data with the Freesurfer tool were used to determine the fractions of different subcortical areas within the spectroscopic voxel. Averaged over all subjects, the GM within the voxel revealed approximately 20% precuneus fraction, but no posterior cingulate cortex, which is directly involved in pain processing (Peyron et al., 2000). Interestingly, it has been recently shown that the default mode network (DMN) as well as the precuneus, which also belongs to the DMN, exhibit pain related activation (Maleki et al., 2013; Minassian et al., 2013; Owen et al., 2008). The DMN is a network of brain regions being active in the resting state (Raichle et al., 2001). Minassian et al. supposed internal mentation processes associated with episodic memory retrieval being responsible for activation of the DMN. Furthermore, recent fMRI and PET studies also reported the precuneus to be activated in motor imagery (Cavanna and Trimble, 2006). All volunteers participating in this study were asked to avoid any motion during the stimulation, thus the observed metabolic changes in OC may also be related to the volunteer's urge to remove the thermode from the stimulated body part. Taken together, both investigated brain regions revealed similar changes of Glx/tCr and GABA+/tCr in the PAIN state. This indicates that perception of acute pain obviously involves not only neurochemical changes in pain processing

brain regions, such as the ACC, but is also associated with neurochemical alterations in OC.

As the most important finding of the presented study, significant increases of Glx with a simultaneous decrease of GABA+ in both brain regions during pain perception were observed. Considering the fact that the major signal contribution to Glx arises from both Glu and Gln (Veenendaal et al., 2016) (see also Chapter 4.1.2), this increase of Glx in ACC and OC can be ascribed to elevated glutamatergic neurotransmission and the related Glu/Gln cycling due to the increased activity of the excitatory system, but also to increased energy metabolism or both. The reduced GABA+ levels are interpreted to reflect a down-regulation of inhibition during pain processing. The results for Glx are in line with findings of Mullins et al. (Mullins et al., 2005) and Gussew et al. (Gussew et al., 2010), who also observed Glx and Glu increases in the anterior cingulate cortex and insular cortex during perception of cold and heat acute pain. Glu levels were determined by using a STEAM (TE = 20 ms, B<sub>0</sub> = 4 T) and a PRESS sequence (TE = 30 ms, B<sub>0</sub> = 3 T), respectively, that allow a more reliable detection of Glu compared to the MEGA-PRESS sequence applied here. Furthermore, the obtained GABA results are in accordance with animal studies (Jasmin et al., 2003), which identified the inhibition of GABA neurotransmission in the insular cortex of rats as a trigger for an elevated pain sensation. Similar results as in the present study were also obtained by Hasler et al. (Hasler et al., 2010), who reported GABA decreases evoked by psychological stress in the human prefrontal cortex and ascribed them to reduced inhibitory influence of GABA on neural circuits involved in responding to stress or threat.

In contrast to the presented results, Kupers et al. (Kupers et al., 2009) reported an increase of GABA, but no changes in Glu and Glx in the rostral anterior cingulate cortex of healthy subjects. The experiments were also performed on a 3 T scanner, but using a conventional 1D MRS sequence (double spin echo method, TE = 20 ms) instead of the J-difference editing approach <sup>1</sup>H MEGA-PRESS. As discussed in Chapter 2.2, quantifying GABA based on conventional MRS data at 3 T is usually hampered by strong signal overlapping from other brain metabolite signals (see also Fig. 2.2). Thus, the reported GABA level changes by Kupers et al. might be questionable. These contradictory findings are not clarified yet and may be the result of the different investigated brain regions or differences in the applied pain stimulation protocols between the two studies. In contrast to the presented study here, Kupers et al. used continuous painful heat stimulation of 4 min duration (stimulation temperature 46.7°C ± 0.2°C).

One persistent difficulty with *in vivo* brain MRS is the assignment of the measured metabolite changes to a neurotransmitter turnover, especially in case of spectroscopically

measured Glu or Glx intensities (see Chapter 2.3.1 and 4.1.2). The attribution to the origin of the measured Glx changes remains unspecific since the spectroscopic voxels included both GM and WM, which in turn consist of neurons and glial cells with different proportions of Glu and Gln, respectively (Rae, 2014). However, due to the strong functional interaction of excitatory and inhibitory mechanisms under healthy conditions (Stagg et al., 2011b), it can be hypothesized that the changes in GABA+ and also in Glx observed here may primarily be ascribed to the modulation of neurochemical processes underlying the regulation of neuronal activity.

Although the current experiment aimed to extract time-resolved neurochemical information associated with pain processing in the human brain, the results concerning the time course of pain processing in the REST and DUMMY state are unfortunately not clear-cut. As stated before, no definite trend was identified neither for GABA+/tCr nor for Glx/tCr. The results indicate that the time scale of the experiment was obviously too short to reach a steady state level for Glu and GABA+. This might be explained by different effects. First, repeated stimuli were applied and the REST spectra were acquired 3s after each stimulus. Although the results indicate that painful stimuli initiate brain activity resulting in neurotransmitter concentration changes, this brain activity seems to persist longer than 3s and sustained concentration levels were consequently observed in the REST state. Second, a recent study by Mangia et al. (Mangia et al., 2007) investigated Glu dynamics during visual stimulation by performing fMRS experiments at 7 T. Dynamic metabolite courses of 40s time resolution were extracted by applying a sliding window approach to the acquired fMRS data that was possible due to the improved sensitivity of measurements at high field strengths. In one experiment prolonged stimulation was applied for 5.3 min, repeated twice with a resting period of the same length in between (similar to the present DUMMY state). During the stimulation blocks the Glu concentration reached a new steady state, followed by a gradual return to the baseline concentration during rest. The second stimulation block resulted again in a Glu increase, but with smaller amplitude. Comparing these observations with the results of the current experiment, one explanation could be that the Glx and GABA+ concentration changes became smaller during the six repeated dynamic runs. Furthermore, the resting period was a factor of two shorter compared to the study of Mangia et al., which most likely prevented a complete return to baseline level concentrations when tacitly assuming the same metabolite dynamics in both studies. This should further be put in relation to the volunteers' reports, who not only described decreasing pain perception during each stimulus block with painful sensations being noticed primarily in the beginning, but also post-stimulus pain sensations during the DUMMY measurements. These assessments in combination with the observed

metabolite concentrations changes suggest that pain perception elicits intra-individual effects that last longer than the temporal resolution used here. Consequently, data averaging across pain stimulation states and omitting the time-resolved data acquisition scheme may be more advantageous for future studies, resulting in shortened measurement times and reduced habituation effects.

The ratios Glx/tCr, GABA+/tCr, NAA/tCr, tCho/tCr and tCr/H<sub>2</sub>O showed distinct inter-individual variations (see Tab. 5.1 and 5.2). In case of GABA+/tCr, the fraction of macromolecules contributing to the GABA+ signal is also expected to be different for each volunteer, resulting in increased variation of this metabolite ratio (Mader et al., 2002) (see Fig. 5.6 B and D). Despite these limitations, however, it was possible to detect concentration changes in PAIN, REST and DUMMY states relative to a REF condition.

Notwithstanding this, <sup>1</sup>H MRS is certainly unable to resolve the processes on a cellular or synaptic level due to the large voxel sizes that cause partial volume effects, restricting identification and localization of the processes involved in pain processing. Furthermore, several other stimulus related effects, such as sensory perception, habituation, attention and anticipation, may also blur neuronal activations. Consequently, further improvements of the stimulation design would be advantageous to allow more specific assignments of the observed effects. Habituation to the applied stimuli could be reduced by increasing the novelty of the presented stimulus, e.g. by variation of its intensity and duration, or by performing the fMRS measurements at higher field strengths ( $\geq 7$  T), which would not require the time consuming J-difference editing strategies to resolve GABA.

The current study is one of the first that demonstrates the response of the excitatory and inhibitory neurotransmitter system to pain stimuli in ACC and OC *in vivo* using <sup>1</sup>H MEGA-PRESS proving the applicability to explore stimulus-induced metabolite concentration changes.



# Chapter 6

## Combined *in vivo* functional MRS and functional MRI during painful stimulation

In this chapter, the results of combined measurements of functional MRS and fMRI data during pain perception are presented. An appropriate measurement protocol was set up in a preliminary study to enable most similar pain stimulation conditions for both modalities that was explored in terms of BOLD signal variations in selected pain processing brain regions. Based on these investigations, a brain region for the fMRS measurements was selected revealing most constant activation during prolonged heat pain stimulation. This experiment setup was then applied to a group of healthy male volunteers to explore possible interrelations between GABA+, Glx and BOLD signal values. Parts of this chapter have previously been presented at international conferences (Cleve et al., 2016a, 2017b) and are submitted to a journal for publication as an article (Cleve et al. (2017a), revision in progress).

### 6.1 Motivation

The investigation of metabolic processes associated with brain activity and their relation to the neurovascular coupling (Logothetis, 2008) is of particular interest in studying the brain. Specifically, combining quantitation of brain metabolites and the amplitudes of the functional BOLD response to a stimulus is subject of current research (Duncan et al., 2014), which aims to tackle the question about the interrelation between metabolite levels and BOLD signal changes following neuronal activation. While functional MRI is sensitive to changes in blood oxygenation levels that are related to the energy consumption of task-specifically activated brain regions,  $^1\text{H}$  MRS provides a complementary

tool to non-invasively monitor brain metabolites *in vivo* since the neuronal processes regulating brain activity measured with fMRI remain hidden.

Recent studies have demonstrated associations between resting state GABA levels and stimulus-induced BOLD signal changes in the same brain region in healthy volunteers. Negative associations between GABA levels and task-positive BOLD responses were observed with visual (Bednařík et al., 2015; Donahue et al., 2010; Muthukumaraswamy et al., 2009, 2012; Violante et al., 2013) and motor activation (Stagg et al., 2011a) as well as with negative BOLD signal changes during emotional processing (Northoff et al., 2007). These associations thus indicate stronger BOLD responses to be linked with lower inhibitory neurotransmitter levels in the resting state. Besides these intra-regional findings, interrelations between GABA and Glu levels and BOLD responses or functional connectivity strengths were also observed in different brain networks (Duncan et al., 2011; Falkenberg et al., 2012; Kapogiannis et al., 2013; Wagner et al., 2016) potentially reflecting small scale synchrony of microcircuits related to the interaction of neuronal excitation and inhibition (Duncan et al., 2014).

So far, however, most studies have focused on measuring resting state metabolite levels, and only few studies have investigated the interrelation between task-induced neurotransmitter level changes and BOLD responses (Bednařík et al., 2015; Ip et al., 2017; Kühn et al., 2016). Investigating the visual cortex, Bednařík et al. observed a positive correlation between Glu level changes and BOLD responses during neuronal activation. Beyond, Ip et al. found that the time courses of visual stimulus evoked Glu changes and BOLD signal alterations are positively associated. Moreover, Kühn et al. reported GABA increases in the anterior cingulate cortex during a Stroop task that were negatively associated with the intra-regional BOLD signal changes.

Brain regions with BOLD responses during pain processing are well known (Apkarian et al., 2005), and previous fMRS studies (see also Chapter 5) already demonstrated pain-induced changes of GABA, Glu and Glx (Cleve et al., 2015; Gussew et al., 2010; Gutzeit et al., 2011; Mullins et al., 2005). This raises the challenging question if associations exist not only between resting state GABA and Glu levels but also between their acute pain evoked changes and the corresponding BOLD responses. This can be investigated by performing combined fMRS/fMRI experiments.

To this end, acute heat pain stimulation was applied during the acquisition of whole brain fMRI and fMRS data of healthy subjects to explore potential interrelations between metabolite levels and pain evoked BOLD signal changes in a brain region being activated during pain perception (intra-regional exploration) as well as in other pain processing regions (inter-regional exploration). To reduce habituation during prolonged stimulation a new measurement protocol was set up that is presented in the following

section. An MRS target region was selected that was most consistently activated during stimulation over the required measurement time for both modalities. One important aspect of the study was to test, whether the induced GABA and Glx concentration changes were observable in the selected brain region, and, if so, whether these changes were associated with the amplitude of BOLD signal changes as seen with whole brain fMRI. It was hypothesized, based on the results in Chapter 5, that GABA reveals a negative change during acute heat pain stimulation while Glx shows an increase at the same time. Furthermore, BOLD signal changes in the MRS target region were expected to reveal a negative association with resting state GABA levels, as well as a positive correlation with the pain-induced Glx level changes. No specific assumption was made about a possible interrelation between GABA, Glx and whole-brain BOLD signal changes that was investigated in an explorative manner.

## **6.2 Preliminary examinations**

As discussed in Chapter 5.4 habituation to repeated acute heat pain stimuli poses a challenge for acute pain experiments, because when stimuli are applied repeatedly, neuronal activity is usually reduced (Apšvalka et al., 2015; Grill-Spector et al., 2006), known as a repetition suppression effect. Therefore, a new stimulation paradigm was set up and evaluated in a preliminary fMRI study during 11 min of heat pain stimulation. Besides exploring habituation related temporal variations of the measured BOLD signal, it was additionally investigated which pain processing brain region showed the most constant activation for prolonged heat pain stimulation over time, and was thus suitable for the extended combined fMRS and fMRI measurements of the main study.

### **6.2.1 Stimulation paradigm and experiment design**

As concluded from the results of the fMRS experiment (Chapter 5), block design based data acquisition, thus not distinguishing between the stimulus and inter-stimulus states, seems to be beneficial for pain stimulation experiments by allowing for reduced measurement times that is of major importance for acute pain stimulation studies. Habituation can be reduced by increasing the level of novelty of the applied heat stimuli by varying their duration and intensity. Additionally, the effect of elevated pain sensation due to wind-up (see Chapter 5.2.2) was exploited in the new stimulation paradigm by increasing the frequency of the presented stimuli within one block to 0.33 Hz. Moreover, the stimulation area was changed from the inside of the left forearm to the back of the left hand according to Penfield's homunculus (Penfield and Boldrey,

1937), which indicates that the hand is much more sensitive to sensory inputs compared to the forearm.

To explore habituation with the new stimulation paradigm over time, four healthy volunteers (one female, three male, one subject investigated twice,  $32 \pm 9$  years) were investigated. The fMRI protocol (EPI sequence, three measurements: Tab. A.3:3, two measurements: Tab. A.3:4) consisted of 20 alternating baseline and stimulation periods of 16 s duration each, resulting in an acquisition time of 11 min (see Fig. 6.1 A). Painful heat stimuli were applied using the thermal stimulation unit described in Chapter 5.2.1. At baseline, temperature was held constant at  $31^\circ\text{C}$ , whereas during stimulation three heat pulses were applied (pulse 1 (2 s):  $T_{max} - 2^\circ\text{C}$ ; pulse 2 (1 s):  $T_{max}$ ; pulse 3 (3 s):  $T_{max} - 2.5^\circ\text{C}$ ) with an inter-stimulus interval of 3 s during which temperature was allowed to return to baseline (see Fig. 6.1 B). The stimulation temperature  $T_{max}$  was individually adjusted in a pre-test performed on the back of the left hand. First, the heat pulse paradigm was applied to the volunteers at a non-painful temperature ( $T_{max} = 42^\circ\text{C}$ ) for training. Afterwards, single heat pulses of 1 s duration were applied with an inter-stimulus interval of 30 s and with increasing temperature ( $1^\circ\text{C}$  steps,  $42^\circ\text{C} - 51^\circ\text{C}$ ). The volunteers were asked to rate each pulse on the VAS scale ranging from zero to ten. The individual stimulation temperature  $T_{max}$  was chosen at a VAS value of 5. During the MR session the heat pain stimulation was applied to the back of the right hand to avoid any pre-experimental sensitization of the skin.

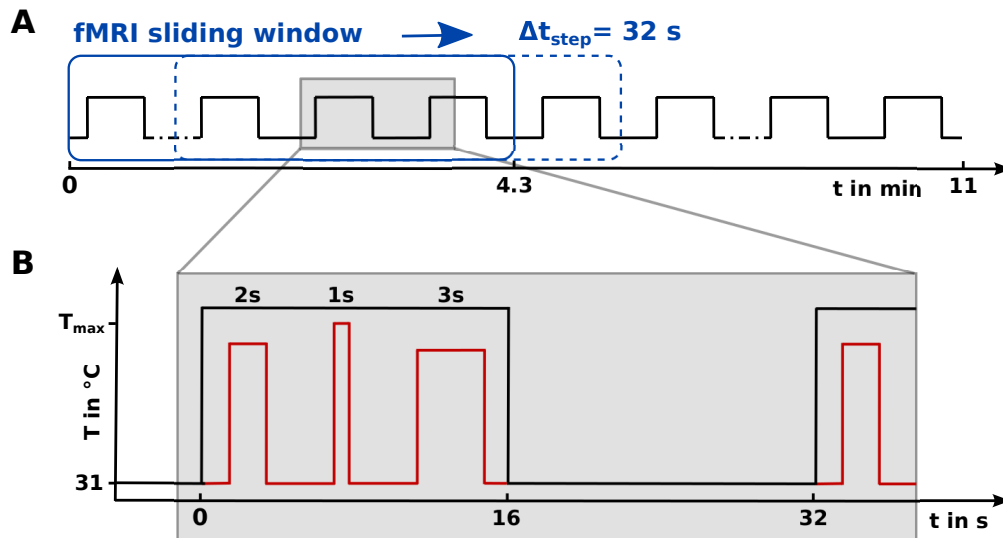


Figure 6.1: (A) Alternating baseline and stimulation blocks of 16 s duration each during fMRI data acquisition and fMRI data processing scheme by using a sliding window (blue) with a step size  $\Delta t_{step}$  of 32 s resulting in twelve time steps. (B) Sequence of applied heat pain stimuli of varying duration and intensity with an inter-stimulus interval of 3 s.

## 6.2.2 Data analysis

The EPI series were analyzed with the SPM8 software package as described in Chapter 2.4.3 using a Gaussian kernel of  $\text{FWHM} = 6 \text{ mm}$  for smoothing. To identify temporal BOLD signal variations, the data were stepwise processed by shifting a time window of 4.3 min with step size  $\Delta t_{step}$  of 32 s (Fig. 6.1 A), resulting in twelve different windows. Statistical parametric maps for the stimulation *vs.* baseline contrast coefficient ( $\beta_1$ ) and for the constant term in the regression ( $\beta_2$ ) were obtained for each window (see also Fig. 2.13 D). To explore the BOLD signal changes in different brain regions of interest (ROI), corresponding masks were manually defined in MNI space for four regions that are known to be involved in pain processing (left and right insula (rIns, lIns), ACC and precuneus (Apkarian et al., 2005), see Fig. 6.2). Corresponding masks were then transformed into each individual EPI dataset to calculate the time course of the mean BOLD signal ( $\text{BOLD}_{window}$ ) in the selected brain regions.  $\text{BOLD}_{window}$  was calculated in percentage by dividing voxelwise  $\beta_1$  by  $\beta_2$  and averaging the resulting values over the corresponding ROI volume (Bednařík et al., 2015):

$$\text{BOLD}_{window} = \overline{\left(\frac{\beta_1}{\beta_2}\right)_{ROI}} \cdot 100 \quad (6.1)$$

Finally, to quantify relative habituation over time, the time course of the BOLD signal changes,  $\Delta\text{BOLD}$ , was calculated relative to the first processing step for the twelve time windows for each ROI and volunteer, respectively.

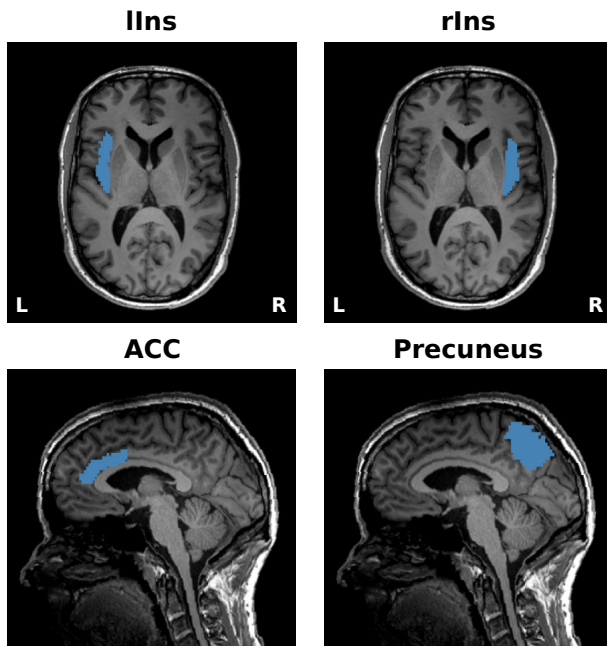


Figure 6.2: Transverse and sagittal  $T_1$ -weighted MP-RAGE slices showing ROI masks defined in MNI space for left and right insula (lIns, rIns), anterior cingulate cortex (ACC) and precuneus transformed to single subject space.

Stimuli related activation of brain regions was assumed, if, first, more than 10 % of the voxels within the corresponding ROI ( $N_{voxel}$ ) exceeded an explorative significance threshold of  $p < 0.05$  (uncorrected) for at least one time window and, second, the subject specific mean BOLD value within a ROI was positive, indicating a positive BOLD response to the applied stimuli. The temporal variation of the number of significantly activated voxels,  $N_{voxel}$ , was correlated with the time course of the BOLD amplitude for each ROI and each volunteer using the Pearson correlation coefficient  $R$ .

### 6.2.3 Results and conclusion

All volunteers showed pain stimuli related brain activation in lIns and rIns, four in ACC and two in precuneus. The range of mean BOLD signal values for activated brain regions for the first time window is listed in Table 6.1 showing the highest activation in lIns at the beginning of the experiment. The relative BOLD signal changes  $\Delta$ BOLD over the duration of nociception are shown in Figure 6.3. lIns and rIns revealed smaller variations compared to ACC and precuneus in all subjects. The BOLD signal in insular cortices decreased by up to 50 % after a stimulation time of 9 min. ACC and precuneus showed higher inter-individual variations with increased stimulation duration. In conclusion, a measurement time period of 9 min should not be exceeded when applying acute pain stimulation with the presented stimulation paradigm. However, a habituation related decrease of BOLD signal of approximately 50 % (at maximum) can obviously not be avoided.

	BOLD <sub>1</sub> in %	R (BOLD <i>vs.</i> $N_{voxel}$ )
lIns	[0.14, 0.31]	[0.74, 0.90]
rIns	[0.16, 0.26]	[0.56, 0.95]
ACC	[0.06, 0.30]	[0.74, 0.89]
Precuneus	[0.10, 0.12]	[0.23, 0.80]

Table 6.1: Range of mean BOLD-fMRI amplitudes after 4.3 min of stimulation in lIns, rIns, ACC and precuneus, and range of the correlation coefficient  $R$  between relative BOLD signal change and number of significant ( $p < 0.05$ ) activated voxels for each brain region.

Furthermore, the correlation between the time courses of BOLD amplitude and  $N_{voxel}$  was significant for all ROIs (except for one volunteer in rIns and precuneus), supporting that mean BOLD signal changes are related to functional habituation, and are not caused by, e.g., single, randomly highly activated voxels within the ROIs.

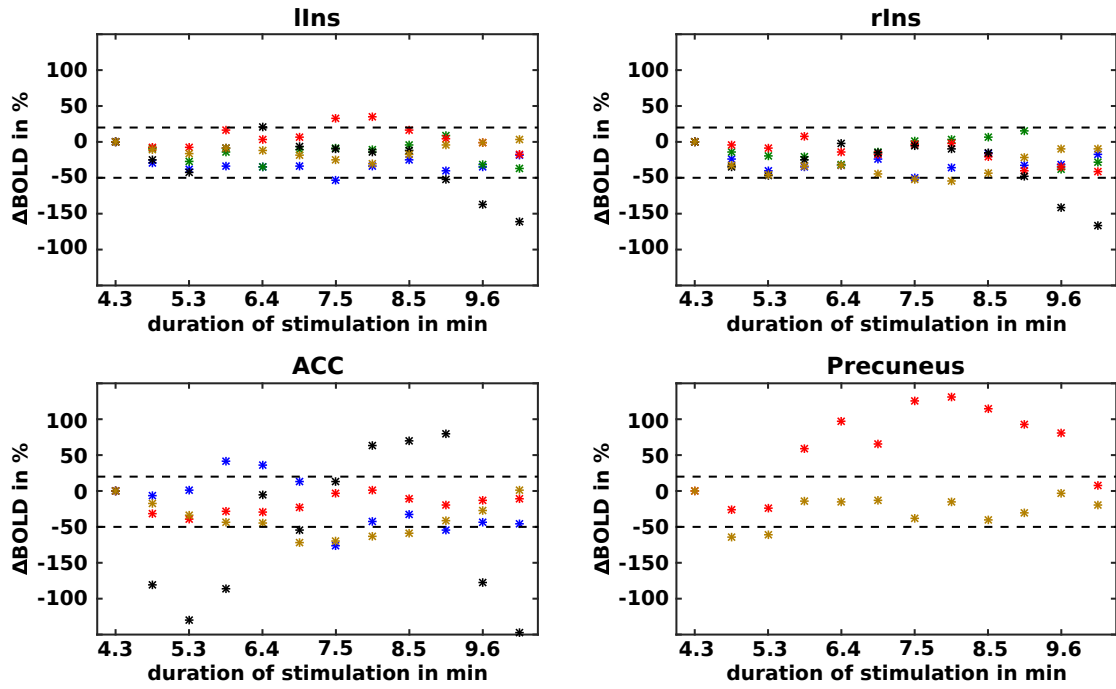


Figure 6.3: BOLD signal changes relative to the first processing step ( $\Delta$ BOLD) for the twelve time windows in the four investigated brain regions *vs.* duration of heat pain stimulation. All volunteers (marked with different colors of the diagram symbols) showed pain stimuli related brain activation in lIns and rIns, four in ACC and two in precuneus. Dashed lines depict the same percentage interval in all plots.

## 6.3 Experiment setup

### 6.3.1 Measurement protocol

Based on the results of the preliminary study described in section 6.2, the left insular cortex was selected as target region for the functional spectroscopic measurements, since it turned out to be the strongest and most consistently activated brain structure across the investigated volunteer group even during prolonged heat pain stimulation. The protocol for the combined measurement of fMRS and fMRI is schematically depicted in Figure 6.4. The fMRI and fMRS measurements during pain stimulation (PAIN) were split into two parts, while a resting period (REST) of 17 min duration after 9 min of pain stimulation was inserted to allow for a recovery phase. During this phase the volunteers were instructed to relax but avoid to fall asleep. During each PAIN block, fMRI data were acquired first, followed by fMRS. During both functional runs within one PAIN block heat pulses were applied to the back of the right hand with the stimulation temperature  $T_{max}$  being individually determined as described in Chapter 6.2.1. The stimulation paradigm (see Fig. 6.1) was applied during fMRI (eight

baseline-stimulation-periods) and fMRS (22 baseline-stimulation-periods) measurements. During reference and stimulation data acquisitions the volunteers were asked to keep their eyes open and to fixate on a white cross on black background displayed on a screen placed in the MR scanner. Prior to the start of the heat pain measurements, volunteers were instructed to avoid stimuli related sudden movements. Immediately after the experiment, the volunteers rated again the sensation of the heat pulse series, which allowed documentation of any possible habituation effects.

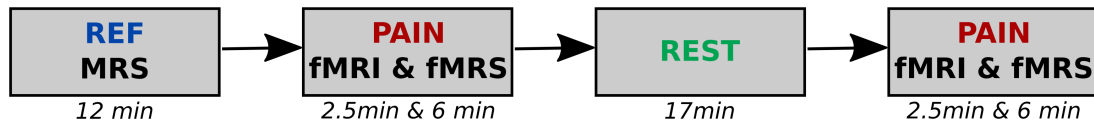


Figure 6.4: Measurement protocol. Following acquisition of reference spectra (REF) two identical pain stimulation blocks (PAIN), each including fMRI and fMRS data measurements, were applied, which were separated by a resting phase (REST). MR-triggered heat stimuli were applied to the right back of the hand of the volunteers. During REST no stimuli were applied.

### 6.3.2 Volunteers

Women were explored in the fMRS study presented in Chapter 5, because they are more sensitive to pain than men. However, it was demonstrated that women show stronger adaption and habituation to repeatedly applied painful stimuli (Hashmi and Davis, 2009). Consequently, male subjects were investigated in the following study to reduce impact of habituation effects on the serial fMRS and fMRI measurements. Twenty-seven right-handed healthy male volunteers ( $24.9 \pm 3.0$  years) were recruited without any known brain disorder or other chronic disease, including chronic pain or diseases requiring medication. The experiments were not performed during any indisposition to avoid interfering effects on pain perception. Furthermore, the volunteers were asked to abstain from alcohol intake within the last 24 hours, smoking within the last two hours and caffeine consumption one hour before the measurements. Prior to the measurements volunteers gave written consent following the guidelines of the local ethics committee after having been fully informed about the experiment including all possible risks.

### 6.3.3 Functional MRS data acquisition and analysis

The spectroscopic voxel was positioned in the left insular cortex ( $V = (28 \times 40 \times 14) \text{ mm}^3$ , MNI coordinates of voxel center:  $x = -44, y = -8, z = 2$ , see Fig. 6.7). MRS data were



acquired with the  $^1\text{H}$  MEGA-PRESS sequence before (REF) and during stimulation (PAIN, see Tab. A.1:17 - A.1:19, A.3:5). As illustrated in Figure 6.4, the MRS measurements during pain stimulation were split into two blocks.

The spectroscopic data were processed as described in Chapter 3.1. and pooled to mean REF and PAIN spectra, respectively. The metabolite signals were quantified as described in Chapter 2.2.6. The signal intensity of tCr was determined from the mean NED spectra. Signal intensities of GABA+ and Glx were quantified from the mean DIFF spectra and normalized to tCr. The resting state metabolite ratios GABA+/tCr and Glx/tCr were used for the subsequent analyses. Pain-induced changes are denoted by  $\Delta\text{GABA+}$  and  $\Delta\text{Glx}$  (with  $\Delta\text{Met} = 100 \cdot ((\text{Met}/\text{tCr})_{\text{PAIN}} / (\text{Met}/\text{tCr})_{\text{REF}} - 1)$ ).

### 6.3.4 Functional MRI data acquisition and analysis

Functional imaging data were acquired first during each of the two pain stimulation blocks with a standard gradient-echo EPI sequence (Tab. A.3:6).

The time series were used to determine pain evoked BOLD signal changes, which were subsequently correlated with the resting state metabolic levels as well as with the stimulus-induced changes of GABA+ and Glx in the insular cortex.

A schematic overview over the processing and analysis steps is given in Figure 6.5. First, the fMRI data were analyzed as described in Chapter 2.4.3 using a fully automated SPM12 pipeline while applying motion and slice-time corrections (see Fig. 6.5 A) and transformation to MNI space. Next, the functional data were spatially smoothed with a Gaussian kernel of  $\text{FWHM} = 6$  mm. The first three volumes of each EPI series were excluded from the PAIN blocks to ensure equilibrium state of the longitudinal magnetisation before concatenating the data of the two fMRI sessions. A general linear model was then applied to create statistical parametric maps for extracting the stimulation *vs.* baseline contrast coefficient and the constant term of the regression. To account for possible scanner related offsets between the first and the second fMRI measurement two separate constant regression terms were determined. For each volunteer, a map of BOLD signal changes (BOLD in %) was calculated by voxel-wise dividing the stimulation *vs.* baseline contrast coefficients by the mean of both constant regression terms (see also Eq. 2.19).

A group analysis (see Fig. 6.5 B) was performed with the parameter estimates obtained from the single-subject level analysis to test for the significance of voxels associated with the stimulation. The significance threshold was set to  $p < 0.05$  (FWE corrected) at the voxel-level and to  $p < 0.05$  (FWE corrected) at the cluster-level corresponding to a spatial extent threshold of seven voxels per cluster.

For the intra-regional associative analysis between metabolite levels (GABA+/tCr,

Glx/tCr,  $\Delta$ GABA+ and  $\Delta$ Glx) and BOLD responses (see Fig. 6.5 C), binary 3D masks of the MRS voxel in the insular cortex were created for each subject by using the geometric meta-information from the MRS data files and then transformed to the MNI space. In the next step, these MRS voxel masks were combined with a binary mask of significantly activated brain regions from the previous group analysis. These combined masks were finally applied to the individual maps of BOLD amplitude changes to calculate the subject-specific mean BOLD amplitude changes within the volume of interest.

To investigate exploratively possible interrelations between insular GABA+/tCr, Glx/tCr,  $\Delta$ GABA+,  $\Delta$ Glx and BOLD in other brain regions (inter-regional analysis), a whole-brain multiple regression analysis was performed with SPM12 (see 6.5 D). Thereby, the GABA+/tCr and Glx/tCr as well as the  $\Delta$ GABA and  $\Delta$ Glx values were selected as regressors. The multiple regression analysis was masked with the mask image created from the group analysis (pain stimulation *vs.* baseline,  $p < 0.05$  uncorrected) to focus on significant correlations between fMRI activation and metabolite measures only in voxels showing pain related activation. The correlations between metabolite levels and BOLD responses to heat pain stimulation were thresholded at an uncorrected voxel-level of  $p < 0.005$  with a minimum cluster size of 25 voxels according to the expected number of voxels  $k_E$  extracted from the SPM analysis. Finally, subject-specific mean BOLD signal changes were extracted from the significant clusters that were identified from the regression analysis.

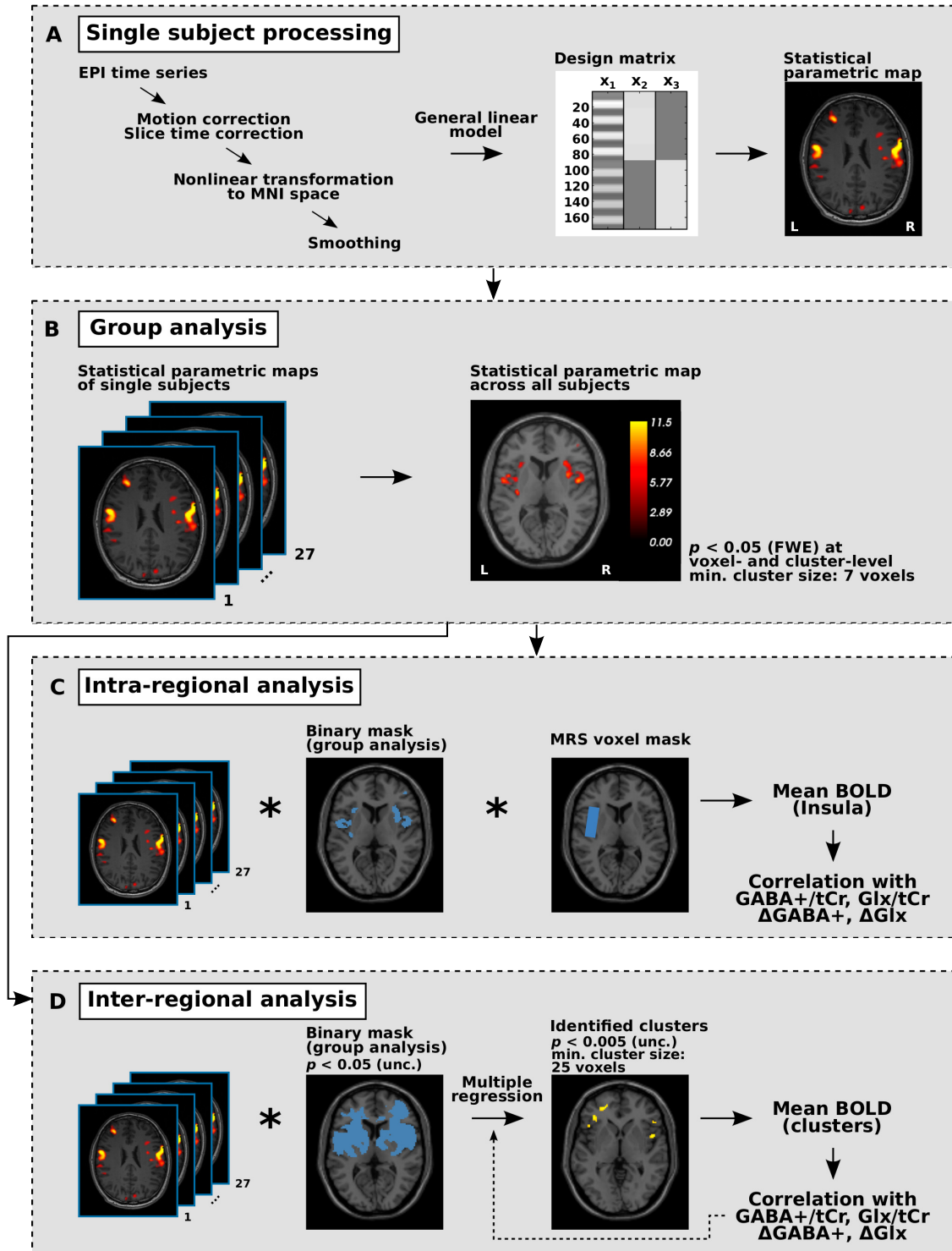


Figure 6.5: Schematic depiction of the processing steps for combined fMRS and fMRI data evaluation. (A) Processing of fMRI data for each single subject. (B) Group analysis across all statistical parametric maps of each subject to identify significant pain associations over the group. (C) Intra-regional analysis between individual insular mean BOLD signal values and the metabolite measures. (D) Inter-regional analysis between whole-brain BOLD data and the metabolite measures by performing multiple regression analysis. See text for detailed description of each processing step.

### 6.3.5 Statistical analysis

The rank sum test ( $p < 0.05$ ) was applied to identify significant pain-induced relative concentration changes of target metabolite median values of all included datasets. Furthermore, Spearman’s rank correlation ( $p < 0.05$ ) was applied to investigate possible intra- and inter-regional associations between pain-induced mean BOLD changes extracted from the significant clusters (as described above) and metabolite resting state levels or relative metabolite concentration changes in the left insular cortex. It should be noted, that in case of the inter-regional investigation the Spearman’s rank correlation coefficient served as additional correlative measure only. Moreover, Spearman’s rank correlation was applied to explore if associations exist between the metabolite measures and the VAS values reported at the end of the experiment.

## 6.4 Results

### 6.4.1 Pain stimulation and data exclusion

Averaged over all participants, the mean stimulation temperature was  $T_{max} = (50.0 \pm 0.9)^\circ\text{C}$ . Pain sensation reported by the volunteers resulted in mean VAS values of  $4.6 \pm 0.6$  and  $5.0 \pm 1.1$  at the beginning and at the end of the experiment, respectively. The higher stimulation temperatures in this study compared to in the previous fMRS study but with comparable reported mean VAS values at the beginning of the stimulation reflect the higher sensitivity of women to pain compared to men. The volunteers reported no or only slight habituation to the applied stimuli during one stimulation block, and increased pain intensity during the second block, which is reflected in the increased mean VAS value after the examination.

The PAIN spectroscopy data of one volunteer had to be excluded from the data pool due to a scanner error during the measurements, as had data of a second volunteer due to poor spectra quality. For another subject, the resting state Glx/tCr ratio was identified as an outlier (single subject Glx/tCr  $> 3 \times (25^{th} - 75^{th})$  interquartile range of the Glx/tCr distribution over all included datasets) leading to exclusion from the subsequent analysis. In the end, 25 datasets for the REF state and 24 for the PAIN state entered the analysis.

### 6.4.2 Functional MRS data

Tissue composition of the MRS voxel in the left insular cortex was consistent across all included subjects, as reflected in the small standard deviations of the mean tissue fractions of GM ( $58.4\% \pm 2.4\%$ ), WM ( $28.3\% \pm 2.6\%$ ) and CSF ( $13.4\% \pm 2.6\%$ ).

The included spectroscopy data had a mean SNR of  $104.1 \pm 11.0$  and mean FWHM of  $(0.047 \pm 0.005)$  ppm ( $(5.8 \pm 0.6)$  Hz) with respect to the NAA peak.

Median values of the GABA+/tCr and Glx/tCr ratios in the REF condition (25<sup>th</sup> and 75<sup>th</sup> percentile in brackets) were 0.38 (0.36, 0.40) and 0.20 (0.19, 0.21), respectively, which is within the same range of metabolite ratios described in Chapter 5 despite different cortical/subcortical areas. Figure 6.6 shows the distributions of  $\Delta$ GABA+ and  $\Delta$ Glx for the PAIN state relative to the REF condition (zero line). With all datasets included, no significant pain-induced changes of GABA+/tCr ( $\Delta$ GABA+ = 0.4% (-3.02%, 9.2%)) or Glx/tCr ( $\Delta$ Glx = 0.1% (-2.7%, 8.5%)) were observed (see boxplots on gray background).

However, intra-individually,  $\Delta$ GABA+ and  $\Delta$ Glx both showed distinct positive as well as negative trends (boxplots on white background in Fig. 6.6 showing the pooled positive and negative percentage concentration changes), where the positive metabolite concentration changes are more prominent compared to the negative changes. This can be also seen from the corresponding median values of the pooled data ( $\Delta$ GABA+: -3.2% vs. 9.2%;  $\Delta$ Glx: -3.1% vs. 8.4%). It should be noted, however, that volunteers revealing positive  $\Delta$ GABA+ did not necessarily show positive  $\Delta$ Glx and vice versa.

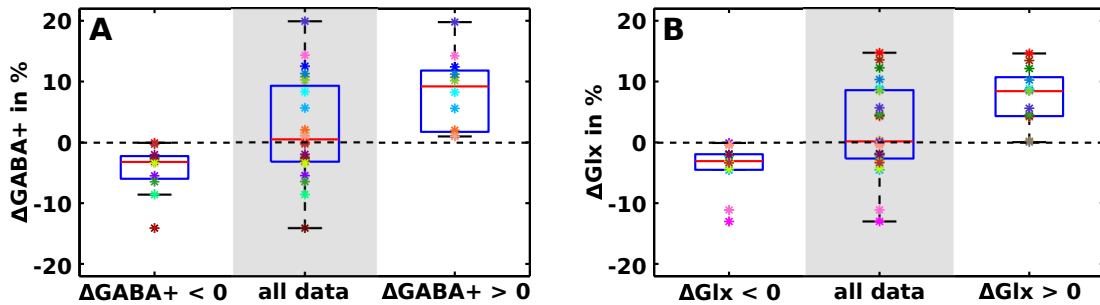


Figure 6.6: Relative concentration changes of (A) GABA+/tCr and (B) Glx/tCr represented in boxplots and normalized to the intra-individual REF state (- -) for each volunteer (marked with different colors of the diagram symbols). The solid red line indicates the median value of the distribution. The lower and upper blue lines of the boxes represent the 25<sup>th</sup> and 75<sup>th</sup> percentile, respectively. The two grey background colored boxplots show the distribution for all data; the boxplots on white background show the distribution for only negative ( $n_{\Delta GABA+<0} = 12$ ,  $n_{\Delta Glx<0} = 11$ ) or positive ( $n_{\Delta GABA+>0} = 12$ ,  $n_{\Delta Glx>0} = 13$ ) intra-individual percentage concentration changes, respectively.

Moreover, a trend towards positive association in terms of Spearman's rank correlation coefficient was identified between  $\Delta$ Glx and the VAS values reported at the end of the experiment ( $R = 0.39$ ,  $p = 0.058$ ). No significant or trend towards correlation between VAS values and insular resting state GABA+/tCr, resting state Glx/tCr or  $\Delta$ GABA+ were observed. The VAS values reported at the beginning of the experiment

were not considered since the individual  $T_{max}$  was chosen at a VAS value of 5 during the pre-test leading to a narrow VAS range between 4 and 6. In contrast, the VAS values reported at the end of the experiment rather reflect the individual perceived pain intensity over the whole experiment.

### 6.4.3 Functional MRI data

Comparing the pain stimulation condition with the baseline, significant BOLD activation ( $p < 0.05$ , voxel- and cluster-level FWE corr.) were detected bilaterally in the insula, in the contra- and ipsi-lateral secondary somatosensory cortex (SII) as well as in the right inferior and middle frontal gyrus (Fig. 6.7). Corresponding MNI coordinates, cluster sizes and T values are summarized in Table 6.2.

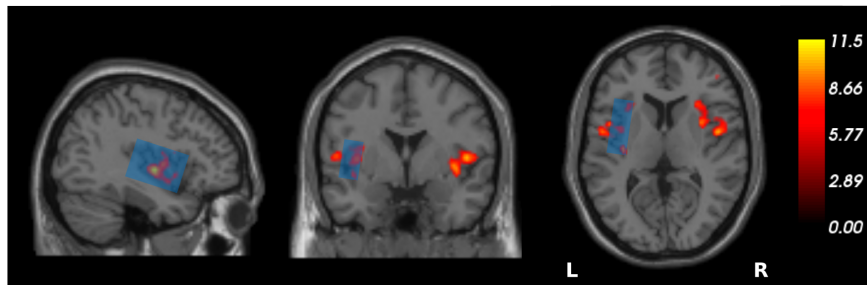


Figure 6.7: Overlay of the MRS voxel placed in the insular cortex (blue) and the statistical map of the group fMRI response to painful stimuli (FWE corrected at the voxel-level and cluster-level with  $p < 0.05$ ) on anatomical images.

Region of activation	Cluster size	MNI coordinate			T value
		x	y	z	
Left insula (BA 13)	481	-44	4	12	11.55
Right insula (BA 13)	979	58	8	2	11.42
Right SII (BA 40)	182	58	-26	22	8.59
Left SII (BA 40)	143	-50	-20	16	8.50
Right inferior frontal gyrus (BA 44)	23	62	10	16	7.82
Right middle frontal gyrus (BA 46)	22	46	44	6	7.54
Left insula (BA 13)	35	-28	20	10	7.43

Table 6.2: Brain regions showing significant ( $p < 0.05$ , voxel- and cluster-level FWE corr.) BOLD activation during acute pain perception. Corresponding Brodmann areas (BA) are given in brackets.

### 6.4.4 Associations between BOLD signal changes and metabolite levels

Intra-regionally, neither resting state GABA+/tCr ( $R = 0.02$ ,  $p = 0.935$ ) nor resting state Glx/tCr ( $R = -0.09$ ,  $p = 0.665$ ) revealed any significant associations with BOLD changes in terms of Spearman’s rank correlation. Also, no significant associations were observed between BOLD and  $\Delta$ GABA+ ( $R = -0.01$ ,  $p = 0.966$ ) or BOLD and  $\Delta$ Glx ( $R = 0.36$ ,  $p = 0.086$ ) in the left insular cortex.

Extending the investigation to whole-brain fMRI for exploring inter-regional interrelations, one cluster in the supplementary motor area with overlap to the mid-cingulate cortex (SMA/MCC) was identified with a significant negative association between the BOLD signal values and the insular resting state GABA+/tCr levels (see Tab. 6.3 and Fig. 6.8). Moreover, BOLD signal changes were positively correlated with pain-induced  $\Delta$ Glx in the left insula in seven further clusters: Left superior frontal gyrus, left and right inferior frontal gyrus, left inferior parietal lobe, left superior temporal gyrus,

Brain regions	Cluster size	MNI coordinate			T value	R	<i>p</i>
		x	y	z			
SMA/MCC (BA 6/24)	129	-10	-20	48	4.65	-0.56	0.004

Table 6.3: Cluster showing a significant negative association between BOLD activation during acute pain perception and resting state GABA+/tCr ( $p < 0.005$  voxel-level uncorrected). Spearman’s rank correlation coefficients  $R$  and  $p$  values were determined by associating inter-individual mean BOLD activations from the identified cluster and corresponding GABA+/tCr values. The corresponding Brodmann areas (BA) are given in brackets.

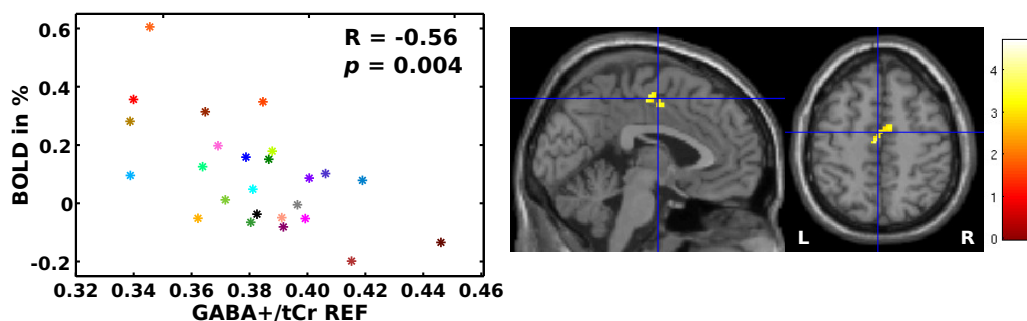


Figure 6.8: Significant negative association in terms of Spearman’s rank correlation between the individual (marked with different colors of the diagram symbols) BOLD responses to pain stimulation in the SMA/MCC region ( $x = -10$ ,  $y = -20$ ,  $z = 48$ ) and resting state GABA+/tCr levels in the left insular cortex, as revealed by multiple regression analysis.

left anterior insula and right posterior insula (see Tab. 6.4). Exemplary correlation plots between the mean BOLD signal values extracted from the left anterior and right posterior insular cortices with  $\Delta\text{Glx}$  in the left insula are depicted in Figure 6.9 A and B, respectively. It should be noted that the identified cluster in the left anterior insula did not overlap with the BOLD volume mask used for the intra-regional analysis (masked with the MRS voxel volume and statistical map of the group fMRI response to painful stimuli).

Brain regions	Cluster size	MNI coordinate			T value	R	<i>p</i>
		x	y	z			
Left superior frontal gyrus (BA 10)	95	-20	48	4	5.23	0.73	< 0.001
Right inferior frontal gyrus (BA 47)	163	50	20	-10	4.90	0.68	< 0.001
Left inferior frontal gyrus (BA 47)	140	-36	24	-16	4.52	0.69	< 0.001
Left inferior parietal lobe (BA 40)	159	-42	-50	52	4.46	0.62	0.002
Left superior temporal gyrus (BA 42)	52	-62	-28	16	4.03	0.59	0.003
Left anterior insula (BA 13)	110	-38	18	6	3.98	0.68	< 0.001
Right posterior insula (BA 13)	30	50	6	0	3.76	0.67	< 0.001

Table 6.4: Clusters showing significant positive associations between BOLD activation during acute pain perception and  $\Delta\text{Glx}$  ( $p < 0.005$  voxel-level uncorrected). Spearman's rank correlation coefficients R and *p* values were determined by associating individual mean BOLD activations from the identified cluster and corresponding  $\Delta\text{Glx}$  values. The corresponding Brodmann areas (BA) are given in brackets.



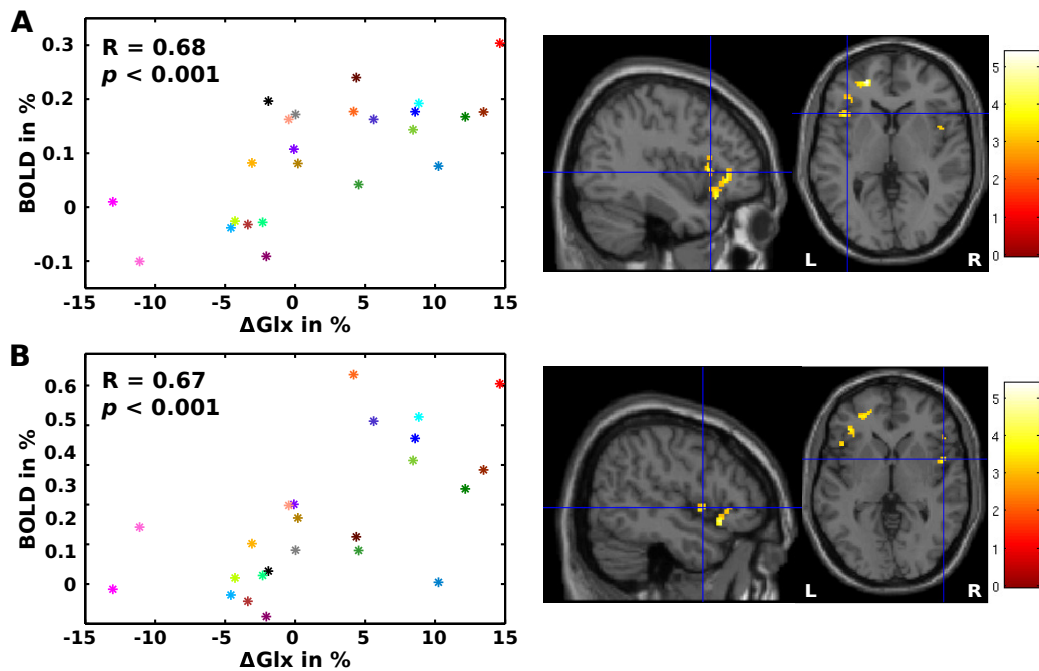


Figure 6.9: Significant positive associations between the BOLD signal in (A) left anterior ( $x = -38$ ,  $y = 18$ ,  $z = 6$ ) and (B) the right posterior insular cortex ( $x = 50$ ,  $y = 6$ ,  $z = 0$ ) and  $\Delta\text{Glx}$  in the left insular cortex.

## 6.5 Discussion

The current chapter describes combined fMRS and fMRI measurements *in vivo*, which were performed at a clinical field strength of 3 T to explore potential intra- and inter-regional associations between acute pain evoked BOLD changes and insular resting state GABA+/tCr and Glx/tCr levels as well as between the BOLD changes and stimulus-induced GABA+ and Glx changes.

Against the expectations, first, no significant pain-induced GABA+ and Glx changes were observed in the insular cortex. Second, intra-regional interrelations between the BOLD changes in the left insula and corresponding metabolite levels or their pain-induced changes were also not found. However and interestingly, significant inter-regional positive associations between BOLD responses in the left superior frontal gyrus, left and right inferior frontal gyrus, left inferior parietal lobe, left superior temporal gyrus, left anterior insula and right posterior insula and insular  $\Delta\text{Glx}$  were observed in this study. Moreover, a significant negative interrelation between BOLD signal changes in the SMA/MCC area and the insular resting state GABA+/tCr levels was identified. These brain regions, which can be ascribed to the network of pain processing brain regions, are known to be activated during pain perception as well as to be involved in the processing of sensory inputs as they occur during heat pain stimulation or to

reveal changes in cortical thickness in the chronic pain state (Apkarian et al., 2005; Caeyenberghs et al., 2017; Jensen et al., 2013; Price, 2000; Symonds, 2006). The positive association between the BOLD response in pain processing brain regions and insular  $\Delta\text{Glx}$  is compatible with the notion that Glx increases during brain activation and that interaction between brain regions is mediated by glutamatergic communication (Duncan et al., 2011). On the other hand, the observed negative interrelation between the BOLD response and GABA+/tCr indicates that the inhibitory tone of GABA in the resting state adjusts the neuronal activity following stimulation not only locally (Duncan et al., 2014) but also within brain networks. Taken together, the observed correlations between insular metabolite levels with BOLD signal changes in the pain network suggests that neurochemical processes within the selected MRS region influence other brain regions through long range projections from excitatory and inhibitory neurons, which should then, in turn, be reflected to a certain degree by the measured GABA+ and Glx values in that region (Duncan et al., 2014). Since  $\Delta\text{Glx}$  shows positive and negative changes (see Fig. 6.6), thus pointing to different directions of activation related processes, it is difficult to provide a clear-cut interpretation of its significant association with predominantly positive BOLD responses. However, since this association was identified in brain regions that are well known to be involved in pain processing, this explorative finding of positive associations between BOLD and  $\Delta\text{Glx}$  (Fig. 6.9) appears at least plausible, but certainly requires more detailed investigations in future studies. Nevertheless, the presented findings indicate inter-regional interactions between neurotransmitter or also energy metabolism turnover levels and stimulus-induced brain activations in the pain processing network. One might argue that the identified clusters were determined by applying a liberal significance threshold of  $p < 0.005$  (voxel-level uncorrected) to the multiple regression analysis. However, since this threshold was combined with correction at cluster-level (see Chapter 2.4.3), the observed associations appear not unreasonable.

The obtained results are supported by a number of studies that have identified inter-regional associations between GABA, Glx and Glu and functional connectivity measured with resting state fMRI within brain networks. Stagg et al. observed an inverse relationship between GABA levels in the motor cortex and the strength of functional connectivity across the resting motor network (Stagg et al., 2014). Wagner et al. identified a negative association of Glx levels in the hippocampus and its functional connectivity along the anterior-posterior axis (Wagner et al., 2016). Moreover, the functional connectivity strength in the DMN revealed a positive correlation with Glu and a negative association with GABA measured in the posteromedial cortex (Kapogiannis et al., 2013). Beyond, task-related BOLD responses were also associated with local

resting state metabolite measures. Falkenberg et al. demonstrated that Glu levels in the ACC predict inter-regional BOLD responses to cognitive control (Falkenberg et al., 2012). Furthermore, Duncan et al. observed an inter-regional glutamatergic mediation of empathy task-induced BOLD signal changes between perigenual and supragenual ACC (Duncan et al., 2011). Summarizing, these findings were interpreted as network excitation-inhibition balances modulating inter-regional synchrony, which may also hold true for the findings of the current study.

In contrast, recent research however also reported a negative intra-regional relation between resting state GABA levels and intra-regional task-induced BOLD responses (Bednařík et al., 2015; Donahue et al., 2010; Muthukumaraswamy et al., 2009, 2012; Stagg et al., 2011a; Violante et al., 2013). The authors of these studies suggested that higher GABA levels in resting state inhibit stimulus related brain activation, leading to a reduced BOLD response. Nevertheless, these findings remain controversial as they were not reproduced, for instance, by Harris et al. (Harris et al., 2015a), who applied several tasks in a multiregional brain study, thus supposing a more complex mechanism of the neurochemical modulation of the neurovascular coupling evoking the BOLD response.

A joint analysis of stimulus-induced GABA and Glu level changes and their associations with BOLD signal changes in the same brain area has so far only been performed in a few studies that applied different stimulation paradigms with contrary outcomes. Bednařík et al. (Bednařík et al., 2015) reported a positive association between Glu concentration changes and the BOLD response in the visual cortex during visual stimulation and ascribed this finding to increased energy demands met by oxidative metabolism. More recently, these outcomes were confirmed by Ip et al. (Ip et al., 2017), who observed a correlation between the time courses of Glu and BOLD signal changes in the same brain region during a visual stimulation paradigm by performing semi-simultaneous fMRI and fMRS measurements. In contrast, Kühn et al. (Kühn et al., 2016) missed an interrelation between determined positive Glu changes and BOLD in the ACC, but observed a negative association between GABA concentration changes and the corresponding BOLD response during a Stroop task suggesting an association between GABA and brain activation dynamics. Moreover, Huang et al. (Huang et al., 2015) found no direct association between positive Glx changes and BOLD in the medial prefrontal cortex during a mental imagery task. However, these studies differ not only in the applied stimuli but also in the explored brain regions that may hamper comparability between the reported findings of intra-regional associations between stimulus-induced metabolite changes and BOLD responses.

Combining the findings of recent previous studies and the current results suggests,

first, that there is obviously no simple relationship between the inhibitory metabolic tone within one brain region (as represented by GABA levels) and its corresponding BOLD response to a stimulus that can be generalized. Moreover, the findings presented here underpin that such an expected relationship must be the result of a far more complex system of brain activity regulating mechanisms, which might be as well influenced by interactions with other brain regions. In addition, identified correlations between metabolite levels and BOLD signal changes seem to be highly dependent on the specific stimulation applied, e.g. sensory, visual or cognitive tasks, and the investigated brain network. All of this certainly warrants further research (Lipp et al., 2015).

One further aim of this study was to investigate pain-induced GABA+ and Glx changes in the insular cortex. Both metabolites showed no unambiguous trends during pain perception, but when dividing  $\Delta$ GABA+ and  $\Delta$ Glx into subgroups revealed larger amplitudes for positive percentage concentration changes compared to negative changes, which will be discussed in the following. Previous fMRS pain studies, including the study described in Chapter 5, did observe an increase of Glx during pain perception (Cleve et al., 2015; Gussew et al., 2010; Gutzeit et al., 2011; Mullins et al., 2005) in the insula, anterior cingulate and occipital cortex, together with a contemporaneous decrease of GABA+ (Cleve et al., 2015). In contrast, Kupers et al. (Kupers et al., 2009) reported an increase of GABA, but no changes of Glu and Glx in the rostral anterior cingulate cortex.

The volunteers reported no or only slight habituation to the presented stimuli over the whole experiment time, which is reflected in the fairly small variation of the VAS values at the beginning compared to the end of the experiment. Nevertheless, distraction is known to lower pain evoked activity (Apkarian et al., 2005) and its effect on temporal metabolic changes remains unclear and may even differ from the subjective volunteers' reports. In a recent fMRS study, Apšvalka et al. (Apšvalka et al., 2015) compared the effects of repetitive visual stimulations with identical and novel pictures on metabolic changes in the left lateral occipital cortex. New, not repeated visual stimuli were associated with a significant Glu increase of 12% compared to the resting state, whereas the repeated presentation of the same pictures was not related to an increase in Glu, but did indeed show a slight trend of Glu decrease of about 2%. Regarding the findings of Apšvalka et al., it can be speculated that volunteers with a positive Glx change perceived a higher pain intensity than the group with negative Glx changes in the study presented here. This assumption is supported by the identified trend towards positive correlation between the reported VAS values and  $\Delta$ Glx. Even if no association was observed between the VAS values and GABA, perhaps, a similar effect exists for GABA explaining then the subdivision in positive and negative changes. Taken together, one

may presume that the partially contrary findings of stimulus-induced metabolite changes are related, on the one hand, to differences in the stimulation paradigm design, and, on the other hand, to the investigation of various brain regions. In particular, the latter is supported by the observed temporal variations of pain-induced BOLD responses in different brain regions during the same heat pain stimulation condition (section 6.2).

Finally, there are some limitations to this study that have to be discussed. As mentioned previously, pain perception relies on a complex interaction of processes that do not remain on a constant level over time due to psychological influences, distraction or physiological habituation effects (Apkarian et al., 2005). In particular, keeping the intensity and sensation of pain stimulation constant over a period of several minutes is difficult to achieve (Greffrath et al., 2007; Hashmi and Davis, 2010). To reduce habituation, first, the MRS measurement time was minimized by applying a block design instead of distinguishing between stimulation and short inter-stimulus states (see Chapter 5.4 and 6.2). Second, the measurement protocol was split into two blocks to allow for recovery from persistent heat pain stimulation, even though expecting an unavoidable partial habituation to the perceived heat pulses. Thus, the experiment setup may still contain some trade-offs, whose effects on the results remain unclear. Shortening the measurement time would be mainly beneficial for investigating pain perception that can be achieved with higher field strengths (Ganji et al., 2014) ( $\geq 7$  T), since GABA can then be resolved without spectral editing sequences and with a higher SNR compared to 3 T. Beyond, semi-simultaneous fMRI and fMRS data acquisition strategies instead of sequential measurements should be further pursued as proposed by Ip et al. (Ip et al., 2017), who measured EPI and MRS data within one acquisition cycle, which enables an improved exploration of associations between the two measures. Third, the GABA+ signal contained resonances from macromolecules. Even though a homogeneous group of male volunteers with a narrow age range was investigated, variability in the macromolecular contribution to the measured GABA signal either due to individual differences or experimental issues (i.e., resulting from frequency drift) cannot be excluded. As discussed in Chapter 2.2.5, macromolecule suppression methods, however, suffer from lower SNR, are more susceptible to experimental errors and require additional technical development (Edden et al., 2016; Harris et al., 2015b). Moreover, it has to be considered that in the current study Glx was measured and that the presented results have thus to be differentiated from studies investigating Glu. As discussed in Chapter 5.4, the compartmentation of Glu into metabolic and neurotransmitter pools impedes the differentiation between the pools' corresponding effects on neuronal activation parameters when determining Glu levels with MRS, since the spectra reflect the sum of all Glu compartments. Over and above, as Gln acts as an intermediate of

glutamatergic neurotransmission and is involved in GABA synthesis - processes, which are both affected by brain activation (Rae, 2014) - reporting the sum intensity Glx introduces an additional uncertainty with respect to expected associations between glutamatergic turnover and neuronal activity measures. Consequently, the inability to identify the exact local or metabolic origin of the measured neurochemical levels represents probably the main limitation in interpreting the spectroscopic and functional results.

# Chapter 7

## Conclusion and Outlook

The main objective of this thesis was to apply an MR spectroscopic technique to detect brain metabolites concentration levels and to explore their possible changes during a stimulation condition. Potential changes of neuronal activity associated metabolites GABA and Glx were investigated in the human brain by using  $^1\text{H}$  MEGA-PRESS spectroscopy while applying acute heat pain stimulation. The question whether acute pain-induced metabolite concentration changes are observable can be positively answered as demonstrated in the conducted fMRS study (Chapter 5), where a decrease of GABA+ and a simultaneous increase of Glx was identified in the anterior cingulate and occipital cortex with subcortical areas that are involved in pain processing. Moreover, the sensitivity to identify differences of GABA and Glx concentrations with MEGA-PRESS spectroscopy was experimentally verified in a phantom study (Chapter 4.2). The ability to monitor metabolite changes during acute pain stimulation is promising and underlines the advantage of using  $^1\text{H}$  MRS for direct and simultaneous assessment of neurochemical processes *in vivo*. Recent  $^1\text{H}$  MRS studies identified permanently decreased GABA concentrations and altered Glu or Glx levels in chronic pain disease compared to healthy controls and were interpreted to indicate impairments in neurochemistry (Harris and Clauw, 2012; Henderson et al., 2013). However, since these measurements were performed under resting state conditions only, they are unable to differentiate between changes solely reflecting disordered neuronal regulations or being also related to degenerative cellular changes. Thus, functional MR spectroscopic studies may provide a deeper insight into altered neurochemical processes mediating neuronal activity as they are supposed to be present in chronic pain disease but also in other brain disorders.

Moreover, by combining functional MR imaging and fMRS (Chapter 6) an interrelation between neuronal activity related variations of blood oxygenation levels in several cerebral nociceptive network nodes and insular resting state GABA+ levels as

well as Glx alterations were identified during perception of acute pain. These findings suggest that brain activity within brain networks in the healthy state is influenced by neurochemical interactions within particular cerebral areas. Thus, regulation of brain function seems to be more complex than just assuming that stimulus-induced local neurochemical processes are directly related to increased energy needs and, in turn, to the amplitude of BOLD signal change in the same brain region.

Furthermore, the difference optimization method to automatically correct phase and frequency differences between mean non-edited and edited  $^1\text{H}$  MEGA-PRESS spectra (Chapter 3) distinctly improved the elimination of subtraction artifacts, which typically hamper the quantitation of GABA+ and Glx in the corresponding difference spectrum. Frequency drifts during data acquisition are of major concern in MRS and, as briefly discussed in Chapter 2.2.5, can severely affect spectroscopy measurements, when aiming to suppress macromolecules to quantify pure GABA instead of GABA+. Being able to quantify GABA without macromolecular contributions would facilitate the identification of pure GABA concentration differences, e.g. between groups of healthy subjects and patients, or of associations between resting state GABA levels and BOLD signal changes. Therefore, implementing prospective correction methods of those drifts during MRS measurements are of current interest in the field of MEGA-PRESS research to allow for more reliable metabolite editing. This is currently realized by interleaved water referencing acquisitions (Edden et al., 2016) that suffer, however, from increased measurement time. Frequency correction based on the previous MR scan, e.g. using the reduced suppressed water or the creatine resonance as reference signal, is also conceivable.

One persisting difficulty in MRS is the assignment of the detected metabolite intensities or their stimulus-induced changes to particular physiological pools, such as neurotransmitter turnover or energy metabolism. As presented in Chapter 4.1, the composite measure of glutamate and glutamine (Glx) cannot be separated when applying MEGA-PRESS at 3 T, which introduces further ambiguities to spectroscopic results. Separate detection of resolved GABA, Glu and Gln resonances with 1D measurement techniques currently requires ultra-high magnetic field strengths of 7 T or higher. One more sophisticated approach to effectively separate neurotransmitter and metabolic turnover relies on dynamic acquisitions of  $^{13}\text{C}$  MR spectra series with a selected labeled substance, often glucose, that is continuously administrated *in vivo* (Rothman et al., 2011). The labeled carbons of the energy supplier glucose first enter the TCA cycle (energy metabolism compartment), and are subsequently transferred to the neurotransmitter pool due to interaction with the Glu-Gln cycle and the related GABA synthesis. Thus, turnover rates of energy metabolism and neurotransmitter cycle



can be recalculated from the dynamic  $^{13}\text{C}$  MR measurements by applying appropriate mathematical models. However,  $^{13}\text{C}$  MRS experiments are experimentally challenging and further technical improvements are required to improve sensitivity, e.g. by using hyperpolarization, before  $^{13}\text{C}$  MR becomes a routine tool for human applications (Rothman et al., 2011).

One further limitation of single-voxel MRS experiments *in vivo* concerns the restriction to only a few brain regions. However, as inter-regional associations between GABA+, Glx alterations and BOLD signal changes were observed in the combined fMRS and fMRI study, functional MRS measurements covering multiple voxels or preferably the whole brain would improve distinctly our understanding of physiological interrelations within brain networks. This can currently be achieved by incorporating the editing approaches into 3D MR spectroscopic imaging sequences (MRSI). However, in contrast to single-voxel measurements, MRSI requires more challenging shimming techniques to ensure sufficient field homogeneity over the whole brain and further needs reliable correction of frequency changes due to subject motion during prolonged acquisition times. One promising solution was proposed by Bogner et al. (2014) who combined 3D MEGA-editing MRS imaging with a real-time motion correction and shim update to overcome these issues. Hence, whole-brain GABA measurements can be realized with a spatial resolution up to  $1\text{ cm}^3$  but comparably long measurement times of 24 min. Moreover, very recently, Oeltzschner et al. (2016) developed a dual-volume excitation approach with J-difference editing that enables simultaneous acquisition of GABA spectra from two voxels while keeping the acquisition time the same as for single-voxel measurements. However, the location and orientation of the investigated voxels are restricted to the direction of the slice-selective gradient due to the dual-band slice-selective excitation and limits the measurements, for instance, to homologous right and left or anterior and posterior brain regions. Nonetheless, the recent advances in GABA MRS acquisition strategies of multiple voxels are promising to realize whole-brain or multi-voxel investigations of the excitation-inhibition balance in the near future.

To conclude, MRS is a powerful tool to explore the neurochemical processes regulating brain activity. In particular, the J-editing approach offers an elegant opportunity to access brain metabolites of low concentration at moderate magnetic field strengths. To round off the advances in MR spectroscopy, a new editing scheme shall be briefly described since J-difference editing can also applied to access further brain substances of clinical relevance, such as e.g. glutathione, the main antioxidant in the human brain. To overcome the limitation of MEGA-PRESS of separate MRS experiments, Chan et al. (2016) introduced lately a very promising MRS approach dubbed HERMES (Hadamard Encoding and Reconstruction of Mega-Edited Spectroscopy) that applies J-editing to

various low concentration resonances to observe e.g. the isolated resonances of GABA+ and glutathione at the same time (Saleh et al., 2016). To this end, not only a pair of ED and NED spectra is acquired but rather a series of multiple subspectra fulfilling the ED and NED condition for either GABA+ (editing at 1.9 ppm), glutathione (editing at 4.6 ppm), both or none of them, so that a difference spectrum for each, GABA+ and glutathione, can be separately calculated by appropriate combination of the multiple ED and NED subspectra. Nonetheless, this approach requires that at least one resonance of each metabolite of interest does not overlap with the other to allow for independent editing. Moreover, a compromise has to be found between the optimal echo times for the detection of each selected metabolite, since the echo time for optimal editing of the metabolite of interest is preset by the molecule specific coupling constant  $J$  (Saleh et al., 2016). Despite these limitations the current progress in this research area is encouraging and further advances will be made to reliably assess multiple key metabolites in the human brain in the near future, which is promising for applications in cognitive and clinical neuroscience.

Finally, some difficulties and limitations of realizing and performing pain stimulation experiments shall be discussed that turned up during the progression of the presented studies. Pain perception serves as an important sign of danger and commonly induces protective reactions of the human body to prevent tissue damage. However, those reactions are different across individuals depending on a variety of factors, including previous experiences with pain perception, attentional or emotional state during the experiment, habituation to the presented stimuli and related anticipation (Apkarian et al., 2005). Further, experiment conditions can have different effects on each individual, such as the experiment environment, experimenter and given instructions, that cannot be controlled for, even if all investigated volunteers are instructed with the same routine. All these effects may blur neuronal activation and the related spectroscopic and fMRI measures. Moreover, since the combined fMRS and fMRI measurements were conducted in a serial manner, differences in an individual's perception state might have occurred during the two measurements, and might have influenced identification of further existing associations that did not exceed the significance threshold in this study. However, the latter limitation could be overcome by applying a combined fMRI-MRS sequence as very recently described by Ip et al. (Ip et al., 2017), who acquired whole-brain fMRI and single-voxel MRS data in semi-simultaneous fashion. Nonetheless, further improvements of the stimulation design would be advantageous to allow more similar stimulation conditions for each subject, and thus, more specific assignments of the observed effects. Controlling for equal states of pain perception for each volunteer is difficult but might be achieved by more narrow volunteer screening, e.g. besides considering gender, age

and handedness, also querying psychological aspects, or introducing a task during the pain experiment, such as continuous rating of pain intensity, to control for the volunteer's attention. However, volunteer interaction during the experiment may also lead to an ambiguity to the determined measures. Nonetheless, habituation to the prolonged heat pain stimulation might efficiently be reduced by shorting of the required measurement time that can be realized by conducting the experiments without time consuming spectral editing at higher field strengths.

# Bibliography

- Apkarian, A. V., Bushnell, M. C., Treede, R.-D., and Zubieta, J.-K. (2005). Human brain mechanisms of pain perception and regulation in health and disease. *European Journal of Pain*, 9(4):463–463.
- Apšvalka, D., Gadie, A., Clemence, M., and Mullins, P. G. (2015). Event-related dynamics of glutamate and BOLD effects measured using functional magnetic resonance spectroscopy (fMRS) at 3T in a repetition suppression paradigm. *NeuroImage*, 118(8):292–300.
- Ashburner, J. and Friston, K. (1997). The role of registration and spatial normalization in detecting activations in functional imaging. *Clinical MRI/Developments in MR*, 7(1):26–28.
- Bartley, E. J. and Fillingim, R. B. (2013). Sex differences in pain: A brief review of clinical and experimental findings. *British Journal of Anaesthesia*, 111(1):52–58.
- Bednařík, P., Tkáč, I., Giove, F., DiNuzzo, M., Deelchand, D. K., Emir, U. E., Eberly, L. E., and Mangia, S. (2015). Neurochemical and BOLD responses during neuronal activation measured in the human visual cortex at 7 Tesla. *Journal of Cerebral Blood Flow & Metabolism*, 35(4):601–610.
- Bender, R. and Lange, S. (2001). Adjusting for multiple testing - When and how? *Journal of Clinical Epidemiology*, 54(4):343–349.
- Berkley, K. J. (1997). Sex differences in pain. *Behavioral and Brain Sciences*, 20(3):371380.
- Blamire, A. M., Ogawa, S., Ugurbil, K., Rothman, D., McCarthy, G., Ellermann, J. M., Hyder, F., Rattner, Z., and Shulman, R. G. (1992). Dynamic mapping of the human visual cortex by high-speed magnetic resonance imaging. *Proceedings of the National Academy of Sciences of the United States of America*, 89(22):11069–11073.
- Bloch, F., Hansen, W. W., and Packard, M. (1946). The nuclear induction experiment. *Physical Review*, 70:474–485.

- Bogner, W., Gagoski, B., Hess, A. T., Bhat, H., Tisdall, M. D., van der Kouwe, A. J., Strasser, B., Marjańska, M., Tractnig, S., Grant, E., Rosen, B., and Andronesi, O. C. (2014). 3D GABA imaging with real-time motion correction, shim update and reacquisition of adiabatic spiral MRSI. *NeuroImage*, 103:290–302.
- Bogner, W., Gruber, S., Doelken, M., Stadlbauer, a., Ganslandt, O., Boettcher, U., Tractnig, S., Doerfler, a., Stefan, H., and Hammen, T. (2010). In vivo quantification of intracerebral GABA by single-voxel 1H-MRS-How reproducible are the results? *European Journal of Radiology*, 73(3):526–531.
- Borsook, D., Moulton, E. a., Schmidt, K. F., and Becerra, L. R. (2007). Neuroimaging revolutionizes therapeutic approaches to chronic pain. *Molecular Pain*, 3(ii):25.
- Brown, R., Cheng, Y.-C. N., Haacke, E., Thompson, M., and R., V. (2014). *Magnetic Resonance Imaging - Physical Principles and Sequence Design, Second Edition*. John Wiley & Sons, Inc.
- Caeyenberghs, K., Pijnenburg, M., Goossens, N., Janssens, L., and Brumagne, S. (2017). Associations between Measures of Structural Morphometry and Sensorimotor Performance in Individuals with Nonspecific Low Back Pain. *American Journal of Neuroradiology*, 38(1):183–191.
- Cavanna, A. E. and Trimble, M. R. (2006). The precuneus: a review of its functional anatomy and behavioural correlates. *Brain*, 129(3):564–83.
- Chan, K. L., Puts, N. A. J., Schär, M., Barker, P. B., and Edden, R. A. E. (2016). HERMES: Hadamard encoding and reconstruction of MEGA-edited spectroscopy. *Magnetic Resonance in Medicine*, 76(1):11–19.
- Choi, C., Ganji, S. K., DeBerardinis, R. J., Hatanpaa, K. J., Rakheja, D., Kovacs, Z., Yang, X.-L., Mashimo, T., Raisanen, J. M., Marin-Valencia, I., Pascual, J. M., Madden, C. J., Mickey, B. E., Malloy, C. R., Bachoo, R. M., and Maher, E. A. (2012). 2-hydroxyglutarate detection by magnetic resonance spectroscopy in IDH-mutated patients with gliomas. *Nature Medicine*, 18(4):624–9.
- Choi, C., Patel, A., Douglas, D., and Dimitrov, I. (2010). Measurement of proton T2 of coupled-spin metabolites in gray and white matter in human brain at 3T. In *Proceedings of the International Society for Magnetic Resonance in Medicine*, volume 18, #3331, Stockholm.
- Cleve, M., Gussew, A., and Reichenbach, J. R. (2013). In vivo measurements of acute pain induced changes of GABA and Glx with functional 1H MEGA-PRESS MR

- spectroscopy. In *Cardiff International Symposium on MR Spectroscopy of GABA*, volume 2, #28, Cardiff, Wales, UK.
- Cleve, M., Gussew, A., and Reichenbach, J. R. (2014a). In vivo measurements of acute pain induced changes of GABA+ and Glx in the brain with functional 1H-MEGA-PRESS MR spectroscopy. In *Proceedings of the International Society for Magnetic Resonance in Medicine*, volume 22, #485, Milan, Italy.
- Cleve, M., Gussew, A., and Reichenbach, J. R. (2014b). In vivo Nachweis akuteschmerzinduzierter Veränderungen von GABA+ und Glx im menschlichen Gehirn mit funktioneller 1H-MEGA-PRESS MR Spektroskopie. In *Proceedings of the German Chapter of the International Society for Magnetic Resonance in Medicine*, volume 17, #4, Jena, Germany.
- Cleve, M., Gussew, A., and Reichenbach, J. R. (2015). In vivo detection of acute pain-induced changes of GABA+ and Glx in the human brain by using functional 1H MEGA-PRESS MR spectroscopy. *NeuroImage*, 105:67–75.
- Cleve, M., Gussew, A., and Reichenbach, J. R. (2016a). BOLD-fMRI signal changes during prolonged heat pain stimulation. In *Proceedings of the International Society for Magnetic Resonance in Medicine*, volume 24, #1736, Singapore.
- Cleve, M., Gussew, A., Wagner, G., Bär, K.-J., and Reichenbach, J. R. (2017a). Assessment of intra- and inter-regional interrelations between GABA+, Glx and BOLD during pain perception in the human brain - A combined <sup>1</sup>H fMRS and fMRI study. *Neuroscience*, revision in progress (15.07.2017).
- Cleve, M., Gussew, A., Wagner, G., and Reichenbach, J. R. (2017b). Interregional associations between GABA+, Glx and BOLD contrast changes during acute pain perception in the human brain - A combined 1H fMRS and fMRI study. In *Proceedings of the International Society for Magnetic Resonance in Medicine*, volume 25, #5633, Honolulu, HI, USA.
- Cleve, M., Krämer, M., Gussew, A., and Reichenbach, J. R. (2016b). Automatic correction of relative frequency and phase for 1H MEGA-PRESS spectra. In *Proceedings of the German Chapter of the International Society for Magnetic Resonance in Medicine*, volume 19, #7, Würzburg, Germany.
- Cleve, M., Krämer, M., Gussew, A., and Reichenbach, J. R. (2017c). Difference optimization: Automatic correction of relative frequency and phase for 1H MEGA-PRESS spectra. In *Proceedings of the International Society for Magnetic Resonance in Medicine*, volume 25, #2997, Honolulu, HI, USA.

- Cleve, M., Krämer, M., Gussew, A., and Reichenbach, J. R. (2017d). Difference optimization: Automatic correction of relative frequency and phase for mean non-edited and edited GABA  $^1\text{H}$  MEGA-PRESS spectra. *Journal of Magnetic Resonance*, 279:16–21.
- Corbett, R. J., Laptook, A. R., Tollefsbol, G., and Kim, B. (1995). Validation of a noninvasive method to measure brain temperature in vivo using  $^1\text{H}$  NMR spectroscopy. *Journal of Neurochemistry*, 64(3):1224–30.
- Craven, A. R., Grüner, R., Ersland, L., Dwyer, G. E., Brix, M. K., and Hugdahl, K. (2014). Optimal scan time for reproducible GABA measurements. In *Proceedings of the International Society for Magnetic Resonance in Medicine*, volume 22, #2910, Milan, Italy.
- Dale, A. and Buckner, R. (1997). Selective Averaging of Rapidly Presented Individual Trials Using fMRI. *Human Brain Mapping*, 5(5):329–340.
- de Graaf, R. A. (2007). *In vivo NMR Spectroscopy: Principles and Techniques*. John Wiley & Sohns, Ltd, 2 edition.
- Defrin, R., Shachal-Shiffer, M., Hadgadg, M., and Peretz, C. (2006). Quantitative somatosensory testing of warm and heat-pain thresholds: the effect of body region and testing method. *The Clinical Journal of Pain*, 22(2):130–6.
- Dickinson, W. C. (1950). Dependence of the  $\text{F}^{19}$  Nuclear Resonance Position on Chemical Compound. *Physical Review*, 77:736–737.
- Donahue, M. J., Near, J., Blicher, J. U., and Jezard, P. (2010). Baseline GABA concentration and fMRI response. *NeuroImage*, 53(2):392–398.
- Duncan, N. W., Enzi, B., Wiebking, C., and Northoff, G. (2011). Involvement of glutamate in rest-stimulus interaction between perigenual and supragenual anterior cingulate cortex: A combined fMRI-MRS study. *Human Brain Mapping*, 32(12):2172–2182.
- Duncan, N. W., Wiebking, C., and Northoff, G. (2014). Associations of regional GABA and glutamate with intrinsic and extrinsic neural activity in humans A review of multimodal imaging studies. *Neuroscience and Biobehavioral Reviews*, 47:36–52.
- Edden, R. A. E., Intrapromkul, J., Zhu, H., Cheng, Y., and Barker, P. B. (2012a). Measuring T2 in vivo with J-difference editing: application to GABA at 3 Tesla. *Journal of Magnetic Resonance Imaging*, 35(1):229–34.

- Edden, R. A. E., Oeltzschner, G., Harris, A. D., Puts, N. A. J., Chan, K. L., Boer, V. O., Schär, M., and Barker, P. B. (2016). Prospective frequency correction for macromolecule-suppressed GABA Editing at 3T. *Journal of Magnetic Resonance Imaging*, 44:1474–1482.
- Edden, R. A. E., Pomper, M. G., and Barker, P. B. (2007). In vivo differentiation of N-acetyl aspartyl glutamate from N-acetyl aspartate at 3 Tesla. *Magnetic Resonance in Medicine*, 57(6):977–82.
- Edden, R. A. E., Puts, N. A. J., and Barker, P. B. (2012b). Macromolecule-suppressed GABA-edited magnetic resonance spectroscopy at 3T. *Magnetic Resonance in Medicine*, 68(3):657–661.
- Eklund, A., Nichols, T. E., and Knutsson, H. (2016). Cluster failure: Why fMRI inferences for spatial extent have inflated false-positive rates. *Proceedings of the National Academy of Sciences of the United States of America*, 113(28):7900–5.
- Evans, A. C., Collins, D. L., Mills, S. R., Brown, E. D., Kelly, R. L., and Peters, T. M. (1993). 3D statistical neuroanatomical models from 305 MRI volumes. In *1993 IEEE Conference Record Nuclear Science Symposium and Medical Imaging Conference*, pages 1813–1817 vol.3.
- Evans, C. J., Puts, N. A. J., Robson, S. E., Boy, F., McGonigle, D. J., Sumner, P., Singh, K. D., and Edden, R. A. E. (2013). Subtraction artifacts and frequency (Mis-)alignment in J-difference GABA Editing. *Journal of Magnetic Resonance Imaging*, 38(4):970–975.
- Falkenberg, L. E., Westerhausen, R., Specht, K., and Hugdahl, K. (2012). Resting-state glutamate level in the anterior cingulate predicts blood-oxygen level-dependent response to cognitive control. *Proceedings of the National Academy of Sciences of the United States of America*, 109(13):5069–73.
- Fermi, E. (1930). Über die magnetischen Momente der Atomkerne. *Zeitschrift für Physik*, 60(5):320–333.
- Fields, H. L., Heinricher, M. M., and Mason, P. (1991). Neurotransmitters in Nociceptive Modulatory Circuits. *Annual Review of Neuroscience*, 14(1):219–245.
- Friston, K., Holmes, A., Poline, J.-B., Price, C., and Frith, C. (1996). Detecting Activations in PET and fMRI: Levels of Inference and Power. *NeuroImage*, 4(3):223–235.



- Fruhstorfer, H., Lindblom, U., and Schmidt, W. C. (1976). Method for quantitative estimation of thermal thresholds in patients. *Journal of Neurology, Neurosurgery & Psychiatry*, 39(11):1071–1075.
- Ganji, S. K., An, Z., Banerjee, A., Madan, A., Hulsey, K. M., and Choi, C. (2014). Measurement of regional variation of GABA in the human brain by optimized point-resolved spectroscopy at 7 T in vivo. *NMR in Biomedicine*, 27(10):1167–1175.
- Gasparovic, C., Song, T., Devier, D., Bockholt, H. J., Caprihan, A., Mullins, P. G., Posse, S., Jung, R. E., and Morrison, L. a. (2006). Use of tissue water as a concentration reference for proton spectroscopic imaging. *Magnetic Resonance in Medicine*, 55(6):1219–26.
- Govindaraju, V., Young, K., and Maudsley, A. A. (2000). Proton NMR chemical shifts and coupling constants for brain metabolites. *NMR in Biomedicine*, 13(3):129–53.
- Greffrath, W., Baumgärtner, U., and Treede, R.-D. (2007). Peripheral and central components of habituation of heat pain perception and evoked potentials in humans. *Pain*, 132(3):301–11.
- Grill-Spector, K., Henson, R., and Martin, A. (2006). Repetition and the brain: Neural models of stimulus-specific effects. *Trends in Cognitive Sciences*, 10(1):14–23.
- Griswold, M. A., Jakob, P. M., Heidemann, R. M., Nittka, M., Jellus, V., Wang, J., Kiefer, B., and Haase, A. (2002). Generalized autocalibrating partially parallel acquisitions (GRAPPA). *Magnetic Resonance in Medicine*, 47(6):1202–1210.
- Gussew, A., Erdtel, M., Hiepe, P., Rzanny, R., and Reichenbach, J. R. (2012). Absolute quantitation of brain metabolites with respect to heterogeneous tissue compositions in (1)H-MR spectroscopic volumes. *Magnetic Resonance Materials in Physics, Biology and Medicine*, 25(5):321–33.
- Gussew, A., Rzanny, R., Erdtel, M., Scholle, H. C., Kaiser, W. A., Mentzel, H. J., and Reichenbach, J. R. (2010). Time-resolved functional 1H MR spectroscopic detection of glutamate concentration changes in the brain during acute heat pain stimulation. *NeuroImage*, 49(2):1895–1902.
- Gussew, A., Rzanny, R., Güllmar, D., Scholle, H.-C., and Reichenbach, J. R. (2011). <sup>1</sup>H-MR spectroscopic detection of metabolic changes in pain processing brain regions in the presence of non-specific chronic low back pain. *NeuroImage*, 54(2):1315–23.

- Gutzeit, A., Meier, D., Meier, M. L., von Weymarn, C., Ettlin, D. a., Graf, N., Froehlich, J. M., Binkert, C. a., and Brügger, M. (2011). Insula-specific responses induced by dental pain. A proton magnetic resonance spectroscopy study. *European Radiology*, 21(4):807–15.
- Hahn, E. L. (1950). Spin Echoes. *Physical Review*, 80:580–594.
- Harris, A. D., Glaubit, B., Near, J., Evans, J. C., Puts, N. A. J., Schmidt-Wilcke, T., Tegenthoff, M., Barker, P. B., and Edden, R. A. E. (2014). Impact of frequency drift on gamma-aminobutyric acid-edited MR spectroscopy. *Magnetic Resonance in Medicine*, 72(4):941–8.
- Harris, A. D., Puts, N. A. J., Anderson, B. A., Yantis, S., Pekar, J. J., Barker, P. B., and Edden, R. A. E. (2015a). Multi-Regional Investigation of the Relationship between Functional MRI Blood Oxygenation Level Dependent (BOLD) Activation and GABA Concentration. *PLOS ONE*, 10(2):e0117531.
- Harris, A. D., Puts, N. A. J., Barker, P. B., and Edden, R. A. E. (2015b). Spectral-editing measurements of GABA in the human brain with and without macromolecule suppression. *Magnetic Resonance in Medicine*, 74(6):1523–1529.
- Harris, A. D., Saleh, M. G., and Edden, R. A. E. (2017). Edited 1H magnetic resonance spectroscopy in vivo: Methods and metabolites. *Magnetic Resonance in Medicine*, 77(4):1377–1389.
- Harris, R. E. and Clauw, D. J. (2012). Imaging central neurochemical alterations in chronic pain with proton magnetic resonance spectroscopy. *Neuroscience Letters*, 520(2):192–196.
- Hashmi, J. a. and Davis, K. D. (2009). Women experience greater heat pain adaptation and habituation than men. *Pain*, 145(3):350–357.
- Hashmi, J. A. and Davis, K. D. (2010). Effects of temperature on heat pain adaptation and habituation in men and women. *Pain*, 151(3):737–743.
- Hasler, G., van der Veen, J. W., Grillon, C., Drevets, W. C., and Shen, J. (2010). Effect of Acute Psychological Stress on Prefrontal GABA Concentration Determined by Proton Magnetic Resonance Spectroscopy. *American Journal of Psychiatry*, 167(10):1226–1231.
- Henderson, L. A., Peck, C. C., Petersen, E. T., Rae, C. D., Youssef, A. M., Reeves, J. M., Wilcox, S. L., Akhter, R., Murray, G. M., and Gustin, S. M. (2013). Chronic Pain: Lost Inhibition? *Journal of Neuroscience*, 33(17):7574–7582.

- Henry, M. E., Lauriat, T. L., Shanahan, M., Renshaw, P. F., and Jensen, J. E. (2011). Accuracy and stability of measuring GABA, glutamate, and glutamine by proton magnetic resonance spectroscopy: a phantom study at 4 Tesla. *Journal of Magnetic Resonance*, 208(2):210–8.
- Henry, P. G., Dautry, C., Hantraye, P., and Bloch, G. (2001). Brain GABA editing without macromolecule contamination. *Magnetic Resonance in Medicine*, 45(3):517–520.
- Hindman, J. C. (1966). Proton Resonance Shift of Water in the Gas and Liquid States. *Journal of Chemical Physics*, 44(12):4582.
- Huang, Z., Davis Iv, H. H., Yue, Q., Wiebking, C., Duncan, N. W., Zhang, J., Wagner, N.-F., Wolff, A., and Northoff, G. (2015). Increase in glutamate/glutamine concentration in the medial prefrontal cortex during mental imagery: A combined functional mrs and fMRI study. *Human Brain Mapping*, 36(8):3204–3212.
- Huttenlocher, P. R. (1979). Synaptic density in human frontal cortex developmental changes and effects of aging. *Brain Research*, 163(2):195 – 205.
- Ip, I. B., Berrington, A., Hess, A. T., Parker, A. J., Emir, U. E., and Bridge, H. (2017). Combined fMRI-MRS acquires simultaneous glutamate and BOLD-fMRI signals in the human brain. *NeuroImage*, 155:113–119.
- Jansen, J. F. A., Backes, W. H., Nicolay, K., and Kooi, M. E. (2006). <sup>1</sup>H MR spectroscopy of the brain: absolute quantification of metabolites. *Radiology*, 240(2):318–332.
- Jasmin, L., Rabkin, S. D., Granato, A., Boudah, A., and Ohara, P. T. (2003). Analgesia and hyperalgesia from GABA-mediated modulation of the cerebral cortex. *Nature*, 424(6946):316–320.
- Jensen, K. B., Srinivasan, P., Spaeth, R., Tan, Y., Kosek, E., Petzke, F., Carville, S., Fransson, P., Marcus, H., Williams, S. C. R., Choy, E., Vitton, O., Gracely, R., Ingvar, M., and Kong, J. (2013). Overlapping Structural and Functional Brain Changes in Patients With Long-Term Exposure to Fibromyalgia Pain. *Arthritis & Rheumatism*, 65(12):3293–3303.
- Kapogiannis, D., Reiter, D. A., Willette, A. A., and Mattson, M. P. (2013). Postero-medial cortex glutamate and GABA predict intrinsic functional connectivity of the default mode network. *NeuroImage*, 64:112–9.

- King, S., Chambers, C., and Huguet, A. (2011). The epidemiology of chronic pain in children and adolescents revisited: a systematic review. *Pain*, 152(12):2729–38.
- Klose, U. (1990). In vivo proton spectroscopy in presence of eddy currents. *Magnetic Resonance in Medicine*, 14(1):26–30.
- Kreis, R. (2004). Issues of spectral quality in clinical  $^1\text{H}$ -magnetic resonance spectroscopy and a gallery of artifacts. *NMR in Biomedicine*, 17(6):361–81.
- Kühn, S., Schubert, F., Mекle, R., Wenger, E., Ittermann, B., Lindenberger, U., and Gallinat, J. (2016). Neurotransmitter changes during interference task in anterior cingulate cortex: evidence from fMRI-guided functional MRS at 3 T. *Brain Structure and Function*, 221(5):2541–2551.
- Kupers, R., Danielsen, E., and Kehlet, H. (2009). Painful tonic heat stimulation induces GABA accumulation in the prefrontal cortex in man. *Pain*, 142(1-2):89–93.
- Lagarias, J. C., Reeds, J. A., Wright, M. H., and Wright, P. E. (1998). Convergence Properties of the Nelder–Mead Simplex Method in Low Dimensions. *SIAM Journal on Optimization*, 9(1):112–147.
- LaGraize, S. C. and Fuchs, P. N. (2007). GABA<sub>A</sub> but not GABA<sub>B</sub> receptors in the rostral anterior cingulate cortex selectively modulate pain-induced escape/avoidance behavior. *Experimental Neurology*, 204(1):182–194.
- Lauterbur, P. C. (1973). Image Formation by Induced Local Interactions: Examples Employing Nuclear Magnetic Resonance. *Nature*, 242:190–191.
- Lenz, E. (1834). Ueber die Bestimmung der Richtung der durch elektrodynamische Vertheilung erregten galvanischen Ströme. *Annalen der Physik*, 107(31):483–494.
- Levitt, M. H. (2008). *Spin Dynamics - Basics of Nuclear Magnetic Resonance, Second Edition*. John Wiley & Sons, Inc.
- Lieberman, M. D. and Cunningham, W. A. (2009). Type I and Type II error concerns in fMRI research: re-balancing the scale. *Social Cognitive and Affective Neuroscience*, 4(4):423–428.
- Lipp, I., Evans, C. J., Lewis, C., Murphy, K., Wise, R. G., and Caseras, X. (2015). The relationship between fearfulness, GABA+, and fear-related BOLD responses in the insula. *PLoS ONE*, 10(3):1–18.

- Logothetis, N. (2008). What we can do and what we cannot do with fMRI. *Nature*, 453(7197):869–78.
- Mader, I., Seeger, U., Karitzky, J., Erb, M., Schick, F., and Klose, U. (2002). Proton magnetic resonance spectroscopy with metabolite nulling reveals regional differences of macromolecules in normal human brain. *Journal of Magnetic Resonance Imaging*, 16(5):538–46.
- Maleki, N., Brawn, J., Barmettler, G., Borsook, D., and Becerra, L. (2013). Pain response measured with arterial spin labeling. *NMR in Biomedicine*, 26(6):664–73.
- Mangia, S., Giove, F., and Dinuzzo, M. (2012). Metabolic pathways and activity-dependent modulation of glutamate concentration in the human brain. *Neurochemical Research*, 37(11):2554–61.
- Mangia, S., Giove, F., Tkáč, I., Logothetis, N. K., Henry, P.-G., Olman, C. A., Maraviglia, B., Di Salle, F., and Uurbil, K. (2009). Metabolic and Hemodynamic Events after Changes in Neuronal Activity: Current Hypotheses, Theoretical Predictions and in vivo NMR Experimental Findings. *Journal of Cerebral Blood Flow & Metabolism*, 29(3):441–463.
- Mangia, S., Tkáč, I., Gruetter, R., Van de Moortele, P.-F., Maraviglia, B., and Uurbil, K. (2007). Sustained neuronal activation raises oxidative metabolism to a new steady-state level: evidence from  $^1\text{H}$  NMR spectroscopy in the human visual cortex. *Journal of Cerebral Blood Flow & Metabolism*, 27(5):1055–63.
- Mansfield, P. (1977). Multi-planar image formation using NMR spin echoes. *Journal of Physics C: Solid State Physics*, 10(3):L55.
- Mansfield, P. and Grannell, P. K. (1973). NMR 'diffraction' in solids? *Journal of Physics C: Solid State Physics*, 6(22):L422–L426.
- Mayer, D. and Spielman, D. M. (2005). Detection of glutamate in the human brain at 3 T using optimized constant time point resolved spectroscopy. *Magnetic Resonance in Medicine*, 54(2):439–442.
- Mescher, M., Merkle, H., Kirsch, J., Garwood, M., and Gruetter, R. (1998). Simultaneous in vivo spectral editing and water suppression. *NMR in Biomedicine*, 11(6):266–272.
- Minassian, A. T., Ricalens, E., Humbert, S., Duc, F., Aubé, C., and Beydon, L. (2013). Dissociating anticipation from perception: Acute pain activates default mode network. *Human Brain Mapping*, 34(9):2228–43.

- Mlynárik, V., Gruber, S., and Moser, E. (2001). Proton T (1) and T (2) relaxation times of human brain metabolites at 3 Tesla. *NMR in Biomedicine*, 14(5):325–31.
- Mullins, P. G., Chen, H., Xu, J., Caprihan, A., and Gasparovic, C. (2008). Comparative reliability of proton spectroscopy techniques designed to improve detection of J-coupled metabolites. *Magnetic Resonance in Medicine*, 60(4):964–969.
- Mullins, P. G., McGonigle, D. J., O’Gorman, R. L., Puts, N. A. J., Vidyasagar, R., Evans, C. J., Edden, R. A. E., Brookes, M. J., Garcia, A., Foerster, B. R., Petrou, M., Price, D., Solanky, B. S., Violante, I. R., Williams, S., and Wilson, M. (2014). Current practice in the use of MEGA-PRESS spectroscopy for the detection of GABA. *NeuroImage*, 86:43–52.
- Mullins, P. G., Rowland, L. M., Jung, R. E., and Sibbitt, W. L. (2005). A novel technique to study the brain’s response to pain: Proton magnetic resonance spectroscopy. *NeuroImage*, 26(2):642–646.
- Muthukumaraswamy, S. D., Edden, R. A., Jones, D. K., Swettenham, J. B., and Singh, K. D. (2009). Resting GABA concentration predicts peak gamma frequency and fMRI amplitude in response to visual stimulation in humans. *Proceedings of the National Academy of Sciences of the United States of America*, 106(20):8356–8361.
- Muthukumaraswamy, S. D., Evans, C. J., Edden, R. A., Wise, R. G., and Singh, K. D. (2012). Individual variability in the shape and amplitude of the BOLD-HRF correlates with endogenous GABAergic inhibition. *Human Brain Mapping*, 33(2):455–465.
- Near, J., Edden, R., Evans, C. J., Paquin, R., Harris, A., and Jezzard, P. (2015). Frequency and phase drift correction of magnetic resonance spectroscopy data by spectral registration in the time domain. *Magnetic Resonance in Medicine*, 73(1):44–50.
- Near, J., Simpson, R., Cowen, P., and Jezzard, P. (2011). Efficient  $\gamma$ -aminobutyric acid editing at 3T without macromolecule contamination: MEGA-SPECIAL. *NMR in Biomedicine*, 24(10):1277–85.
- Northoff, G., Walter, M., Schulte, R. F., Beck, J., Dydak, U., Henning, A., Boeker, H., Grimm, S., and Boesiger, P. (2007). GABA concentrations in the human anterior cingulate cortex predict negative BOLD responses in fMRI. *Nature Neuroscience*, 10(12):1515–1517.

- Oeltzschner, G., Puts, N. A. J., Chan, K. L., Boer, V. O., Barker, P. B., and Edden, R. A. E. (2016). Dual-volume excitation and parallel reconstruction for J-difference-edited MR spectroscopy. *Magnetic Resonance in Medicine*, 22:16–22.
- Ogawa, S., Lee, T., Kay, A. R., and Tank, D. W. (1990a). Brain magnetic resonance imaging with contrast dependent on blood oxygenation. *Proceedings of the National Academy of Sciences of the United States of America*, 87(24):9868–9872.
- Ogawa, S. and Lee, T.-M. (1990). Magnetic resonance imaging of blood vessels at high fields: In vivo and in vitro measurements and image simulation. *Magnetic Resonance in Medicine*, 16(1):9–18.
- Ogawa, S., Lee, T.-M., Nayak, A. S., and Glynn, P. (1990b). Oxygenation-sensitive contrast in magnetic resonance image of rodent brain at high magnetic fields. *Magnetic Resonance in Medicine*, 14(1):68–78.
- O’Gorman, R. L., Michels, L., Edden, R. A., Murdoch, J. B., and Martin, E. (2011). In vivo detection of GABA and glutamate with MEGA-PRESS: Reproducibility and gender effects. *Journal of Magnetic Resonance Imaging*, 33(5):1262–1267.
- Owen, D. G., Bureau, Y., Thomas, a. W., Prato, F. S., and St Lawrence, K. S. (2008). Quantification of pain-induced changes in cerebral blood flow by perfusion MRI. *Pain*, 136(1-2):85–96.
- Patel, A. B., de Graaf, R. a., Mason, G. F., Rothman, D. L., Shulman, R. G., and Behar, K. L. (2005). The contribution of GABA to glutamate/glutamine cycling and energy metabolism in the rat cortex in vivo. *Proceedings of the National Academy of Sciences of the United States of America*, 102(15):5588–5593.
- Pauli, W. (1925). Über den zusammenhang des abschlusses der elektronengruppen im atom mit der komplexstruktur der spektren. *Zeitschrift für Physik*, 31(1):765–783.
- Penfield, W. and Boldrey, E. (1937). Somatic motor and sensory representation in the cerebral cortex of man as studied by electrical stimulation. *Brain*, 60(4):389–443.
- Peyron, R., Laurent, B., and Garcia-Larrea, L. (2000). Functional imaging of brain responses to pain. A review and meta-analysis. *Neurophysiologie Clinique/Clinical Neurophysiology*, 30(5):263–288.
- Price, D. D. (2000). Psychological and neural mechanisms of the affective dimension of pain. *Science*, 288(5472):1769–72.

- Price, D. D., Hu, J. W., Dubner, R., and Gracely, R. H. (1977). Peripheral suppression of first pain and central summation of second pain evoked by noxious heat pulses. *Pain*, 3(1):57–68.
- Proctor, W. G. and Yu, F. C. (1950). The Dependence of a Nuclear Magnetic Resonance Frequency upon Chemical Compound. *Physical Review*, 77:717.
- Provencher, S. W. (2001). Automatic quantitation of localized in vivo  $^1\text{H}$  spectra with LCMoDel. *NMR in Biomedicine*, 14(4):260–264.
- Purcell, E. M., Torrey, H. C., and Pound, R. V. (1946). Resonance Absorption by Nuclear Magnetic Moments in a Solid. *Physical Review*, 69:37–38.
- Puts, N. A. J., Barker, P. B., and Edden, R. A. E. (2013). Measuring the longitudinal relaxation time of GABA in vivo at 3 Tesla. *Journal of Magnetic Resonance Imaging*, 37(4):999–1003.
- Rae, C. D. (2014). A guide to the metabolic pathways and function of metabolites observed in human brain  $^1\text{H}$  magnetic resonance spectra. *Neurochemical Research*, 39(1):1–36.
- Raichle, M. E., MacLeod, A. M., Snyder, A. Z., Powers, W. J., Gusnard, D. A., and Shulman, G. L. (2001). A default mode of brain function. *Proceedings of the National Academy of Sciences of the United States of America*, 98(2):676–682.
- Rothman, D. L., De Feyter, H. M., Graaf, R. A., Mason, G. F., and Behar, K. L. (2011).  $^{13}\text{C}$  MRS studies of neuroenergetics and neurotransmitter cycling in humans. *NMR in Biomedicine*, 24(8):943–957.
- Rothman, K. J. (1990). No Adjustments Are Needed for Multiple Comparisons. *Epidemiology*, 1(1):43–46.
- Saleh, M. G., Oeltzschner, G., Chan, K. L., Puts, N. A. J., Mikkelsen, M., Schär, M., Harris, A. D., and Edden, R. A. E. (2016). Simultaneous edited MRS of GABA and glutathione. *NeuroImage*, 142:576–582.
- Sandgren, N., Stoica, P., Frigo, F. J., and Selén, Y. (2005). Spectral analysis of multichannel MRS data. *Journal of Magnetic Resonance*, 175(1):79–91.
- Savitzky, A. and Golay, M. J. E. (1964). Smoothing and Differentiation of Data by Simplified Least Squares Procedures. *Analytical Chemistry*, 36(8):1627–1639.



- Schaller, B., Xin, L., O'Brien, K., Magill, A. W., and Gruetter, R. (2014). Are glutamate and lactate increases ubiquitous to physiological activation? A  $^1\text{H}$  functional MR spectroscopy study during motor activation in human brain at 7 Tesla. *NeuroImage*, 93(P1):138–145.
- Schneider, F. and Fink, G. (2007). *Funktionelle MRT in Psychiatrie und Neurologie*. Springer.
- Schubert, F., Gallinat, J., Seifert, F., and Rinneberg, H. (2004). Glutamate concentrations in human brain using single voxel proton magnetic resonance spectroscopy at 3 Tesla. *NeuroImage*, 21(4):1762–1771.
- Shulman, R. and Rothman, D. (1998). Interpreting functional imaging studies in terms of neurotransmitter cycling. *Proceedings of the National Academy of Sciences of the United States of America*, 95(20):11993–11998.
- Shungu, D. C., Mao, X., Gu, M., Milak, M. S., Weiduschat, N., Mayer, D., Spielman, D., Mann, J. J., and Kegeles, L. S. (2013). 'Glx' Measured by J-editing/MEGA-PRESS is Primarily 'Pure' Glutamate... Or is it? In *Proceedings of the International Society for Magnetic Resonance in Medicine*, volume 21, #3985, Salt Lake City, Utah, USA.
- Silbernagl, S. and Despopoulos, A. (2012). *Taschenatlas der Physiologie, 8. Auflage*. Georg Thieme Verlag KG.
- Simpson, R., Devenyi, G. A., Jezzard, P., Hennessy, T. J., and Near, J. (2017). Advanced processing and simulation of MRS data using the FID appliance (FID-A) - An open source, MATLAB-based toolkit. *Magnetic Resonance in Medicine*, 77(1):23–33.
- Stagg, C. J., Bachtiar, V., Amadi, U., Gudberg, C. A., Ilie, A. S., Sampaio-Baptista, C., O'Shea, J., Woolrich, M., Smith, S. M., Filippini, N., Near, J., and Johansen-Berg, H. (2014). Local GABA concentration is related to network-level resting functional connectivity. *eLife*, 3(3):1–9.
- Stagg, C. J., Bachtiar, V., and Johansen-Berg, H. (2011a). The role of GABA in human motor learning. *Current Biology*, 21(6):480–4.
- Stagg, C. J., Bachtiar, V., and Johansen-Berg, H. (2011b). What are we measuring with GABA magnetic resonance spectroscopy? *Communicative & Integrative Biology*, 4(5):573–5.
- Star-Lack, J., Spielman, D., Adalsteinsson, E., Kurhanewicz, J., Terris, D. J., and Vigneron, D. B. (1998). In vivo lactate editing with simultaneous detection of choline,

- creatine, NAA, and lipid singlets at 1.5 T using PRESS excitation with applications to the study of brain and head and neck tumors. *Journal of Magnetic Resonance*, 133(2):243–54.
- Stefan, D., Cesare, F. D., Andrasescu, a., Popa, E., Lazariev, a., Vescovo, E., Strbak, O., Williams, S., Starcuk, Z., Cabanas, M., van Ormondt, D., and Graveron-Demilly, D. (2009). Quantitation of magnetic resonance spectroscopy signals: the jMRUI software package. *Measurement Science and Technology*, 20(10):104035.
- Symonds, L. L. (2006). Right-Lateralized Pain Processing in the Human Cortex: An fMRI Study. *Journal of Neurophysiology*, 95(6):3823–3830.
- Terpstra, M., Vaughan, T. J., Ugurbil, K., Lim, K. O., Schulz, S. C., and Gruetter, R. (2005). Validation of glutathione quantitation from STEAM spectra against edited 1H NMR spectroscopy at 4T: application to schizophrenia. *Magnetic Resonance Materials in Physics, Biology and Medicine*, 18(5):276–82.
- Vanhamme, L., van den Boogaart, A., and Van Huffel, S. (1997). Improved Method for Accurate and Efficient Quantification of MRS Data with Use of Prior Knowledge. *Journal of Magnetic Resonance*, 129(1):35–43.
- Veenendaal, T. M. V., Backes, W. H., Aldenkamp, A. P., Medicine, N., Science, R., and States, U. (2016). On the composition of Glx in MEGA-PRESS measurements at 3T, is it glutamate? In *Proceedings of the International Society for Magnetic Resonance in Medicine*, volume 24, #4004, Singapore.
- Violante, I. R., Ribeiro, M. J., Edden, R. A. E., Guimarães, P., Bernardino, I., Rebola, J., Cunha, G., Silva, E., and Castelo-Branco, M. (2013). GABA deficit in the visual cortex of patients with neurofibromatosis type 1: genotype-phenotype correlations and functional impact. *Brain*, 136(3):918–25.
- Vlaardingerbroek, M. T. and den Boer, J. A. (2003). *Magnetic Resonance Imaging - Theory and Practice (Third Edition)*. Springer.
- Von Korff, M., Jensen, M. P., and Karoly, P. (2000). Assessing global pain severity by self-report in clinical and health services research. *Spine*, 25(24):3140–3151.
- Wagner, G., Gussev, A., Köhler, S., de la Cruz, F., Smesny, S., Reichenbach, J. R., and Bär, K.-j. (2016). Resting state functional connectivity of the hippocampus along the anteriorposterior axis and its association with glutamatergic metabolism. *Cortex*, 81:104–117.

- Walls, A. B., Waagepetersen, H. S., Bak, L. K., Schousboe, A., and Sonnewald, U. (2015). The glutamine-glutamate/GABA cycle: function, regional differences in glutamate and GABA production and effects of interference with GABA metabolism. *Neurochemical Research*, 40(2):402–9.
- Worsley, K. and Friston, K. (1995). Analysis of fMRI Time-Series Revisited Again. *NeuroImage*, 2(3):173–181.
- Worsley, K. J., Evans, A. C., Marrett, S., and Neelin, P. (1992). A Three-Dimensional Statistical Analysis for CBF Activation Studies in Human Brain. *Journal of Cerebral Blood Flow & Metabolism*, 12(6):900–918.
- Zaaraoui, W., Fleysher, L., Fleysher, R., Liu, S., Soher, B. J., and Gonen, O. (2007). Human brain-structure resolved T2 relaxation times of proton metabolites at 3 Tesla. *Magnetic Resonance in Medicine*, 57(6):983–989.
- Zhuo, M. (2008). Cortical excitation and chronic pain. *Trends in Neurosciences*, 31(4):199–207.

# List of Figures

2.1	FID signal detection and corresponding frequency spectrum . . . . .	10
2.2	Conventional <i>in vivo</i> $^1\text{H}$ MR spectrum . . . . .	12
2.3	J-coupling . . . . .	14
2.4	J-coupling evolution of a weakly J-coupled <i>AX</i> spin system . . . . .	15
2.5	J-difference editing of a weakly J-coupled <i>AX</i> spin system . . . . .	16
2.6	$^1\text{H}$ MEGA-PRESS spectra and GABA molecule . . . . .	18
2.7	$^1\text{H}$ MEGA-PRESS sequence . . . . .	19
2.8	J-coupling evolution of GABA at 3.0 ppm with TE . . . . .	20
2.9	jMRUI fitting of NED and DIFF spectra . . . . .	22
2.10	Glu and Gln molecules . . . . .	24
2.11	Cycling of GABA, Glu and Gln . . . . .	26
2.12	Hemodynamic response function and fMRI data acquisition using a block design stimulation . . . . .	28
2.13	SPM processing pipeline of fMRI data . . . . .	31
3.1	Post-processing pipeline for $^1\text{H}$ MEGA-PRESS spectra . . . . .	35
3.2	Subtraction artifacts in the mean DIFF spectrum . . . . .	39
3.3	Visualisation of the $L^1$ or $L^2$ norm based minimization criteria to optimize mean DIFF spectra . . . . .	40
3.4	Difference optimization processing scheme . . . . .	41
3.5	Performance of difference optimization on simulation data (color encoded matrix) . . . . .	43
3.6	Performance of difference optimization on simulation data (bar plots) .	44
3.7	Performance of difference optimization on <i>in vivo</i> data . . . . .	45
3.8	Exemplary minimization of $\Delta f$ and $\Delta\phi$ using difference optimization .	46
4.1	Glu and Gln phantom measurements with varied frequency selective editing pulse position . . . . .	53
4.2	Experiment setup of phantoms with varied GABA and Glu concentrations	56
4.3	Detectable concentration changes of $\Delta\text{GABA}$ and $\Delta\text{Glu}$ <i>in vitro</i> . . . .	58

4.4	Detectable concentration changes of $\Delta$ GABA and $\Delta$ Glu under simulated <i>in vivo</i> conditions . . . . .	60
5.1	MR compatible thermode and stimulation unit . . . . .	64
5.2	Voxel position in ACC and OC for fMRS measurements . . . . .	65
5.3	Data acquisition scheme during the fMRS experiment . . . . .	66
5.4	Relative changes of Glx/tCr and GABA+/tCr in ACC and OC . . . . .	68
5.5	Mean $^1\text{H}$ MEGA-PRESS DIFF spectra for REF and PAIN state in ACC and OC . . . . .	69
5.6	Absolute changes of Glx/tCr and GABA+/tCr in ACC and OC . . . . .	71
6.1	Heat pain stimulation paradigm and fMRI data evaluation using a sliding window approach . . . . .	79
6.2	ROI masks for lIns, rIns, ACC and precuneus . . . . .	80
6.3	BOLD signal changes depending on duration of heat pain stimulation in lIns, rIns, ACC and precuneus . . . . .	82
6.4	Data acquisition scheme during the combined fMRS and fMRI experiment	83
6.5	Processing steps for combined fMRS and fMRI data evaluation . . . . .	86
6.6	Relative changes of Glx/tCr and GABA+/tCr in the insular cortex . . . . .	88
6.7	MRS voxel position in the insula and statistical map of the group fMRI response to pain stimulation . . . . .	89
6.8	Negative association between BOLD signal clusters and insular GABA+/tCr	90
6.9	Positive association between BOLD signal clusters and insular $\Delta$ Glx . . . . .	92

# List of Tables

2.1	<i>In vivo</i> T <sub>1</sub> and T <sub>2</sub> values for selected metabolites in GM and WM at 3T	23
4.1	Detectable concentration changes of ΔGABA and ΔGlx <i>in vitro</i> and under simulated <i>in vivo</i> conditions	61
5.1	fMRS results for Glx/tCr and GABA+/tCr in ACC and OC	69
5.2	fMRS results for NAA/tCr, tCho/tCr and tCr/H <sub>2</sub> O in ACC and OC	70
6.1	BOLD signal variations during prolonged heat pain stimulation for lIns, rIns, ACC and precuneus.	81
6.2	Brain regions showing significant BOLD activation during pain perception	89
6.3	Clusters showing a negative association between BOLD and GABA+/tCr	90
6.4	Clusters showing a positive association between BOLD and ΔGlx	91
A.1	Measurement Parameters MRS (Part 1)	xxxii
A.2	Measurement Parameters MRS (Part 2)	xxxiii
A.3	Measurement Parameters MRI (Part 1)	xxxiv
A.4	Measurement Parameters MRI (Part 2)	xxxiv

# Appendix

## A.1 List of all measurement parameters

On the following two pages all used MRS and MRI sequences and relevant measurement parameters are listed in four tables. Sequent numbers are assigned to the measurements given in the first column. Thus, referencing from the main text to the according sequences is done by, e.g. "Tab. A.1:4", and according measurement parameters are found in Table A.1 at line 4. Moreover, MRS and MRI measurement parameters are continued in one of the following tables A.2 and A.4 labelled with the same number listed in the first column. All measurements were performed on a 3 T Siemens MR scanner using vendor supplied receiver coils. Note that a single  $^1\text{H}$  MEGA-PRESS scan consists of acquiring one ED and one NED spectrum, resulting in an overall acquisition period of two TR intervals per scan.

#	Sequence	TR	TE	TA	NAS	BW	$N_{Samp}$	$Ed_{NED}$	$Ed_{ED}$	Water suppression
1	$^1\text{H}$ MEGA-PRESS	1.8 s	68 ms	11.5 min	192	2.8 kHz	4k	7.5 ppm	1.9 ppm	reduced
2	$^1\text{H}$ MEGA-PRESS	1.8 s	68 ms	0.1 min	1	2.8 kHz	4k	7.5 ppm	1.9 ppm	none
3	$^1\text{H}$ PRESS	2.0 s	30 ms	0.5 min	16	2.4 kHz	2k	-	-	reduced
4	$^1\text{H}$ MEGA-PRESS	2.0 s	68 ms	1.1 min	16	2.5 kHz	4k	7.5 ppm	1.7 ppm - 2.5 ppm	reduced
5	$^1\text{H}$ MEGA-PRESS	2.0 s	68 ms	0.5 min	8	2.5 kHz	4k	7.5 ppm	1.7 ppm	none
6	$^1\text{H}$ PRESS	2.0 s	30 ms	0.5 min	16	2.4 kHz	2k	-	-	reduced
7	$^1\text{H}$ MEGA-PRESS	3.0 s	68 ms	1.6 min	16	2.4 kHz	4k	7.5 ppm	1.9 ppm	reduced
8	$^1\text{H}$ MEGA-PRESS	3.0 s	68 ms	0.4 min	4	2.4 kHz	4k	7.5 ppm	1.9 ppm	none
9	$^1\text{H}$ MEGA-PRESS	3.0 s	68 ms	12.8 min	128	2.8 kHz	4k	7.5 ppm	1.9 ppm	reduced
10	$^1\text{H}$ MEGA-PRESS	3.0 s	68 ms	1.6 min	16	2.8 kHz	4k	7.5 ppm	1.9 ppm	none
11	$^1\text{H}$ MEGA-PRESS	3.0 s	68 ms	5.6 min	56	2.8 kHz	4k	7.5 ppm	1.9 ppm	reduced
12	$^1\text{H}$ MEGA-PRESS	3.0 s	68 ms	2.4 min	24	2.8 kHz	4k	7.5 ppm	1.9 ppm	none
13	$^1\text{H}$ MEGA-PRESS	3.0 s	68 ms	12.8 min	128	2.8 kHz	4k	7.5 ppm	1.9 ppm	reduced
14	$^1\text{H}$ MEGA-PRESS	3.0 s	68 ms	1.6 min	16	2.8 kHz	4k	7.5 ppm	1.9 ppm	none
15	$^1\text{H}$ MEGA-PRESS	3.0 s	68 ms	5.6 min	56	2.8 kHz	4k	7.5 ppm	1.9 ppm	reduced
16	$^1\text{H}$ MEGA-PRESS	3.0 s	68 ms	2.4 min	24	2.8 kHz	4k	7.5 ppm	1.9 ppm	none
17	$^1\text{H}$ MEGA-PRESS	1.8 s	68 ms	12 min	192	2.9 kHz	4k	7.5 ppm	1.9 ppm	reduced
18	$^1\text{H}$ MEGA-PRESS	1.8 s	68 ms	1 min	16	2.9 kHz	4k	7.5 ppm	1.9 ppm	none
19	$^1\text{H}$ MEGA-PRESS	1.8 s	68 ms	6 min	96	2.9 kHz	4k	7.5 ppm	1.9 ppm	reduced

Table A.1: Acquisition parameters for all performed magnetic resonance spectroscopy measurements. The table is continued in Tab. A.2



#	Shim	Volume	Brain region/Object	Receiver coil	MR scanner
1	manual	$(25 \times 35 \times 12) \text{ mm}^3$	PC	12-channel head matrix coil	TIM Trio
2	manual	$(25 \times 35 \times 12) \text{ mm}^3$	PC	12-channel head matrix coil	TIM Trio
3	manual	$(25 \times 25 \times 25) \text{ mm}^3$	Phantom	64-channel head matrix coil	Prisma fit
4	manual	$(25 \times 25 \times 25) \text{ mm}^3$	Phantom	64-channel head matrix coil	Prisma fit
5	manual	$(25 \times 25 \times 25) \text{ mm}^3$	Phantom	64-channel head matrix coil	Prisma fit
6	manual	$(25 \times 25 \times 25) \text{ mm}^3$	Phantom	64-channel head matrix coil	Prisma fit
7	manual	$(25 \times 25 \times 25) \text{ mm}^3$	Phantom	64-channel head matrix coil	Prisma fit
8	manual	$(25 \times 25 \times 25) \text{ mm}^3$	Phantom	64-channel head matrix coil	Prisma fit
9	manual	$(36 \times 20 \times 12) \text{ mm}^3$	ACC <small>(REF)</small>	12-channel head matrix coil	TIM Trio
10	manual	$(36 \times 20 \times 12) \text{ mm}^3$	ACC	12-channel head matrix coil	TIM Trio
11	manual	$(36 \times 20 \times 12) \text{ mm}^3$	ACC <small>(STIMULATION)</small>	12-channel head matrix coil	TIM Trio
12	manual	$(36 \times 20 \times 12) \text{ mm}^3$	ACC <small>(DUMMY)</small>	12-channel head matrix coil	TIM Trio
13	manual	$(35 \times 20 \times 15) \text{ mm}^3$	OC <small>(REF)</small>	12-channel head matrix coil	TIM Trio
14	manual	$(35 \times 20 \times 15) \text{ mm}^3$	OC	12-channel head matrix coil	TIM Trio
15	manual	$(35 \times 20 \times 15) \text{ mm}^3$	OC <small>(STIMULATION)</small>	12-channel head matrix coil	TIM Trio
16	manual	$(35 \times 20 \times 15) \text{ mm}^3$	OC <small>(DUMMY)</small>	12-channel head matrix coil	TIM Trio
17	manual	$(28 \times 40 \times 14) \text{ mm}^3$	lIns <small>(REF)</small>	64-channel head matrix coil	Prisma fit
18	manual	$(28 \times 40 \times 14) \text{ mm}^3$	lIns	64-channel head matrix coil	Prisma fit
19	manual	$(28 \times 40 \times 14) \text{ mm}^3$	lIns <small>(STIMULATION)</small>	64-channel head matrix coil	Prisma fit

Table A.2: Additional measurement parameters from Tab. A.1 for all performed magnetic resonance spectroscopy measurements.

#	Sequence	Matrix	FOV	TR	TE	Slice thickness	Slices	Volumes	GRAPPA/Turbo factor
1	MP-RAGE	256 x 256	256 x 256 mm <sup>2</sup>	2530 ms	3 ms	1.0 mm	176	-	2
2	MP-RAGE	256 x 256	256 x 256 mm <sup>2</sup>	2630 ms	3 ms	1.0 mm	176	-	2
3	EPI	106 x 106	220 x 220 mm <sup>2</sup>	2000 ms	30 ms	2.6 mm	24	200	2
4	EPI	106 x 106	220 x 220 mm <sup>2</sup>	1600 ms	30 ms	3.2 mm	24	200	2
5	MP-RAGE	256 x 256	256 x 256 mm <sup>2</sup>	2300 ms	3 ms	1.0 mm	192	-	2
6	EPI	106 x 106	220 x 220 mm <sup>2</sup>	1600 ms	30 ms	3.2 mm	24	2 x 90	2

Table A.3: Acquisition parameters for all performed magnetic resonance imaging measurements. The table is continued in Tab. A.4.

#	Anatomical region/Object	Receiver coil	MR Scanner
1	Brain	12-channel head matrix coil	TIM Trio
2	Brain	12-channel head matrix coil	TIM Trio
3	Brain	64-channel head matrix coil	Prisma fit
4	Brain	64-channel head matrix coil	Prisma fit
5	Brain	64-channel head matrix coil	Prisma fit
6	Brain	64-channel head matrix coil	Prisma fit

Table A.4: Additional measurement parameters from Tab. A.3 for all performed magnetic resonance imaging measurements.

## A.2 Lebenslauf

### Marianne Cleve

Kefersteinstr. 10

07745 Jena

marianne\_cleve@web.de

### Persönliche Angaben

Geburtsdatum	16.12.1986
Geburtsort	Halle (Saale), Deutschland
Geschlecht	Weiblich
Staatsangehörigkeit	Deutsch

### Ausbildung und wissenschaftlicher Werdegang

08/2012 - heute	Martin-Luther-Universität Halle-Wittenberg Doktorandin an der Naturwissenschaftlichen Fakultät II, Institut für Physik
08/2012 - heute	Medizinische Physik, IDIR, Universitätsklinikum Jena Wissenschaftliche Mitarbeiterin
07/2015 - 06/2017	Martin-Luther-Universität Halle-Wittenberg Stipendiatin der Graduiertenförderung Sachsen-Anhalt
10/2009 - 12/2011	Martin-Luther-Universität Halle-Wittenberg Masterstudium der Medizinischen Physik (1,2)
10/2006 - 09/2009	Martin-Luther-Universität Halle-Wittenberg Bachelorstudium der Medizinischen Physik (2,0)
08/1997 - 07/2006	Gymnasium Große Stadtschule Wismar Abschluss: Allgemeine Hochschulreife (1,2) Mit Auszeichnung für besondere Leistungen in den Naturwissenschaften

### Angaben zu Vorstrafen

Es liegen weder Vorstrafen vor, noch ist ein Ermittlungsverfahren eingeleitet.

Jena, August 2017

## A.3 Auszeichnungen

- 2017 | ISMRM Merit Award Summa Cum Laude und Präsentation in der  
Poster-Highlights Session der ISMRM MR Spectroscopy Study Group,  
Honolulu, HI, USA  
*Interregional associations between GABA+, Glx and BOLD contrast  
changes during acute pain perception in the human brain - A combined  $^1H$   
fMRS and fMRI study*
- 2015 | Stipendium der Graduiertenförderung Sachsen-Anhalt  
Martin-Luther-Universität Halle-Wittenberg
- 2014 | ISMRM Merit Award Magna Cum Laude und Präsentation in der  
Poster-Highlights Session der ISMRM MR Spectroscopy Study Group,  
Mailand, Italien  
*In vivo measurements of acute pain induced changes of GABA+ and Glx in  
the brain with functional  $^1H$  MEGA-PRESS MR spectroscopy*

## A.4 Veröffentlichungen

### Artikel

- **Cleve M.**, Gussew A., Wagner G., Bär K.-J., Reichenbach J.R. (2017). Assessment of intra- and inter-regional interrelations between GABA+, Glx and BOLD during pain perception in the human brain - A combined  $^1\text{H}$  fMRS and fMRI study. *Neuroscience*, revision in progress (15.07.2017).
- **Cleve M.**, Krämer M., Gussew A., Reichenbach J.R. (2017). Difference optimization: Automatic correction of relative frequency and phase for mean non-edited and edited GABA  $^1\text{H}$  MEGA-PRESS spectra. *Journal of Magnetic Resonance*, 279, 16-21.
- **Cleve M.**, Gussew A., Reichenbach J.R. (2015). *In vivo* detection of acute pain-induced changes of GABA+ and Glx in the human brain by using functional  $^1\text{H}$  MEGA-PRESS MR spectroscopy. *NeuroImage*, 105, 67-75.

### Konferenzbeiträge

#### Poster

- **Cleve M.**, Gussew A., Wagner G., Reichenbach J. R. (2017). Interregional associations between GABA+, Glx and BOLD contrast changes during acute pain perception in the human brain A combined  $^1\text{H}$  fMRS and fMRI study. In *Proceedings of the International Society for Magnetic Resonance in Medicine*, volume 25, #5633, Honolulu, HI, USA.
- **Cleve M.**, Krämer M., Gussew A., Reichenbach, J. R. (2017). Difference optimization: Automatic correction of relative frequency and phase for  $^1\text{H}$  MEGA-PRESS spectra. In *Proceedings of the International Society for Magnetic Resonance in Medicine*, volume 25, #2997, Honolulu, HI, USA.
- **Cleve M.**, Gussew A., Reichenbach J.R. (2016). BOLD-fMRI signal changes during prolonged heat pain stimulation. In *Proceedings of the International Society for Magnetic Resonance in Medicine*, volume 24, #1736, Singapore.
- **Cleve M.**, Krämer M., Gussew A., Reichenbach J.R. (2016). Automatic correction of relative frequency and phase for  $^1\text{H}$  MEGA-PRESS spectra. In *Proceedings of the German Chapter of the International Society for Magnetic Resonance in Medicine*, volume 19, #7, Würzburg, Germany.
- Feng X., Deistung A., **Cleve M.**, Schweser F., Reichenbach J.R. (2016). Investigation of intrascanner reproducibility of quantitative susceptibility mapping (QSM) and  $R2^*$  at 3T. In *Proceedings of the International Society for Magnetic Resonance in Medicine*, volume 24, #2857, Singapore.

- Gussew A., Janetzki L., **Cleve M.**, Borys C., Reichenbach J.R. (2016). Chronic pain related alterations of regional and interregional glutamate and GABA associations in the human brain. In *Proceedings of the International Society for Magnetic Resonance in Medicine*, volume 24, #3986, Singapore.
- Gussew A., Wagner G., Near J., **Cleve M.**, Reichenbach J.R. (2016). Assessment of interrelations between DMN resting state functional connectivity and brain GABA concentrations by using functional MRI and  $^1\text{H}$ -MEGA-PRESS MRS with and without suppression of macromolecules. In *Proceedings of the German Chapter of the International Society for Magnetic Resonance in Medicine*, volume 19, #23, Würzburg, Germany.
- **Cleve M.**, Gussew A., Janetzki L., Borys C., Reichenbach J.R. (2015). Interregional associations between excitatory and inhibitory neurotransmitters in the resting human brain. In *Proceedings of the International Society for Magnetic Resonance in Medicine*, volume 23, #4637, Toronto, Canada.
- Feng X., Deistung A., **Cleve M.**, Gussew A., Schweser F., Reichenbach J.R. (2015). Intra-scanner reproducibility of quantitative susceptibility mapping (QSM). In *European Society for Magnetic Resonance in Medicine and Biology*, volume 32, #294, Edinburgh, UK.
- Gussew A., Borys C., Janetzki L., **Cleve M.**, Habenicht U., Malessa R., Strau B., Reichenbach J.R. (2015). Altered regional and interregional interrelations of glutamate and GABA in patients with chronic low back pain A  $^1\text{H}$ -MR spectroscopic study. In *Jahrestagung der Deutschen Gesellschaft für Klinische Neurophysiologie und Funktionelle Bildgebung*, volume 60, #27, Tübingen, Germany.
- **Cleve M.**, Gussew A., Reichenbach J.R. (2014). *In vivo* measurements of acute pain induced changes of GABA+ and Glx in the brain with functional  $^1\text{H}$ -MEGA-PRESS MR spectroscopy. In *Proceedings of the International Society for Magnetic Resonance in Medicine*, volume 22, #485, Milan, Italy.
- **Cleve M.**, Gussew A., Hiepe P., Rzanny R., Reichenbach J.R. (2014). Impact of spectra quality on GABA quantitation with  $^1\text{H}$  MEGA-PRESS sequence. In *Proceedings of the International Society for Magnetic Resonance in Medicine*, volume 22, #2881, Milan, Italy.
- **Cleve M.**, Gussew A., Hiepe P., Rzanny R., Reichenbach J.R. (2013). Impact of SNR and linewidth on accuracy and reproducibility of GABA detection with MEGA-PRESS sequence. In *Jahrestagung der Deutschen Gesellschaft für Medizinische Physik*, volume 44, #38, Köln, Germany.
- Gussew A., Wagner G., Deistung A., Rzanny R., Hiepe P., **Cleve M.**, Bär K.-J., Reichenbach J.R. (2013). Assessment of hippocampal activation and resting state glutamate concentration by using functional MRI and  $^1\text{H}$  MR spectroscopic imaging. *Proceedings of the International Society for Magnetic Resonance in Medicine*, volume 21, #1952, Salt Lake City, Utah, USA.

## Vorträge

- **Cleve M.**, Gussew A., Janetzki L., Borys C., Reichenbach J.R. (2015). Interregionale Zusammenhänge zwischen den erregenden und hemmenden Neurotransmittern Glutamat und GABA im menschlichen Gehirn. In *Jahrestagung der Deutschen Gesellschaft für Medizinische Physik*, volume 46, Marburg, Germany.
- **Cleve M.**, Gussew A., Reichenbach J.R. (2014). *In vivo* Nachweis akut schmerzinduzierter Änderungen von GABA+ und Glx im menschlichen Gehirn mit funktioneller  $^1\text{H}$ -MEGA-PRESS MR Spektroskopie. In *Proceedings of the German Chapter of the International Society for Magnetic Resonance in Medicine*, vol. 17, #4, Jena, Germany.
- **Cleve M.**, Gussew A., Reichenbach J.R. (2014). Acute pain induced GABA+ and Glx changes in the human brain - a functional  $^1\text{H}$ -MR spectroscopy study. In *Jahrestagung des Interdisziplinären Netzwerks für Molekulare Bildgebung (INMB) - MoBi 2014*, #17, Jena, Germany.
- **Cleve M.**, Gussew A., Reichenbach J.R. (2013). *In vivo* measurements of acute pain induced changes of GABA and Glx with functional  $^1\text{H}$  MEGA-PRESS MR spectroscopy. In *Cardiff International Symposium on MR Spectroscopy of GABA*, volume 2, #28, Cardiff, Wales, UK.

## Eingeladene Vorträge

- **Cleve M.** (2017).  $^1\text{H}$  MR-Spektroskopie des menschlichen Gehirns - Methoden und Anwendungen. In *CME-Fortbildung für Radiologen*, IDIR, Universitätsklinikum Jena, Germany
- **Cleve M.** (2015).  $^1\text{H}$  MR spectroscopy - Exploring neurochemical mechanisms regulating the brain activity. In *CME-Fortbildung für Radiologen*, IDIR, Universitätsklinikum Jena, Germany
- **Cleve M.** (2015).  $^1\text{H}$  MR spectroscopy - Exploring neurochemical mechanisms regulating the brain activity. In *Neurowissenschaftliches Seminar*, Medical Physics Group und Klinik für Psychiatrie des Universitätsklinikums Jena, Germany

## A.5 Danksagung

Ohne die Unterstützung zahlreicher Menschen wäre diese Arbeit nicht zustande gekommen. Zuallererst möchte ich mich herzlich bei meinen beiden Betreuern Prof. Dr. Jürgen R. Reichenbach und Prof. Dr. Jochen Balbach bedanken, die mir während meiner gesamten Promotionszeit immer mit fachlichen Diskussionen und konstruktiven Denkanstößen zur Seite standen.

Besonderer Dank gilt Dr. Alexander Gussew, der mir bei wissenschaftlichen Fragestellungen, aber auch bei Problemen nicht-fachlicher Natur, immer den Rücken gestärkt hat.

Ebenso möchte ich mich bei allen aktuellen und ehemaligen Kollegen aus der Medical Physics Group bedanken. Jeder Einzelne hat auf seine Weise zu dem Gelingen der vorliegenden Arbeit beigetragen.

... Bei M.A. Kevin Moll für die freundschaftliche Büro- und Banknachbarschaft, die produktive Arbeitsatmosphäre (Journal of Pork Hedgehog!) und die unzähligen Küchengespräche,

... Bei Dr. Martin Krämer für die zahlreichen, äußerst konstruktiven Diskussionen, und dass ich von ihm so viel über das Programmieren lernen durfte,

... Bei Dr. Andreas Deistung für seine geduldige und hilfsbereite Art und die Regelmäßigkeit des täglichen Teekochens in unserem Büro,

... Bei Dr. Daniel Güllmar für die Einführung in die fMRT und den gelegten Grundstein zur Einsicht für die Notwendigkeit von Statistik,

... Bei Dr. Karl-Heinz Herrmann für die umfassenden Kenntnisse über Linux, MR-Sequenzen, Espressobohnen und Milchschaum,

... Bei Dr. Christian Ros für das Drücken des "Submit-Buttons" bei der Einreichung meines ersten Papers und die stets gute Laune.

Vielen Dank, dass ihr das Testen meiner Schmerzstimulation mitgemacht habt. Zudem hätten auch ohne euch die Konferenztouren, die gemeinsamen Grill- und Schellenbierabende nicht so viel Spaß gemacht.

Ebenso möchte ich meinen Dank auch all jenen Kollegen des Universitätsklinikums Jena aussprechen, die mich bei meiner Arbeit am Steiger unterstützt haben.

Nicht zuletzt gilt mein aufrichtiger Dank auch meinen Freunden, die mich in stressigen Promotionszeiten ausgehalten, für kreative Schaffenspausen gesorgt und wortwörtlich ihren Kopf für meine Studien hingehalten haben!

Meiner lieben Familie kann ich nicht genug danken. Danke, dass ihr da seid!



## A.6 Selbstständigkeitserklärung

Hiermit versichere ich ausdrücklich, dass ich die vorliegende Dissertation mit dem Thema

”Functional  $^1\text{H}$  MR spectroscopic investigations of pain processing in the human brain”

selbstständig und ohne fremde Hilfe verfasst, keine anderen als die von mir angegebenen Quellen und Hilfsmittel benutzt und die den benutzten Werken wörtlich oder inhaltlich entnommenen Stellen als solche kenntlich gemacht habe. Des Weiteren erkläre ich, dass ich noch keinen Promotionsversuch unternommen habe. Ich habe diese Dissertation weder in der gegenwärtigen noch in einer anderen Fassung einer anderen Fakultät vorgelegt.

Jena, August 2017

Marianne Cleve